Durham E-Theses

Modelling atom diffraction in pulsed and continuous far off-resonant optical lattices

BESWICK, BENJAMIN,THOMAS

How to cite:

BESWICK, BENJAMIN,THOMAS (2019) *Modelling atom diffraction in pulsed and continuous far off-resonant optical lattices*, Durham theses, Durham University. Available at Durham E-Theses Online: http://etheses.dur.ac.uk/13159/

Use policy

Modelling atom diffraction in pulsed and continuous far off-resonant optical lattices

Benjamin Thomas Beswick

Abstract

In this thesis we investigate the diffraction of cold atomic gases by optical lattices. Of particular interest to atom interferometry is the implementation of a high momentum-transfer "beam-splitter," which may be achieved by inducing quantum resonance in such an atomic gas. We use Monte Carlo simulations to investigate these quantum resonances in the regime where the gas receives laser pulses of finite duration, and demonstrate that an ϵ-pseudoclassical model for the dynamics of the gas atoms reproduces quantum resonant behavior for both zero-temperature and finite-temperature non-interacting gases. We show that this model agrees well with the fully quantum treatment of the system over a timescale set by the choice of experimental parameters.

In similar setups, the depth of a laser lattice may be measured by exposing an atomic gas to a series of off-resonant laser-standing-wave pulses, and fitting theoretical predictions for the population found in each of the allowed momentum states. We present an analytic model for the time evolution of the atomic populations of the lowest momentum-states, which is sufficient for a weak lattice, as well as numerical simulations incorporating higher momentum states for both relatively strong and weak lattices at zero and finite temperature. We propose a new approach to characterizing the depths of optical lattices, in which an atomic gas is given a finite initial momentum, leading to high amplitude oscillations in the zeroth diffraction order which are robust to finite-temperature effects. We present a zero-temperature analytic formula describing such oscillations, extend it to include atoms with initial momenta detuned from our chosen initial value, and analyze the full finite-temperature response.

Modelling atom diffraction in pulsed and continuous far off-resonant optical lattices

Benjamin Thomas Beswick

A thesis submitted in partial fulfillment
of the requirements for the degree of
Doctor of Philosophy

Department of Physics

Durham University

June 10, 2019

Contents

III   Lattice depth characterisation using continuous grating atom

List of Figures

Acknowledgements

First and foremost I would like to thank my supervisors, Simon Gardiner and Ifan Hughes, with whom it has been a pleasure to share the past four and a half years of stimulating discussions on physics. Your patient advice and tireless encouragement and support have made me a better scientist as well as a better person. I would also like to thank the Leverhulme Trust for funding through research program grant RP2013-k-009. Special thanks must also go to Matt Jones, Robert Potvliege, Andrew MacKellar, Charles Adams, Steven Wrathmall and Steve Hopkins for helpful discussions. It has been my privilege to enjoy the academic and social company of Matt Frye, Fliss McDowell and Yasmin Ilkhani during my time at Trevelyan college, you are among the kindest and wisest people I have met and this would have been a difficult journey without you. To Les, Kirsty, Danny, Karis, Becky, Mel, Hazel, and Jamie thank you for our conversations about life, the universe and everything, which have made my time at Durham unforgettable.

Declaration

I confirm that no part of the material offered has previously been submitted by myself for a degree in this or any other University. Where material has been generated through joint work, the work of others has been indicated.

Benjamin Thomas Beswick
Durham, June 10, 2019

Figures from papers are reproduced with permission.

For my parents

Chapter 1

Overview

1.1 Introduction

In this thesis we investigate the diffraction of cold dilute atomic gases by optical lattices [4], which has been of interest to atomic and molecular physics for some time. Many early examples of such experiments focused on the study of the relationship between classically chaotic systems [5, 6] and atom-optical realizations of their quantum counterparts. For instance, experiments in dynamical localization [7, 8, 9, 10, 11, 12, 13, 14] and quantum resonance in the atom-optics δ-kicked particle [15, 16, 17, 18, 19, 20, 21, 22, 23, 24, 25, 26, 27, 28].

More recently these quantum resonances have been investigated as high momentum transfer beam splitters with applications in atom interferometry [29]. It has also been demonstrated that the measurement process of the especially small lattice depths associated with weak atomic polarizabilities can be improved by diffracting an atomic gas using multiple pulses of a 1d far off resonant optical lattice with a suitably tuned period [30].

Though modeling techniques for both of these experiments are present in the literature [31, 32], many come with the burden of approximations and rules of thumb which may fall outside the range of experimental validity, but are considered necessary in order to make analytic and numerical results tractable and comparable to experimental data. In the case of quantum resonance, the Raman-Nath regime is often assumed, where the infinitesimal

nature of the lattice pulses prevent atoms from exploring the lattice during a pulse sequence. Though this approach yields simple analytic results for the resultant diffraction patterns, in practice such infinitesimal pulses are unachievable, and so finite-duration pulses must be included in any reasonable theoretical model of a real experiment [33].

A further consideration is that atom diffraction models rarely account for effects due to the finite-temperature of atomic gases, which has motivated the use of BECs due to their narrow initial momentum distributions. Exploration of the role of these effects would make it possible to understand atom diffraction experiments performed with atomic gases with initial temperatures that are much easier to achieve, where quantum degeneracy is not required. We note, however, that the inclusion of explicitly finite-duration pulses drastically increases the time necessary for a finite temperature simulation to complete, and reduces the insight gained from finite-temperature simulations performed for the case of δ-kicks [3]. Also, for the case of the measurement of small lattice depths, one often assumes a regime of "weak diffraction", in which models include only the contribution of zeroth and first diffraction orders. Though this is a successful rule of thumb provided the lattice depth is sufficiently small, it is not clear from the literature exactly how far this domain of validity extends, or how great a role is played by the effects of population leakage into higher diffraction orders (which we show can be treated analytically in principle), and finite-temperature initial distributions.

Where these models have been extended in order to avoid these common approximations, for instance by exhaustive and time consuming numerical modeling, one often loses the intuitive picture that a simpler, but more powerful model may offer. In this thesis we propose and investigate modeling approaches for these diffraction experiments which we argue are as simple as possible whilst still capturing the essential dynamical features of the experiments considered, and which offer intuitive frameworks likely to be of use to experimentalists in interpreting their results and planning future atom diffraction experiments. Further, based on these modeling techniques, we propose a new method for lattice depth characterization, which is more robust to finite-temperature effects than currently available methods.

1.2 Thesis outline

This thesis is organised as follows: In Part I we discuss the implementation of a high momentum transfer beam splitter by exploiting quantum resonances in the atom-optical pulsed particle. We present a model for such resonances based on a pseudoclassical approach, which offers significant insight over standard methods and is simpler to explore numerically. Expected momentum distributions computed using the pseudoclassical model are compared to those yielded by a fully quantum approach. In Part II we consider an ultracold atomic gas exposed to a pulsed optical lattice, report analytic and numerical results for the expected atomic diffraction patterns, and discuss implications for lattice depth characterisation using such a setup. In Part III we propose and investigate a new approach to characterising optical lattice depths where an ultracold atomic gas is exposed to a walking standing wave.

1.3 Publications from this work

- Benjamin T. Beswick, Ifan G. Hughes, Simon A. Gardiner, Hippolyte P. A. G. Astier, Mikkel F. Andersen, and Boris Daszuta, *ϵ-pseudoclassical model for quantum resonances in a cold dilute atomic gas periodically driven by finite-duration standing-wave laser pulses,* Phys. Rev. A **94**, 063604 (2016) [3].
  Contribution: Full text, all figures, numerical investigations of the ϵ-pseudoclassical and fully quantum models.

- Benjamin T. Beswick, Ifan G. Hughes, and Simon A. Gardiner *Lattice-depth measurement using multipulse atom diffraction in and beyond the weakly diffracting limit,* Phys. Rev. A **99**, 013614 (2019) [34]
  Contribution: Full text, all figures, numerical investigation, all derivations.

- Benjamin T. Beswick, Ifan G. Hughes, Simon A. Gardiner, *Lattice-depth measurement using continuous grating atom diffraction,* arXiv:1903.04011 (Submitted to Phys. Rev. A) [35]
  Contribution: Full text, all figures, numerical investigation, derivations in collaboration with Simon A. Gardiner

Part I

High momentum transfer beam-splitter in the atom-optical pulsed particle

Chapter 2

Introduction

Microkelvin-temperature cold-atom-gases are a useful medium for atom-optical experiments, including atom interferometry [36]. For light-pulse atom-interferometry experiments it is desirable to implement a high momentum transfer "beam splitter" [37, 38, 39], which can be realized by subjecting an atomic gas to a periodically pulsed optical standing-wave. By tuning the period of the pulse sequence to a specific value known as the Talbot time, the phenomenon of *quantum resonance* can be exploited to coherently split the atomic population of the gas in momentum space using minimal laser power.

A dilute atomic gas receiving pulses of "short" duration is well approximated by the atom-optical δ-kicked rotor Hamiltonian [31]. The atom-optical δ-kicked-rotor has long been the subject of study in the field of quantum chaos [5, 6], aided by the relative simplicity of both the classical and quantum δ-kicked rotor. This includes the existence of some analytical results, as well as the ease with which the quantum δ-kicked rotor lends itself to Fourier methods [40, 41]. Though laser pulses of truly infinitesimal duration are clearly unachievable experimentally, this model successfully describes experiments where the distance traveled by the atomic center of mass during each pulse is negligible relative to the spatial period of the standing wave [7, 8, 9, 10, 11, 12, 13, 14, 15, 16, 17, 18, 19, 20, 21, 22, 23, 24, 25, 26, 27, 28] (the so called Raman–Nath regime [33]). However, experiments indicate that finite pulse-duration effects can increase the sensitivity of atom interferometry experiments [29]. This consideration, coupled with the fact that the infinitesimal pulse approach gives erroneous

24

predictions over larger time-scales [42], motivates their incorporation into the kicked particle Hamiltonian. Though finite duration pulse atom interferometers have been investigated numerically for a single pulsed-particle [33], an investigation for a thermal gas of kicked particles is absent from the literature.

A possible reason for this absence is that simulating driven systems with finite-duration pulses is notably more numerically complex than simulating systems with δ-kicks [33], and this problem scales substantially with the number of particles. Given that knowledge of how the momentum distribution changes over time is necessary for designing and operating light-pulse atom-interferometry experiments, we are motivated to introduce a computationally simpler model, which can give accurate results for a typical experimental set-up.

In this Part we introduce an ϵ-pseudoclassical model for the quantum kicked particle conceptually similar to that introduced to describe quantum accelerator modes by Fishman, Guarneri and Rebbuzzini [43, 44]. This model is attractive due to its mathematical simplicity and the minimal computational complexity of the numerics. We explore the predictions of this model using a Monte Carlo approach, and compare the results to a fully quantum treatment. We find that the model captures the essential features of quantum resonant dynamics in finite-temperature driven gases.

Part I is organised as follows: in Chapter 3 we overview experimental considerations, and describe the model system Hamiltonian and the time-evolution it generates; in Chapter 4 we derive how to treat the existence of finite-duration pulses (assuming we are in the equivalent to a quantum-resonant regime for the δ-kicked rotor) using an ϵ-pseudoclassical model; in Chapter 5 we describe the Monte Carlo methodologies we use to determine our numerical results; in Chapter 6 we compare and contrast numerical results using both full quantum dynamics and the pseudoclassical model.

Chapter 3

System overview

3.1 Experimental considerations

As a typical system, one can consider a cloud of 10^5 Cesium 133 atoms. This can be relatively straightforwardly confined and cooled in a MOT (magneto-optical trap), followed by an optical molasses, to a temperature of $\sim 5\mu$K. In such a regime the resulting cold-atom gas is sufficiently dilute that atom–atom interactions can typically be neglected. Even lower temperatures can be achieved by Raman-sideband-cooling [45], or by cooling to quantum degeneracy [22, 28] (inter-atomic interactions can be significant within a Bose–Einstein condensate, however these can in principle be substantially tuned away by exploiting an appropriate magnetic Feshbach resonance [46, 47, 48, 49, 50], or letting the cloud expand).

The atomic cloud can then be released under gravity, while two counter-propagating laser beams of wavelength λ_L (choosing $\lambda_L = 852$nm corresponds to the wavelength of the cesium D_2 transition) form a laser standing wave in the vertical direction (see Fig. 3.1), which can be periodically pulsed [7, 8, 9, 10, 11, 12, 13, 14, 16, 17, 18, 19, 20, 21, 22, 23, 24, 25, 26, 27, 28]. By carefully tuning the phase-shifter element in Fig. 3.1, the laser beams will form a "walking wave," appearing as a standing wave in a frame comoving with the local gravitational acceleration [1, 2]. Neglecting interactions allows for a theoretical description using a single-particle Hamiltonian, which we describe in Chapter 3.2.
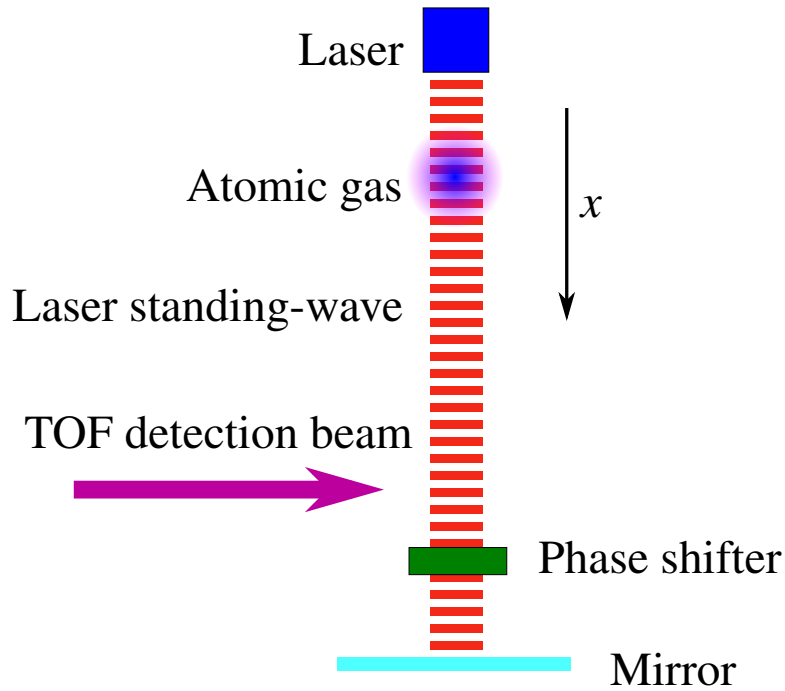
Figure 3.1: Schematic of a possible experimental setup [1]. If vertically oriented, the effect of the gravitational field can be transformed away [2] by use of the phase shifter element, for example an electro-optic modulator [1].

After receiving a set number of laser pulses, a time-of-flight measurement can be performed to determine the momentum distribution of the gas (and thence its momentum variance). These experimental observables are typically what one would measure in light-pulse atom-interferometry experiments (see Chapter 3.4), and we explain how they may be predicted numerically in Chapter 5.

3.2 System Hamiltonians

During a laser pulse, the appropriate single-particle Hamiltonian describes a two-level atom (ground state $|g\rangle$ and excited state $|e\rangle$) of mass M coupled to a laser standing wave of angular

frequency ω_L, wavenumber $k_L \equiv 2\pi/\lambda_L$, and phase ϕ [51, 52]:

$$\hat{H}_{2\text{L}} = \frac{\hbar\omega_0}{2}\left(|e\rangle\langle e| - |g\rangle\langle g|\right) + \frac{\hat{p}^2}{2M} + \frac{\hbar\Omega}{2}\cos(k_L\hat{x})\left[e^{-i(\omega_L t-\phi)}|e\rangle\langle g| + \text{H.c.}\right], \tag{3.2.1}$$

where Ω is the on-resonance Rabi frequency, t is the time, and H.c. stands for Hermitian conjugate. Here, $\hat{x}$ and $\hat{p}$ represent the atomic position and momentum along the axis of the laser standing wave.[a] Transforming to an appropriate rotating frame, and adiabatically eliminating the excited state (assuming the laser field to be far-detuned and that all population begins in the ground state also justifies our neglect of spontaneous emission) results in the Hamiltonian [51]

$$\hat{H}''_{2\text{L}} = \frac{\hat{p}^2}{2M} - \frac{\hbar\Omega^2}{8\Delta}\cos(2k_L\hat{x}), \tag{3.2.2}$$

where we have defined[b] $\Delta \equiv \omega_0 - \omega_L$. We describe the standing wave being periodically switched on and off through the dimensionless time-dependent function $f(t)$, giving

$$\hat{H} = \frac{\hat{p}^2}{2M} - \hbar\phi_d\cos(K\hat{x})\frac{f(t)}{t_p}, \tag{3.2.3}$$

where we have introduced $K \equiv 2k_L$ and $\phi_d \equiv \Omega^2 t_p/8\Delta$. The function $f(t) = \sum_{n=-\infty}^{\infty} F_{\text{sq}}(t - nT, t_p)$, where

$$F_{\text{sq}}(t, t_p) = \begin{cases} 1 & \text{for } 0 < t \leq t_p, \\ 0 & \text{for } t \leq 0 \text{ or } t > t_p. \end{cases} \tag{3.2.4}$$

describes a square pulse of duration t_p. This is typically a reasonable description of atom optical experiments [9]. As $t_p \to 0$, then $f(t)/t_p \to \sum_{n=-\infty}^{\infty}\delta(t - nT)$, and in this limit Eq. (3.2.3) reduces to the familiar δ-kicked particle Hamiltonian described in [51].

---

[a]We may consider the center-of-mass dynamics in the x direction in isolation, as they separate from the remaining center-of-mass degrees of freedom.

[b]Note that the detuning is usually defined as equal to $\omega_L - \omega_0$ [53] and thus is equal to $-\Delta$ as defined in this paper. Within the context of atom-optical δ-kicked rotors the convention used in this paper is typical, however [8, 15].

3.3 Time evolution

The time-periodicity of the Hamiltonian allows us to define a Floquet operator $\hat{F}$, such that $|\psi_{n+1}\rangle = \hat{F}|\psi_n\rangle$, where $|\psi_n\rangle$ denotes the state of the system immediately before the nth kick:

$$\hat{F} = \hat{U}_{\text{Free}}\hat{U}_{\text{Kick}} = \exp\left(-i\frac{\hat{p}^2}{2M}\frac{[T - t_p]}{\hbar}\right) \times \exp\left(-i\left[\frac{\hat{p}^2}{2M} - \frac{\hbar\phi_d}{t_p}\cos(K\hat{x})\right]\frac{t_p}{\hbar}\right), \quad (3.3.1)$$

where $\hat{U}_{\text{Free}}$ governs the "between-kick" free evolution, and $\hat{U}_{\text{Kick}}$ governs the time evolution while the kick is applied.

The spatial periodicity in $\hat{x}$ of Eq. (3.2.3) allows us to invoke Bloch theory [54]. It is therefore convenient to partition the position and momentum operators [55], such that:

$$K\hat{x} = 2\pi\hat{l} + \hat{\theta}, \quad (3.3.2a)$$

$$\hat{l}|Kx = 2\pi l + \theta\rangle = l|Kx = 2\pi l + \theta\rangle, \quad (3.3.2b)$$

$$\hat{\theta}|Kx = 2\pi l + \theta\rangle = \theta|Kx = 2\pi l + \theta\rangle, \quad (3.3.2c)$$

where $l \in \mathbb{Z}$ and $\theta \in [0, 2\pi)$ is effectively an angle variable; and

$$(\hbar K)^{-1}\hat{p} = \hat{k} + \hat{\beta}, \quad (3.3.3a)$$

$$\hat{k}|(\hbar K)^{-1}p = k + \beta\rangle = k|(\hbar K)^{-1}p = k + \beta\rangle, \quad (3.3.3b)$$

$$\hat{\beta}|(\hbar K)^{-1}p = k + \beta\rangle = \beta|(\hbar K)^{-1}p = k + \beta\rangle, \quad (3.3.3c)$$

with $k \in \mathbb{Z}$ and $\beta \in [-1/2, 1/2)$. We now can speak of k as the discrete part of the dimensionless momentum $(\hbar K)^{-1}p$, and β as the continuous part or *quasimomentum*.

Fourier analysis of the Floquet operator $\hat{F}$ reveals that only momentum states separated by integer multiples of $\hbar K$ are coupled [18], and so β must be a conserved quantity; in other words $[\hat{\beta}, \hat{H}] = 0$ [16, 55]. Within any specified quasimomentum subspace we can therefore consider the time evolution to be governed by

$$\hat{F}(\beta) = \exp\left(-i\frac{[\hbar K(\hat{k} + \beta)]^2}{2M}\frac{[T - t_p]}{\hbar}\right) \times \exp\left(-i\left\{\frac{[\hbar K(\hat{k} + \beta)]^2}{2M} - \frac{\hbar\phi_d}{t_p}\cos(\hat{\theta})\right\}\frac{t_p}{\hbar}\right). \quad (3.3.4)$$

We now have a continuum of Floquet operators, one for each β subspace, within which β can be considered simply a number [43, 44, 55]. For the most general time evolutions one should in principle take relative phases between these subspaces into account, however this can be neglected if we do not consider coherent superpositions of states with different values of β.

3.4   Quantum resonance, antiresonance and time reversal

For the δ-kicked rotor, quantum resonance occurs when the free evolution between kicks has no net effect on the state of the system [5, 16, 31, 40, 56, 57]. Referring to Eq. (3.3.4) when $\beta = 0$ and $t_p \rightarrow 0$, this corresponds formally to requiring $\hat{U}_{\text{Free}}$ to collapse to the identity operator. Recalling that $\hat{k}$ has integer eigenvalues, this is fulfilled when

$$T = T_T \equiv \frac{4\pi M}{\hbar K^2} \, , \tag{3.4.1}$$

or any integer multiple thereof. The quantity T_T is known as the *Talbot time* [1, 58], in analogy with the *Talbot length* of optics [59]. Within the $\beta = 0$ subspace (which maps exactly to the case of the quantum δ-kicked rotor, with its intrinsically discrete angular momentum spectrum), adjusting the period to an integer multiple of the Talbot time gives rise to an exactly quadratic increase in $\langle \hat{p}^2 \rangle$ over time, given by $\langle \hat{p}^2 \rangle_n = \hbar^2 K^2 \phi_d^2 n^2 / 2$ [57, 60], where n is the number of kicks.

Assuming the initial momentum distribution is symmetric about a mean value of zero, such ballistic growth of the system energy occurs via significant population being transferred into high-magnitude momentum states of opposite value (leading, at low temperatures, to a distribution with large, negative *kurtosis* [57]). This splitting of the atomic momentum-distribution can form the first component of a light-pulse atom-interferometer [33, 61], acting as the atom-optical analogue of a beam-splitter in classical optics. In an interferometric experiment, a relative phase would be accumulated between the "arms" of the resultant split cloud, due to coherent evolution caused by a perturbation to be measured. At a time t_R, the laser standing-wave can be near-instantaneously phase-shifted in θ by an offset of π, which effectively reverses the quantum resonant dynamics, causing the momentum-state populations to recombine some time later. At this time the relative phase can be extracted, and

hence the magnitude of the perturbation.

For the case where the period T is set to a half integer multiple of the Talbot time a phenomenon known as antiresonance can also be observed, characterized by kick-to-kick motion where there is no net increase in $\langle \hat{p}^2 \rangle$ over time, but instead $\langle \hat{p}^2 \rangle$ alternates between two values [17, 42, 51, 60].

Chapter 4

Finite-duration pulses

4.1 Motivation for a pseudoclassical approach

In the Floquet operator for the quantum δ-kicked particle the position and momentum operators are explicitly separated, making numerical determination of the system time evolution straightforward. Incorporating finite duration pulses combines $\hat{x}$ and $\hat{p}$ in the $\hat{U}_{\text{Kick}}$ operator of Eq. (3.3.1), substantially increasing the numerical task. We are therefore motivated to introduce a simpler treatment, based on ϵ-*pseudoclassics*, which is intended to approximate the fully quantum treatment in an appropriate regime; similar treatments can be found in [44, 55, 62, 63, 64]. The evolution of a quantum particle or ensemble of quantum particles is modeled by a Monte Carlo simulation of an ensemble of pseudoclassical particles (described in Chapter 5), attractive both due to its computational simplicity and dynamical insight.

4.2 Derivation of the pseudoclassical model

We begin with the Floquet operator corresponding to the kicked-particle Hamiltonian, restricted to a particular β subspace [Eq. (3.3.4)], together with the constraint $T = \ell T_T / 2$ (where ℓ is an even integer — this corresponds to the condition for quantum resonance for the δ-kicked particle). Introducing the dimensionless pulse duration $\epsilon = \hbar K^2 t_p / M$, we may

rewrite Eq. (3.3.4) as

$$\hat{F}(\beta) = \exp\left(i\left[\frac{\hat{k}^2}{2}\epsilon + \hat{k}\beta(\epsilon - 2\pi\ell)\right]\right) \times \exp\left(-i\left[\frac{\hat{k}^2}{2}\epsilon + \hat{k}\beta\epsilon - \phi_d\cos(\hat{\theta})\right]\right). \tag{4.2.1}$$

We now define a rescaled and shifted discrete momentum $\hat{\mathcal{J}}(\beta) = (\hat{k} + \beta)\epsilon$, leading to the commutator $[\hat{\theta}, \hat{\mathcal{J}}(\beta)] = i\epsilon$. Introducing the rescaled kicking strength $\tilde{V} = \epsilon\phi_d$, we can now rewrite Eq. (4.2.1) as

$$\hat{F}(\beta) = \exp\left(\frac{i}{\epsilon}\left[\frac{\hat{\mathcal{J}}(\beta)^2}{2} - \hat{\mathcal{J}}(\beta)2\pi\ell\beta\right]\right) \times \exp\left(-\frac{i}{\epsilon}\left[\frac{\hat{\mathcal{J}}(\beta)^2}{2} - \tilde{V}\cos(\hat{\theta})\right]\right). \tag{4.2.2}$$

Note that ϵ appears where we would normally expect to see $\hbar$; for small values of ϵ, we therefore expect an effective classical model to give reasonable results which well approximate the quantum treatment [44, 55, 62, 63, 64].

The dynamics governed by Eq. (4.2.2) are equivalent to those generated by the following dimensionless Hamiltonians:

$$\hat{H}_1 = \frac{\hat{\mathcal{J}}(\beta)^2}{2} - \tilde{V}\cos(\hat{\theta}), \tag{4.2.3a}$$

$$\hat{H}_2 = -\frac{\hat{\mathcal{J}}(\beta)^2}{2} + \hat{\mathcal{J}}(\beta)2\pi\ell\beta, \tag{4.2.3b}$$

where $\hat{H}_1$ is associated with the kick, $\hat{H}_2$ with the free evolution, and each Hamiltonian governs the time-evolution for one dimensionless time unit (rescaled time given by t/t_p). Replacing the quantum Hamiltonian $\hat{H}_1$ with its classical counterpart H_1, we determine Hamilton's equations of motion:

$$\dot{\theta}(\beta) = \frac{\partial H_1}{\partial \mathcal{J}(\beta)} = \mathcal{J}(\beta), \tag{4.2.4a}$$

$$\dot{\mathcal{J}}(\beta) = -\frac{\partial H_1}{\partial \theta(\beta)} = -\tilde{V}\sin(\theta(\beta)), \tag{4.2.4b}$$

which we recognize as the equations of motion of a simple pendulum, the phase space orbits of which are in principle exactly solvable in terms of Jacobi elliptic functions (although they can be more convenient to solve numerically). Referring to a phase space point immediately before the nth kick as $(\theta_n(\beta), \mathcal{J}_n(\beta))$, we say that evolving these values under Eq. (4.2.4)

for 1 dimensionless time unit yields $(\theta_{n^+}(\beta), \mathcal{J}_{n^+}(\beta))$. Feeding these values into the classical equations of motion generated by H_2 yields the very simple classical map

$$\theta_{n+1}(\beta) = \theta_{n^+}(\beta) - \mathcal{J}_{n^+}(\beta) + 2\pi\ell\beta, \tag{4.2.5a}$$

$$\mathcal{J}_{n+1}(\beta) = \mathcal{J}_{n^+}(\beta), \tag{4.2.5b}$$

where $(\theta_{n+1}(\beta), \mathcal{J}_{n+1}(\beta))$ is the phase space point evolved to just before the $(n + 1)^{\text{th}}$ kick [3].

Finally, relating the dimensionless momentum $\mathcal{J}(\beta)$ back to the momentum p yields:

$$p = \hbar K(k + \beta) = \frac{\hbar K}{\epsilon} \mathcal{J}(\beta). \tag{4.2.6}$$

To calculate the time evolution of expectation values using this treatment, we evolve an appropriate initial ensemble of classical particles and then compute their normalized statistics, as described below.

Chapter 5

Monte Carlo simulations

5.1 Quantum Model

In our finite-temperature simulations, we follow the approach of Saunders *et al.* [51], and work within the momentum basis. The initial states are momentum eigenstates, with randomly distributed values sampled from the Maxwell–Boltzmann distribution:

$$D_k(\beta) = \frac{1}{w\sqrt{2\pi}} \exp\left(\frac{-[k+\beta]^2}{2w^2}\right), \tag{5.1.1}$$

where the temperature $\mathcal{T}_w = \hbar^2 K^2 w^2 / M k_{\mathrm{B}}$[51].

Time-evolving an initial momentum eigenstate $|(\hbar K)^{-1}p = k + \beta\rangle$ using the Floquet operator $\hat{F}(\beta)$ of Eq. (4.2.1) results in a transfer of the initial population among other momentum eigenstates, such that the time-evolved state can be written:

$$|\psi(t)\rangle_j = \sum_k^{N_q} c_{kj}(t) \, |(\hbar K)^{-1}p = k + \beta\rangle, \tag{5.1.2}$$

where $|\psi(t)\rangle_j$ is the time-evolved state corresponding the the jth of N_q initial momentum

eigenstates. The second order momentum moment is given by:

$$\langle \hat{p}^2 \rangle(t) = N_q^{-1} \sum_j^{N_q} \langle \hat{p}^2 \rangle_j(t) = N_q^{-1} \sum_j^{N_q} \langle \psi(t)| \hat{p}^2 |\psi(t) \rangle_j. \tag{5.1.3}$$

The momentum distribution can be read off from the absolute square of the coefficients $c_{kj}(t)$ for the case of a single initial momentum state, and tells us the probability of the system being in a given k subspace (some given value of k, but any value of β). For an ensemble of N_q states, the total probability $P_k(t)$ of finding an atom with a certain discrete momentum k is given by the normalized sum of the absolute squares of the $c_{kj}(t)$ coefficients, $P_k = N_q^{-1} \sum_j |c_{kj}(t)|^2$.

It is desirable for our momentum distribution plots to be log-normalized so that fine features may be resolved. In practice momentum states with higher k-values receive a negligible amount of population compared to states near $k = 0$, and so when displaying our momentum distributions we impose a cutoff value C, such that the condition $P_k \geqslant C$ is true for all P_k and t and the problem of taking the logarithm of a near-zero population is avoided.

5.2 ϵ-pseudoclassical model

In the case of the ϵ-pseudoclassical model, momentum distribution dynamics are obtained by evolving a statistical ensemble of N_c classical particles according to Eq. (4.2.4) and Eq. (4.2.5) (note that N_c need not in general be equal to N_q). Though the trajectory of each particle does not in itself have a clear physical meaning, the evolution of an ensemble of sufficiently large size can be used to produce a facsimile of the quantum momentum-state-population-distribution of the gas. We place the momentum data into bins of width $\Delta p = \hbar K$, normalize the resultant population distribution and from this extract the mean squared momentum.

It is possible to produce an approximate momentum distribution also for the case of a zero temperature gas, by setting $\mathcal{J}(\beta) = 0$ and choosing a random ensemble of initial θ values; the ensemble approximates a single momentum eigenstate with a given β. For the case of a finite-temperature gas, $\mathcal{J}(\beta)$ values are randomly drawn from a Maxwell–Boltzmann distribution,

and θ values from a uniform distribution.

Chapter 6

Comparison of quantum and pseudoclassical results

6.1 Dynamics of the pseudoclassical map

To gain insight into the system dynamics, it is useful to construct $(\theta, \mathcal{J})$ Poincaré sections, which in this case are stroboscopic maps defined by Eq. (4.2.4) and Eq. (4.2.5), evolved for some number of kicks N. We remark that we have opted to solve the equations of motion generated by H_1 numerically rather than using the exact Jacobi elliptic functions for ease of implementation; this still requires vastly less computational power to solve the time evolution of the system than the Fourier methods generally used in a fully quantum treatment. Inspection of Eq. (4.2.4) and Eq. (4.2.5) reveals that there are exactly two free parameters: the driving strength $\tilde{V}$, and the quasimomentum β. We therefore construct a selection of Poincaré sections varying these, choosing $\tilde{V} = 0.251$ when we vary β (Fig. 6.1 — this value is motivated by typical experimental values [1, 18, 19, 58, 60, 65, 66, 67, 68, 69, 70]), and $\beta = 0$ when we vary $\tilde{V}$ (Fig. 6.2). The Poincaré section of Fig. 6.1(a) [repeated in Fig. 6.2(a) for ease of comparison between different β subspaces and values of $\tilde{V}$] corresponds to that of an exact quantum resonance in the δ-kicked particle case (for which the dynamical behaviour varies from resonant to antiresonant, depending on the value of β [2, 51, 57]). There are two stable fixed points visible at (0,0) and $(-\pi, 0) \equiv (\pi, 0)$, each surrounded by concentric or-
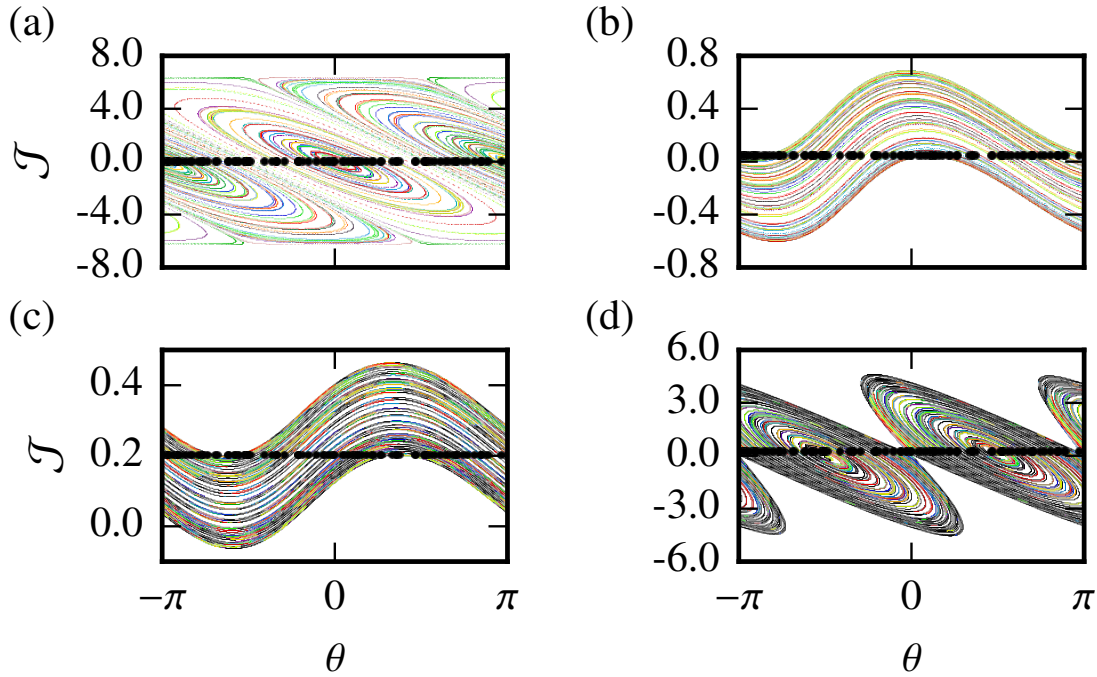
Figure 6.1: Poincaré sections for $(\theta, \mathcal{J}(\beta))$ as evolved by Eq. (4.2.4) and Eq. (4.2.5), corresponding to the $\beta = 0$, 0.05, 0.2, and 0.25 subspaces for (a), (b), (c), and (d) respectively, with $\ell = 2$ and $\tilde{V} = 0.251$. Each black circle represents one of 100 initial phase-space points, and each color represents the evolution of a single phase-space point over 1000 kicks. The smaller black points in (c) and (d) link up the rotational or elliptic orbits, respectively, (which for $\beta = 0.2$ and $\beta = 0.25$, respectively, takes substantially longer than 1000 kicks).

bits characteristic of regular (non-chaotic) motion. Fig. 6.1 (d) corresponds to the $\beta = 0.25$ subspace, which we expect to behave as an antiresonance in the δ-kicked limit. Clearly the system dynamics vary dramatically between different β subspaces, and we must therefore consider them all when modelling a thermal gas.

In Fig. 6.2 we see that, as we increase the driving strength $\tilde{V}$ from $\tilde{V} = 0.251$, a region of pseudorandom trajectories opens up in the outer parts of each system of elliptic orbits, until the Poincaré section becomes predominantly chaotic for $\tilde{V} = 7.51$. We remark that such high values of $\tilde{V}$, combined with small values of ϵ, correspond to very high laser intensities, making it unclear what the transition to chaos in the ϵ-pseudoclassical model really represents in an atom-optical context.
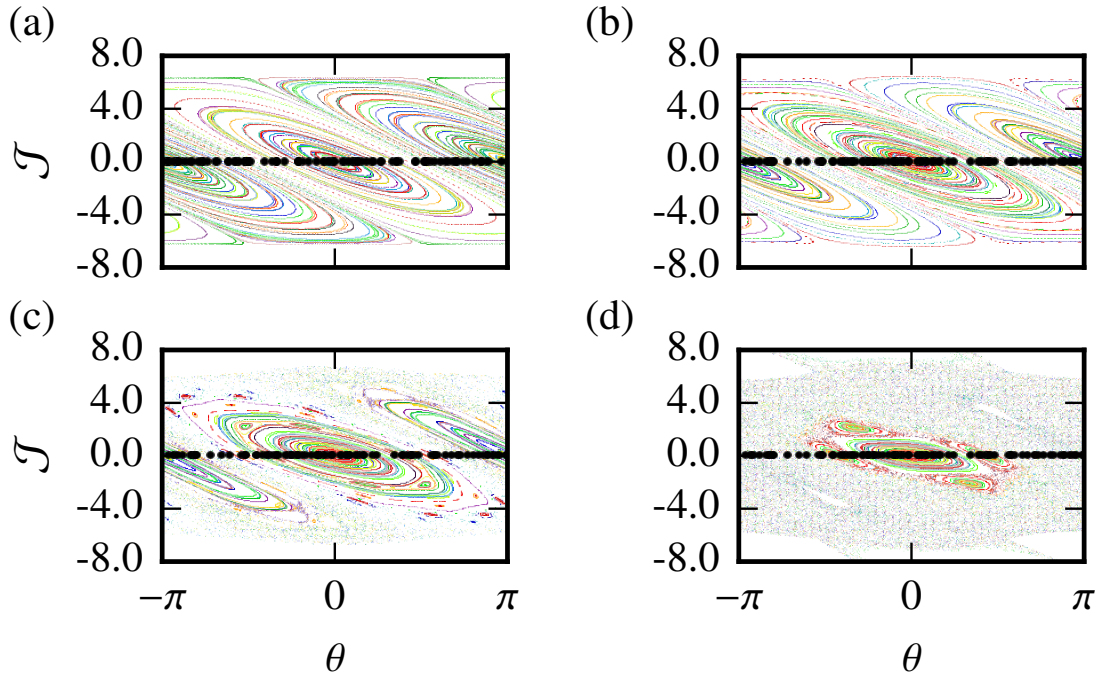
Figure 6.2: Poincaré sections for $(\theta, \mathcal{J}(\beta))$ as evolved by Eq. (4.2.4) and Eq. (4.2.5), corresponding to the $\beta = 0$ subspace for driving strengths $\tilde{V} = 0.251, 2.51, 5.01,$ and 7.51 for (a), (b), (c), and (d) respectively, with $\ell = 2$. Each black circle represents one of 100 initial phase-space points, and each color represents the evolution of a single phase-space point over 1000 pulses.

6.2 Zero-temperature gas

We now compute the evolution of $\langle \hat{p}^2 \rangle$ over time for a range of values of ϵ and constant ϕ_d (meaning that $\tilde{V} \equiv \epsilon \phi_d$ scales linearly with ϵ), using both the pseudoclassical and fully quantum calculations, at zero temperature. This is actually computationally straightforward in the quantum case, as one need only evolve a single initial (zero momentum) eigenstate.

We display our results in Fig. 6.3(a). Two behaviors are clearly visible:

1. As ϵ increases, the approximate pseudoclassical simulations deviate from the quantum dynamics after a smaller number of pulses. As this model relies on an expansion about ϵ as a small parameter, this deviation can be thought of as a cumulative error in the
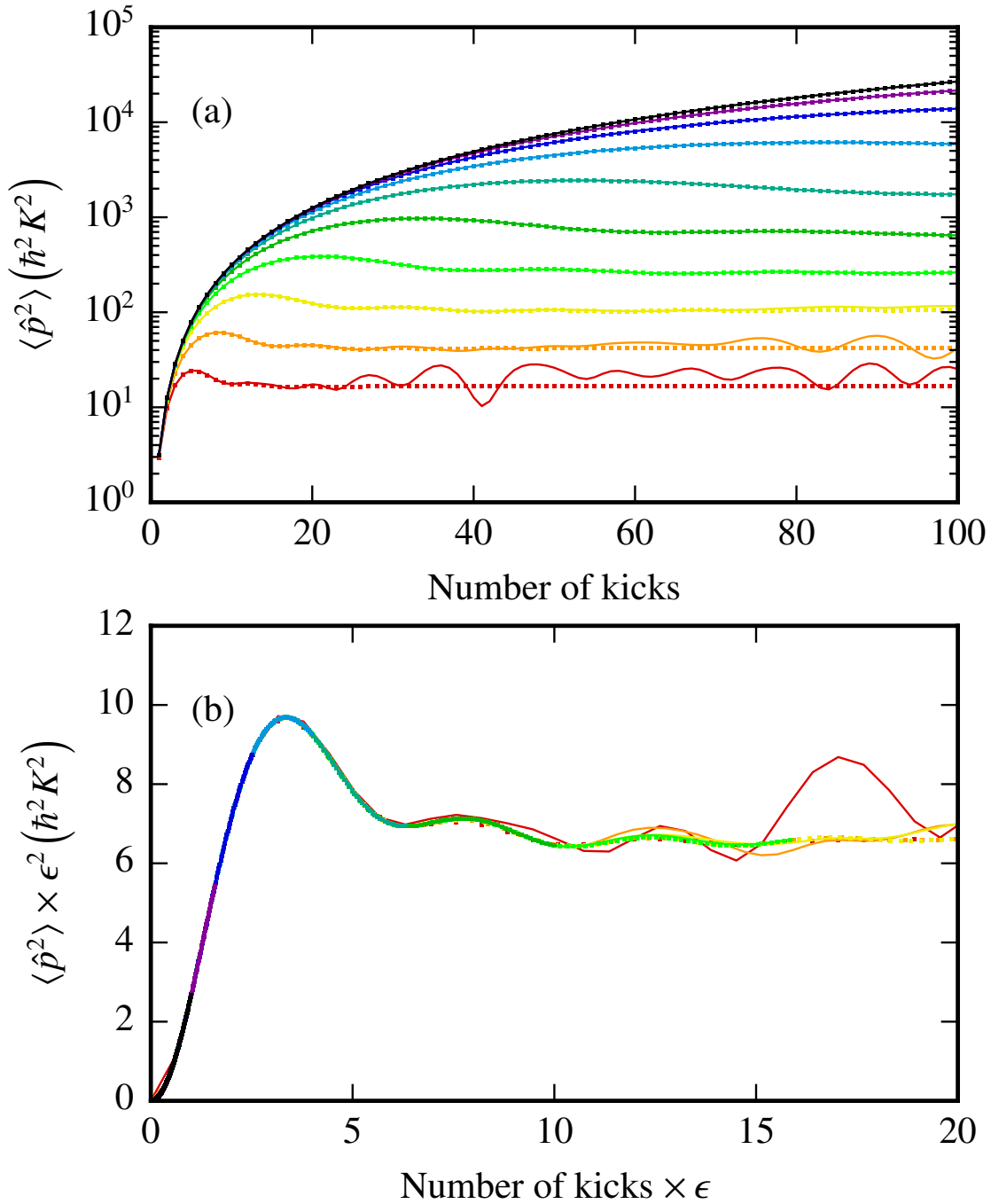
Figure 6.3: (a) Plot of $\langle \hat{p}^2 \rangle$ in units of $\hbar^2 K^2$ vs. number of kicks for a zero temperature gas, with $\phi_d = 0.8\pi$ and $\ell = 2$. The scaled pulse duration ϵ takes the values $10^{-2+2j/11}$, where $j = \{0, 1, 2, .., 10\}$. The curves represent the results of the quantum dynamics [Eq. (3.3.1)], and the points those of the ϵ-pseudoclassical model [Eq. (4.2.4) and Eq. (4.2.5)], with lower values of ϵ giving rise to higher peak values of $\langle \hat{p}^2 \rangle$. Hence, the black curve corresponds to $\epsilon = 0.01$ ($j = 0$) and the red curve to $\epsilon = 0.658$ ($j = 10$). (b) Rescaling of (a) by ϵ^2 in the $\langle \hat{p}^2 \rangle$ axis and ϵ in the kick-number axis such that a universal curve is revealed, where all data overlap over a suitably short timescale.

pseudoclassical dynamics that increases in magnitude each time the classical maps are applied. Results like those of Fig. 6.3(a) allow us to characterize time scales over which we can expect agreement between the pseudoclassical and quantum treatments for a given value of ϵ.

2. The peak value of $\langle \hat{p}^2 \rangle$ is higher for smaller values of ϵ. Recalling that ϵ is simply a rescaled pulse duration, as it approaches zero the system behaves increasingly as if it were receiving δ-kicks, for which $\langle \hat{p}^2 \rangle$ would increase indefinitely over time. It is again clear that the smaller the value of ϵ, the longer the timescale over which the system behaves as if it were δ-kicked. At an ϵ-dependent point in time, $\langle \hat{p}^2 \rangle$ deviates from the quadratic growth associated with perfect quantum resonance, corresponding to violation of the Raman–Nath regime. We can see that $\langle \hat{p}^2 \rangle$ must eventually decrease by inspection of the phase space diagram in Fig. 6.1(a), as the spread of trajectories is forced to eventually decrease simply because they manifest as bounded quasiperiodic orbits.

Rescaling the axes in Fig. 6.3(a) according to the value of ϵ reveals a universal curve, which exists independent of this value, as displayed in Fig. 6.3(b). This universality appears to be essentially exact in the pseudoclassical model, but ceases to apply for the quantum calculations once they deviate significantly from the pseudoclassical predictions. The observed oscillating decay encapsulates the dynamics visible in Fig. 6.1(a), and appears indicative of the dephasing of an ensemble of anharmonic oscillators.

6.3 Quasimomentum dependence

Figure 6.4 shows comparisons of $\langle \hat{p}^2 \rangle$ evolution as computed by the quantum and ϵ-pseudoclassical models for initial conditions corresponding to a single momentum eigenstate with $k = 0$ and different values of β. The pseudoclassical and quantum models agree well over the entire range of β subspaces. Hence, for any reasonable initial momentum distribution, we can expect the pseudoclassical model to reproduce the correct quantum dynamics provided that ϵ is small enough on the timescale to be considered. We have chosen $\epsilon = 0.001$ for Fig. 6.4(a), where the dynamics are essentially coincident with those induced by perfect
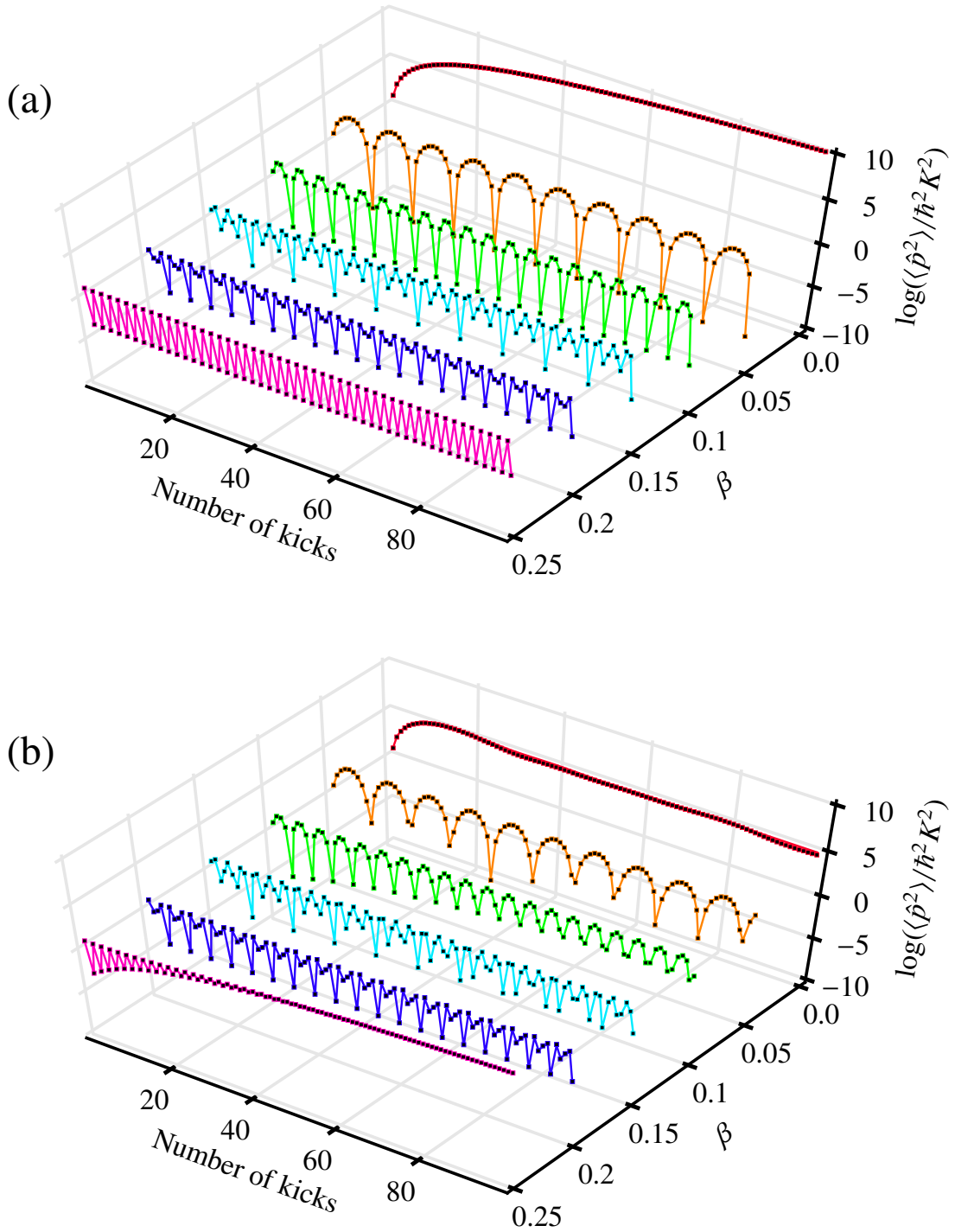
Figure 6.4: Plots of the time evolution of the log of $\langle \hat{p}^2 \rangle$ in units of $\hbar^2 K^2$ vs. number of kicks, for different values of the quasimomentum $\beta = \{0, 0.05, 0.1, 0.15, 0.2, 0.25\}$, for an otherwise zero temperature gas [initial momentum eigenstate with $\mathcal{J}(\beta) = 0$]. The smooth curves represent results of the quantum evolution [Eq. (3.3.1)], and the points those of the effective classical model [Eq. (4.2.4) and Eq. (4.2.5)]. For figure (a) $\epsilon = 0.001$, and for figure (b) $\epsilon = 0.2$. Other parameters are $\phi_d = 0.8\pi$ and $\ell = 2$.

δ-kicks for the chosen parameters and pulse numbers. In Fig. 6.4(b) we have $\epsilon = 0.2$; comparing with Fig. 6.4(a) it is clear that time evolution of $\langle \hat{p}^2 \rangle$ is significantly affected by the finite duration of the pulses. Note, however, that although $\epsilon = 0.2$ would seem to be borderline in terms of being a "small parameter," the agreement between the ϵ-pseudoclassical model and the full quantum dynamics still appears to be excellent.

As β increases from 0 the evolution of $\langle \hat{p}^2 \rangle$ over time progresses from resonant to antiresonant behavior. This progression is twofold periodic in the space of quasimomenta: Eq. (4.2.5) shows that for $\ell = 2$ the same pseudoclassical dynamics are observed for $\beta + 1/2$ as for β (this symmetry can also be deduced for expectation values derived from the fully quantal Floquet operator [Eq. (4.2.2)] acting on momentum eigenstates [51]). Furthermore, the Hamiltonian is an even function of both $\hat{p}$ and $\hat{x}$, meaning that the same $\langle \hat{p}^2 \rangle$ dynamics are observed for $-\beta$ as for β. Hence, the data plotted in Fig. 6.4 effectively spans the full range of β dependencies when the initial value of $\mathcal{J}(\beta)$ (or k) is 0.

6.4 Finite temperature Monte Carlo

We now perform comparative quantum and pseudoclassical Monte Carlo simulations for experimentally achievable timescales. The initial finite temperature ensembles are chosen by random sampling from a Maxwell–Boltzmann distribution (combined with a uniform distribution for θ in the case of the pseudoclassical dynamics), as described in section 5. In Figs. 6.5(a–f) and Figs. 6.5(h–m), we compare momentum distributions, computed for three values of ϵ, using both the pseudoclassical and quantum treatments, over a small number of pulses, at zero temperature ($w = 0$) and for Caesium atoms at $\mathcal{T}_w \simeq 5\,\mu\text{K}$ ($w = 2.5$). In Fig. 6.5(g) and Fig. 6.5(n) we show the associated values of $\langle \hat{p}^2 \rangle$ computed for each case to check that our comparison takes place within the regime of validity of the ϵ-pseudoclassical model. For the zero-temperature ($w = 0$) case, the population splitting in momentum space characteristic of a quantum resonance can be seen in both models over the full 30 pulses for $\epsilon = 0.02$. For larger values of ϵ we observe a slowing in the momentum spreading, followed by a clear plateau in the case of $\epsilon = 0.2$, which is also visible in the corresponding plot of $\langle \hat{p}^2 \rangle$.
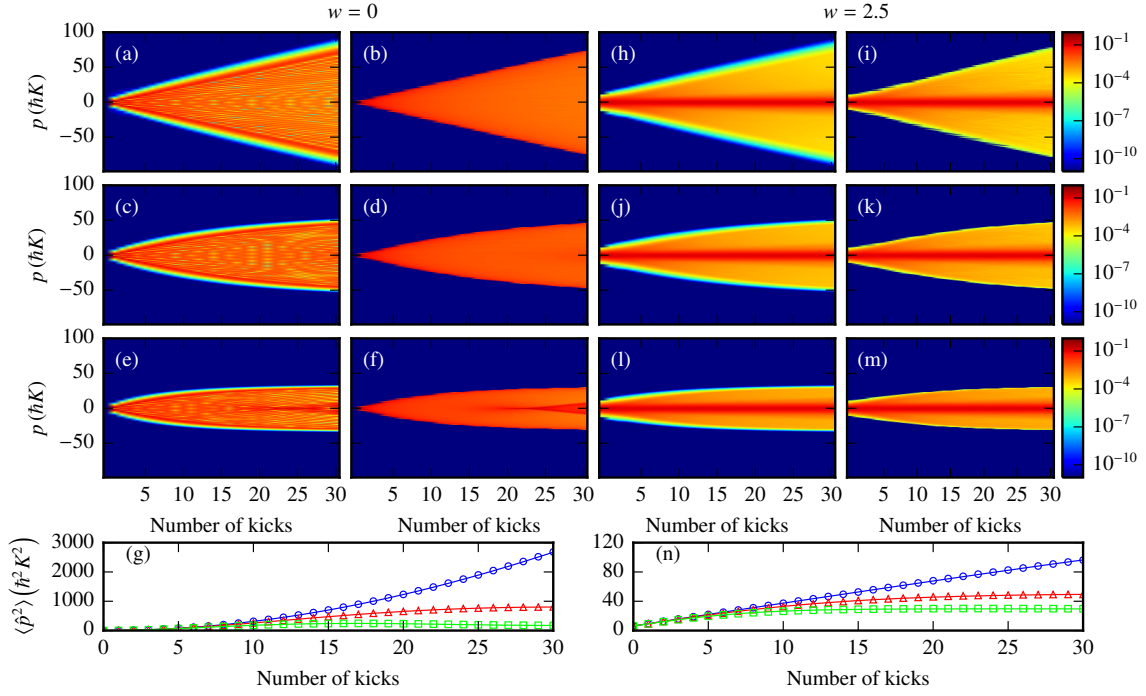
Figure 6.5: Comparison between the dynamics of the momentum distributions computed by the fully quantum model, [Eq. (3.3.1)], and the pseudoclassical model [Eq. (4.2.4) and Eq. (4.2.5)] for zero ($w = 0$) and finite temperature gases ($w = 2.5$), with $\phi_d = 0.8\pi$ and $\ell = 2$, for differing values of the scaled pulse duration ϵ. The first and second columns show momentum distributions for a zero temperature gas ($w = 0$) as computed by the quantum [(a), (c), (e)] and pseudoclassical models [(b), (d), (f)] respectively. Columns 3 and 4 give the momentum distributions computed by the quantum [(h), (j), (l)] and effective classical models [(i), (k), (m)] respectively, for $w = 2.5$. In each row, the distribution dynamics are computed for a different value of ϵ: row 1 [(a), (b), (h), (i)] has $\epsilon = 0.02$, row 2 [(c), (d), (j), (k)] has $\epsilon = 0.11$, and row 3 [(e), (f), (l), (m)] has $\epsilon = 0.2$. To accommodate the logarithmic color scale, we have chosen a cutoff value of $C = 10^{-11}$. The corresponding time-evolution of $\langle \hat{p}^2 \rangle$ [in units of $\hbar^2 K^2$] is given in (g), for $w = 0$ and (n) for $w = 2.5$; solid lines represent results of quantum calculations, and symbols those of the effective classical model (squares correspond to $\epsilon = 0.2$, triangles to $\epsilon = 0.11$, and circles to $\epsilon = 0.02$). Monte Carlo calculations were carried out with $N_c = 10^5$ particles, or $N_q = 10^5$ state vectors, as appropriate.

For each value of ϵ the overall shape of the momentum distribution computed by the ϵ-pseudoclassical model matches that of the fully quantum calculation well. A degree of internal structure is present in the zero-temperature ($w = 0$) quantum distributions that is not present in their ϵ-pseudoclassical counterparts. Similarly, in both the $w = 0$ and $w = 2.5$ quantum distributions, there is further structure visible, where the most extreme populated states in momentum space meet the near zero-population background, that is not present in the pseudoclassical calculation. We can clearly see from Fig. 6.5(g) and Fig. 6.5(n) that the evolution of $\langle \hat{p}^2 \rangle$ is nonetheless reproduced perfectly over a short time-scale. For the $w = 2.5$ case, we see a clearly defined feature centered around $p = 0$ representing a large concentration of population. This is typical of finite-temperature quantum-resonant dynamics in atom-optical systems [15, 42, 51], and can be understood from Fig. 6.4; essentially a broad initial momentum distribution means that both resonant ($\beta = 0$) and bounded antiresonant ($\beta = 0.25$) dynamics take place simultaneously, as well as the whole range of intermediate behaviour, leading to an overall averaging of the spreading in momentum space.

With atom interferometry in mind, we have repeated these simulations with the addition of a time-reversal event occurring at $n_R = 15$ pulses (as described in section 3.4), displaying our results in Fig. 6.6. In Fig. 6.6(a) and Fig. 6.6(b) ($\epsilon = 0.02$ and $w = 0$) we clearly have a near-perfect time-reversal process, with the majority of the population returning to the zero-momentum state when $n = 2n_R$. Increasing ϵ to 0.11, we can see from Fig. 6.6(c) and Fig. 6.6(d) that the asymmetry about $n = 2n_R$ has increased very slightly, and for $\epsilon = 0.2$ we can see from Fig. 6.6(e) and Fig. 6.6(f) that the asymmetry has become even larger (similar effects were observed in [33]). For $w = 2.5$, however [Figs. 6.6(h–n)], each distribution begins to refocus but then again increases in breadth (this is the same behaviour as expected for a δ-kicked atomic gas). Note that as the value of ϵ increases the final distributions become narrower, which is an effect of using finite-duration pulses. In each case the ϵ-pseudoclassical predictions give good agreement with the shapes of the momentum distributions yielded by a fully quantum treatment, with the missing edge detail around each quantum distribution only manifest at around the $P_k = 10^{-7}$ level. Crucially, it is clear that the lack of internal structure in the ϵ-pseudoclassical distributions is not a problem for calculating $\langle \hat{p}^2 \rangle$ under time-reversal or at finite-temperature. An interferometric measurement would look at deviations from a perfect time reversal, potentially motivating a study of the fidelity of a time-reversed kicked gas with finite-duration pulses, for example using a similar approach to that derived for the
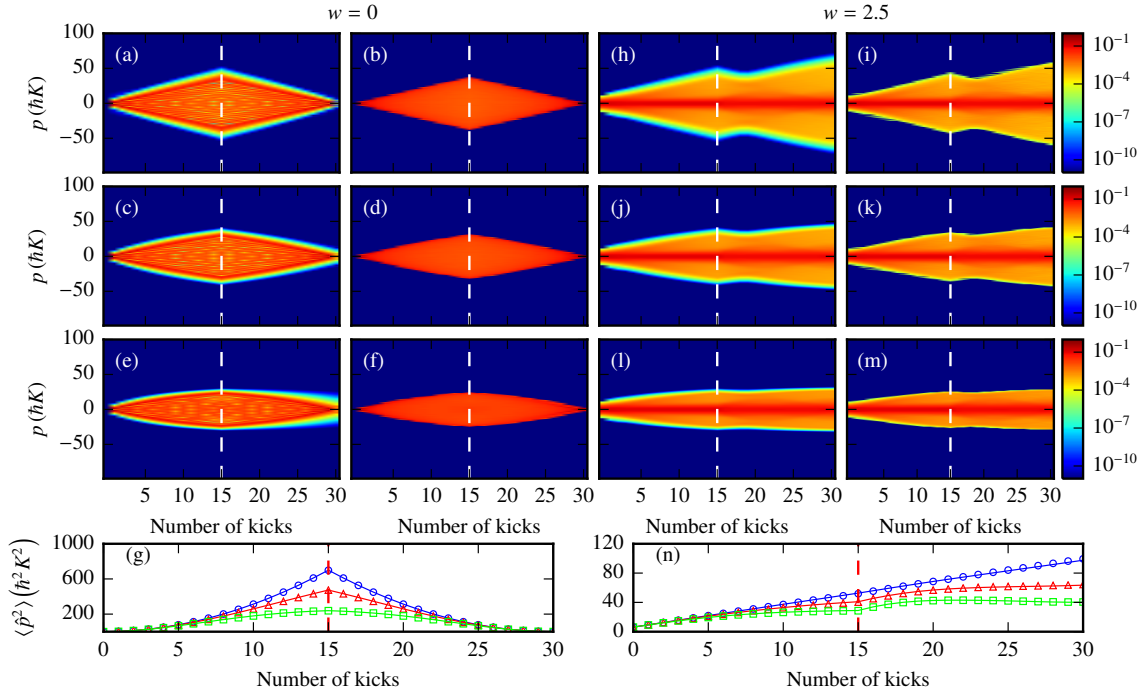
Figure 6.6: Comparison between the dynamics of the momentum distributions computed by the fully quantum model, [Eq. (3.3.1)], and the pseudoclassical model [Eq. (4.2.4) and Eq. (4.2.5)] for zero ($w = 0$) and finite temperature gases ($w = 2.5$), with $\phi_d = 0.8\pi$ and $\ell=2$, for differing values of the scaled pulse duration ϵ. In each case a time-reversal event (phase-shifting the standing wave by π) occurs at the 15th of 30 pulses (marked by the dashed lines). The first and second columns show momentum distributions for a zero temperature gas ($w = 0$) as computed by the quantum [(a), (c), (e)] and pseudoclassical models [(b), (d), (f)] respectively. Columns 3 and 4 give the momentum distributions computed by the quantum [(h), (j), (l)] and effective classical models [(i), (k), (m)] respectively, for $w = 2.5$. In each row, the distribution dynamics are computed for a different value of ϵ: row 1 [(a), (b), (h), (i)] has $\epsilon = 0.02$, row 2 [(c), (d), (j), (k)] has $\epsilon = 0.11$, and row 3 [(e), (f), (l), (m)] has $\epsilon = 0.2$. To accommodate the logarithmic color scale, we have chosen a cutoff value of $C = 10^{-11}$. The corresponding time-evolution of $\langle \hat{p}^2 \rangle$ [in units of $\hbar^2 K^2$] is given in (g), for $w = 0$ and (n) for $w = 2.5$; solid lines represent results of quantum calculations, and symbols those of the effective classical model (squares correspond to $\epsilon = 0.2$, triangles to $\epsilon = 0.11$, and circles to $\epsilon = 0.02$). Monte Carlo calculations were carried out with $N_c = 10^5$ particles, or $N_q = 10^5$ state vectors, as appropriate.

δ-kicked rotor in [71].

Having carried out a detailed comparison of the quantum and ϵ-pseudoclassical models over relatively short time scales and at finite temperature, we can reasonably assume that whatever value we select for w, the pseudoclassical model will produce accurate results, provided an appropriate value of ϵ is chosen. To better understand the variation of $\langle \hat{p}^2 \rangle$ with temperature over longer time scales, we have carried out simulations for six values of w, using only the ϵ-pseudoclassical model (results displayed in Fig. 6.7). We choose $\epsilon = 0.2$ for each simulation, as this is a relatively large value where we have already shown excellent agreement in $\langle \hat{p}^2 \rangle$ with the fully quantum treatment over a range of 100 pulses (see Fig. 6.4). Plotting $\langle \hat{p}^2 \rangle / w^2$ versus the number of kicks n, the $n = 0$ value for each curve is the same, but from $n = 1$ they separate markedly — the lower the value of w, the greater the relative increase, due to the increased dominance of quantum-resonant behavior centered at $\beta = 0$. The computational simplicity of the pseudoclassical model means that such a plot can be produced in a few minutes on a standard desktop computer, which is potentially invaluable when planning a hypothetical atom-interferometry experiment.
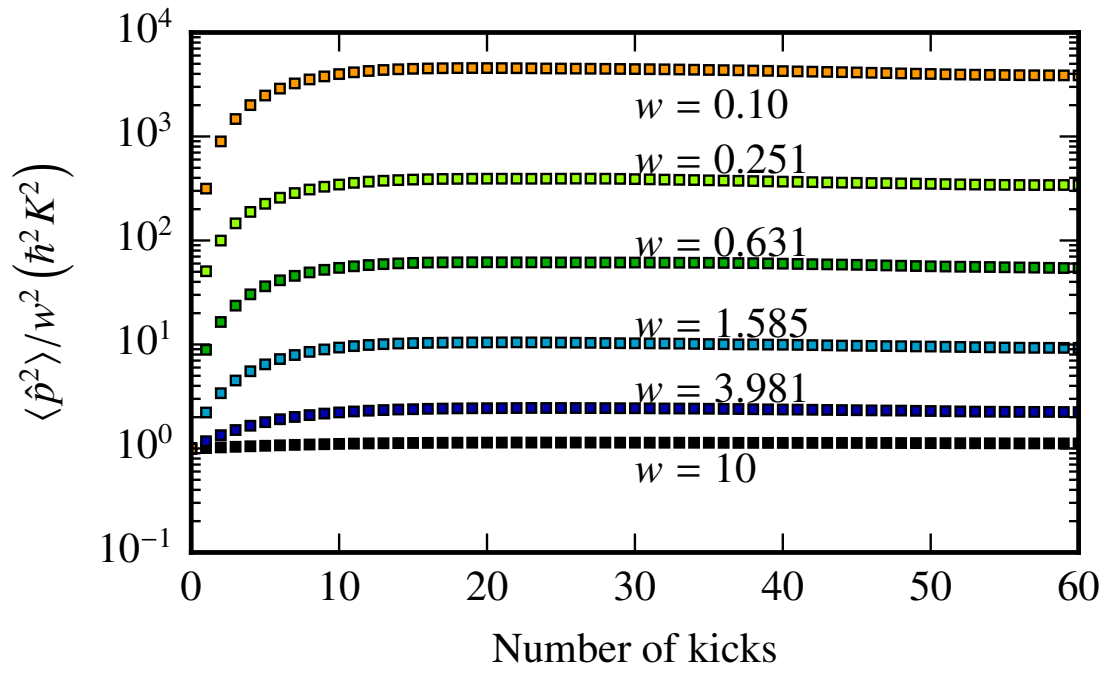
Figure 6.7: Plots of the time evolution of $\langle \hat{p}^2 \rangle/w^2$ in units of $\hbar^2 K^2$ vs. number of kicks, with $\epsilon = 0.2$, $\phi_d = 0.8\pi$ and $\ell = 2$. Each set of points corresponds to an individual value of $w = 10^{-1+2j/5}$, where $j = \{0, 1, 2, ..., 5\}$, as computed by the pseudoclassical model [Eq. (4.2.4) and Eq. (4.2.5)].

> **Chapter Summary**
>
> - We have derived an ϵ-pseudoclassical model for quantum resonances in a finite-temperature dilute atomic gas driven by finite-duration off-resonant laser pulses, and compared to its fully quantum counterpart. We have investigated the dynamics of the ϵ-pseudoclassical model and identified certain phase space features associated with quantum resonant behavior.
>
> - We have further shown how increasing the parameter ϵ shortens the time-scale over which the quantum and ϵ-pseudoclassical calculations agree at zero temperature, as well as the amount of time before a quantum resonance begins to plateau due to violation of the Raman–Nath regime. We have shown that the accuracy of the ϵ-pseudoclassical model is unaffected by the initial state's quasi-momentum, and is therefore suitable for treating a finite-temperature gas. We have explicitly performed Monte Carlo simulations to this end and compared both the expectation value $\langle \hat{p}^2 \rangle$ and momentum distributions as computed by each model, and found that the ϵ-pseudoclassical model reproduces the $\langle \hat{p}^2 \rangle$ essentially exactly, even at finite temperature, and the general shape of the associated momentum distributions up to small details.
>
> - We have also shown explicitly that the ϵ-pseudoclassical model correctly treats the time-reversal mechanism necessary for light-pulse atom-interferometry.
>
> - Finally, we have performed ϵ-pseudoclassical Monte Carlo simulations to determine the behavior of $\langle \hat{p}^2 \rangle$ at different values of w for a large number of kicks. We expect this approach to be useful in quantifying the suitability of particular experimental parameter regimes for light-pulse atom interferometry.

Part II

Lattice depth characterisation using multipulse atom diffraction

Chapter 7

Introduction

Precision measurement of optical lattice [4] depths is important in a broad range of fields in atomic and molecular physics [72, 73], most notably in atom interferometry [36, 61], many body quantum physics [74, 75], accurate determination of transition matrix elements [76, 77, 78, 79, 80], and, by extension, ultraprecise atomic clocks [81, 82]. Lattice depth measurement schemes include methods based on parametric heating [83], Rabi oscillations [84], and sudden lattice phase shifts [85]. The most commonly used scheme is Kapitza-Dirac scattering [86], where an ultracold atomic gas is exposed to a pulsed laser standing wave and theoretical predictions for the fraction of atoms found in each of the allowed momentum states are fit to time of flight measurements to determine the lattice depth [75, 87, 88, 89]. However, when determining the matrix elements of weak atomic transitions, the lattice depths involved are correspondingly small ($V \lesssim 0.01 E_{\mathrm{R}}$ for any atom, were V is the lattice depth and E_{R} is the laser recoil energy), such that signal-to-noise considerations become an issue [90].

Recently, the work of Herold *et al.* and of Kao *et al.* [30, 32] has suggested that this complication can be mitigated by using multiple laser standing wave pulses, and alternating each with a free evolution-stage, both with duration equal to half the Talbot time [21, 24, 91], such that the population in the first diffraction order is coherently added to with each pulse, improving contrast relative to the zeroth order.[a]

---

[a]In practice, this additive effect is only maintained for a certain number of pulses set by the lattice depth, as

The modeling approach taken in [30, 32] is valid for a weak lattice which is pulsed a small number of times, corresponding to the "weakly-diffracting limit". In Chapter 8 we describe our model system and its general time evolution. We then present a full analytic model for the time evolution of the atomic populations of the zeroth and first diffraction orders, which is sufficient for a "weak" lattice (Chapter 9), as well as numerical simulations incorporating higher momentum states at both large ($V>0.1E_{\mathrm{R}}$) and small lattice depths, which we compare for typical experimental values (Chapter 10). We also explore the role of finite-temperature effects in such experiments (Chapter 11).

---

we discuss in Chapter 10.

Chapter 8

Model system: BEC in an optical lattice

8.1 Alternating Hamiltonian evolutions

We consider a BEC with interatomic interactions neglected.[a] This can be achieved experimentally by exploiting an appropriate Feshbach resonance [46, 48, 49, 50], or by allowing the cloud to expand adiabatically [92]. Working in this regime means that we need only consider the single-particle dynamics of each atom in the gas. The laser is far off resonance such that the atom has no internal degrees of freedom [93], and we consider only the motion of the center of mass. We proceed in the same fashion as [3], and consider that the BEC is periodically perturbed by an off-resonant 1d optical lattice, alternated with a free evolution.

The center of mass dynamics of a single atom in this regime is alternatingly governed by the following Hamiltonians [3]:

$$\hat{H}_{\text{Latt}} = \frac{\hat{p}^2}{2M} - V\cos(K\hat{x}), \tag{8.1.1a}$$

$$\hat{H}_{\text{Free}} = \frac{\hat{p}^2}{2M}, \tag{8.1.1b}$$

where $\hat{p}$ is the 1d momentum operator in the x direction (see Fig 8.1), $\hat{x}$ is the associated

---

[a]The quantum degeneracy is not important in our analysis, as the requirement is simply for a very narrow initial momentum spread.
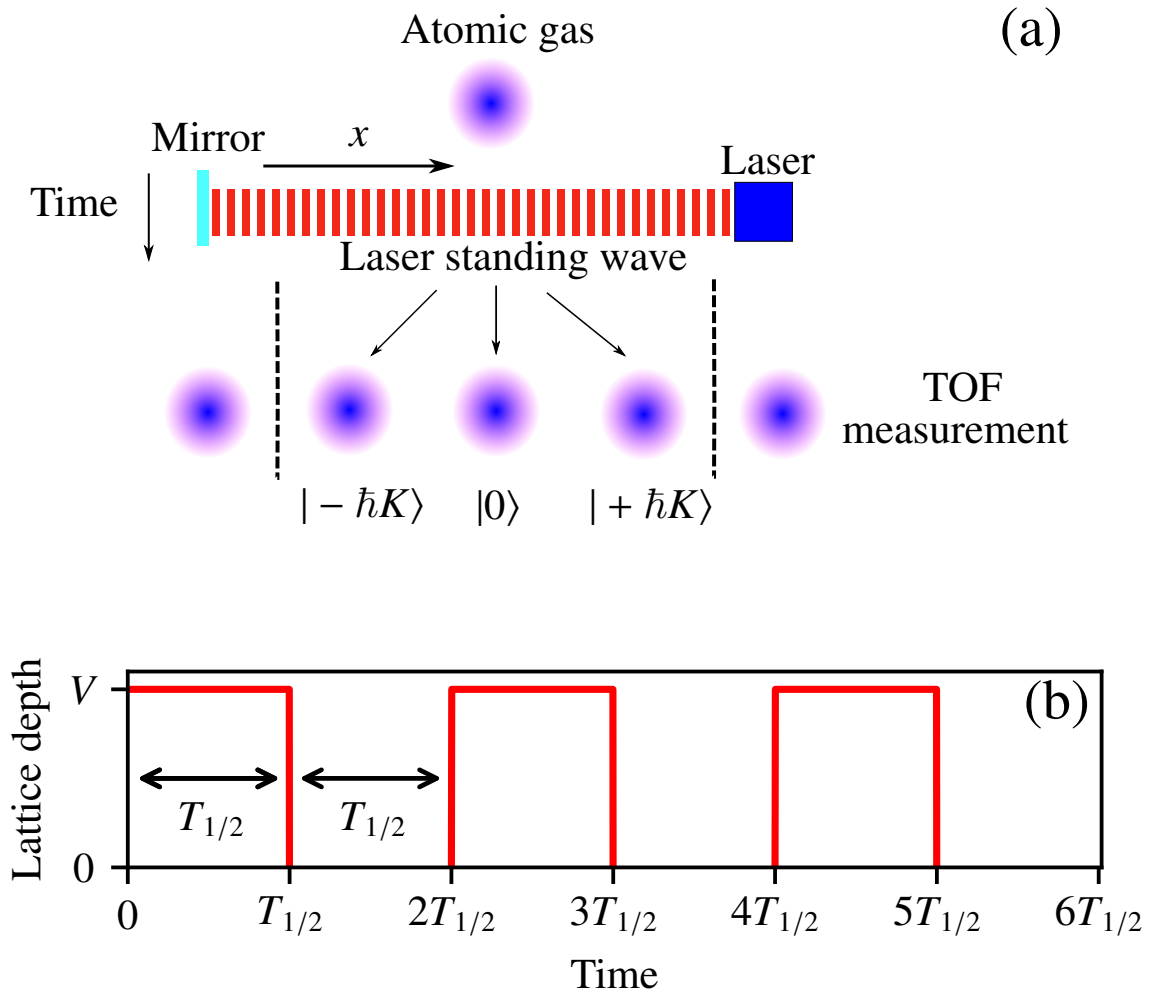
Figure 8.1: Diagram of a multi-pulse atom-diffraction setup. (a) shows a cold atomic gas subjected to multiple lattice pulse evolution sequences, before a time of flight beam measures the atomic population in each of the allowed momentum states, (b) shows the modulation of the lattice depth in time, where V is the lattice depth (dimensions of energy) when the standing wave pulse is on, and $T_{1/2}$ is the Talbot time as defined in Eq. (8.1.2). For simplicity, the laser standing wave has been oriented orthogonally to the gravitational direction, however we note that this is equivalent to a vertically oriented system in which a phase-shifter element is used to introduce a time dependent phase on the standing wave, which is tuned to cancel out gravity [1, 3].

position operator, M is the atomic mass, and V is the lattice depth,[b] with dimensions of energy, of a lattice with wavenumber K ($K = 2K_L$, here K_L is the laser wavenumber) [2, 52].

As stated in the introduction, Herold *et al.* and Kao *et al.* [30, 32] suggested that when measuring very small lattice depths ($V \sim 0.01E_R$, here $E_R = \hbar^2 K^2 / 8M$), the signal can be optimized by working in the regime where both the lattice pulse and free evolution have a duration equal to the half Talbot time [94],

$$T_{1/2} = \frac{2\pi M}{\hbar K^2}. \tag{8.1.2}$$

This is half the full Talbot time, where the Talbot time is the elapsed time for which the free evolution operator [generated by Eq. (8.1.1b)] collapses to the identity when applied to a momentum state that is an integer multiple of $\hbar K$.[c]

8.2   Time evolution

The periodicity in time of the system admits a Floquet treatment [51], where the time evolution of an initial state $|\psi(t = 0)\rangle$ for successive lattice-pulse sequences is given by the repeated action of the system Floquet operator $\hat{F}$ on the chosen initial state. This can be written as $|\psi(t = 2NT_{1/2})\rangle = \hat{F}^N |\psi(t = 0)\rangle$, where N is the number of pulse sequences.

The Floquet operator $\hat{F}$ governing a lattice pulse of duration $T_{1/2}$ [Eq. (8.1.2)], followed by a free evolution of the same duration, can be determined straightforwardly by constructing the time evolution operators associated with Eqs. (8.1.1a) and (8.1.1b). Further, the spatial periodicity of the laser standing wave enables us to invoke Bloch theory [54]. By recasting

---

[b]It is conventional to define the lattice depth with respect to a potential of the form $U_0 \sin^2(Kx/2)$, in this work we refer to the lattice depth as $V = -U_0/2 = -\hbar\Omega^2/8\Delta$ for a laser with Rabi frequency Ω and detuning $\Delta \equiv \omega_L - \omega_0$.

[c]For an initially zero-temperature gas, these conditions correspond to those for an antiresonance in the quantum δ-kicked particle, where the momentum width of the gas is bounded, and alternates between two values in time [2, 17, 21, 24, 25, 27, 28, 42, 51, 57, 60].

the momentum operator $\hat{p}$ in a basis such that:

$$(\hbar K)^{-1}\hat{p} = \hat{k} + \hat{\beta}, \tag{8.2.1a}$$

$$\hat{k}|(\hbar K)^{-1}p = k + \beta\rangle = k|(\hbar K)^{-1}p = k + \beta\rangle, \tag{8.2.1b}$$

$$\hat{\beta}|(\hbar K)^{-1}p = k + \beta\rangle = \beta|(\hbar K)^{-1}p = k + \beta\rangle, \tag{8.2.1c}$$

with $k \in \mathbb{Z}$ and $\beta \in [-1/2, 1/2)$ [55], we elucidate that the total dimensionless momentum $(\hbar K)^{-1}p$ associated with a single plane wave is the sum of k, the discrete part, and β as the continuous part or *quasimomentum*, which is a conserved quantity. In other words, only momentum states separated by integer multiples of $\hbar K$ are coupled [3, 16]. We may therefore say that the system Floquet operator in a single quasimomentum subspace can be written:

$$\hat{F}(\beta) = \hat{F}(\beta)_{\text{Free}}\hat{F}(\beta)_{\text{Latt}} = \exp\left(-i\left[\frac{\hat{k}^2 + 2\hat{k}\beta}{2}\right]2\pi\right) \times \exp\left(-i\left[\frac{\hat{k}^2 + 2\hat{k}\beta}{2} - V_{\text{eff}}\cos(\hat{\theta})\right]2\pi\right), \tag{8.2.2}$$

where $V_{\text{eff}} = VM/\hbar^2K^2$ is the dimensionless lattice depth, $\hat{\theta} = K\hat{x}$ and 2π is the rescaled half Talbot time.[d] By using Eq. (8.2.2) to calculate $|\psi(N)\rangle = \sum_j c_j(N)|k = j\rangle$, the population in each discrete momentum state $|k = j\rangle$ after N pulses is given by the absolute square of the individual coefficients $P_j(N) = |c_j(N)|^2$. In this paper we employ the well-known split-step Fourier approach [3, 33], as well as matrix diagonalization in a truncated basis [32, 95] to determine $|\psi(t = N)\rangle$ beyond the weakly-diffracting limit, as well as an analytic approach in the weakly-diffracting case.

---

[d]Generally speaking Eq. (8.2.2) should include the operator $\hat{\beta}$, however, because we restrict our analysis to initial states within a single quasimomentum subspace, β is simply a scalar value, and relative phases which depend solely on β can be neglected.

Chapter 9

Analytic results in a two-state basis

For an initially zero-temperature gas ($\beta = 0$) subjected to a small number of pulses from a shallow lattice, a useful approximation is to assume that no population is diffracted into momentum states with $|p| > \hbar K$, the so-called "weakly-diffracting limit". Mathematically, this regime corresponds to the time evolution of an initial state $|\psi(t = 0)\rangle = |k = 0\rangle$ in a space spanned only by the $|k = -1\rangle$, $|k = 0\rangle$ and $|k = 1\rangle$ states of the $\beta = 0$ quasimomentum subspace.

The symmetry of the lattice and free evolution Hamiltonians about $|k = 0\rangle$ guarantees that for our chosen initial state, the population diffracted into the $|k = 1\rangle$ state is identical to that diffracted into the $|k = -1\rangle$ state, as the amplitude associated with each state is the same. We take advantage of this by expressing the system Hamiltonians (8.1.1a), (8.1.1b) as matrices

in the truncated momentum basis:

$$|0\rangle = |k = 0\rangle = \begin{pmatrix} 0 \\ 1 \\ 0 \end{pmatrix}, \tag{9.0.1a}$$

$$|+\rangle = \frac{1}{\sqrt{2}}(|k = 1\rangle + |k = -1\rangle) = \begin{pmatrix} 1 \\ 0 \\ 0 \end{pmatrix}, \tag{9.0.1b}$$

$$|-\rangle = \frac{1}{\sqrt{2}}(|k = 1\rangle - |k = -1\rangle) = \begin{pmatrix} 0 \\ 0 \\ 1 \end{pmatrix}, \tag{9.0.1c}$$

yielding the following 3×3 matrix representation of the lattice Hamiltonian:

$$H_{\text{Decoupled}}^{3 \times 3} = \begin{pmatrix} 1/2 & -V_{\text{eff}}/\sqrt{2} & 0 \\ -V_{\text{eff}}/\sqrt{2} & 0 & 0 \\ 0 & 0 & 1/2 \end{pmatrix}. \tag{9.0.2}$$

There is no coupling between the $|0\rangle$ state, and the antisymmetric $|-\rangle$ state, implying that for an initially zero-temperature gas there is no population transfer into the $|-\rangle$ state for all time. The remnant basis is therefore only two-dimensional, with basis states: $|0\rangle_2 \equiv \begin{pmatrix} 0 \\ 1 \end{pmatrix}$ and $|+\rangle_2 \equiv \begin{pmatrix} 1 \\ 0 \end{pmatrix}$, which we may use to represent Equation (8.1.1a) as the 2×2 matrix:

$$H_{\text{Trunc}} = \begin{pmatrix} 1/2 & -V_{\text{eff}}/\sqrt{2} \\ -V_{\text{eff}}/\sqrt{2} & 0 \end{pmatrix}. \tag{9.0.3}$$

We recognize Eq. (9.0.3) as a Rabi matrix, the eigenvalues $E_\pm$ and normalized eigenvectors $\bar{E}_\pm$ of which are well known [96], and can be used to calculate the populations of the $|0\rangle$ and

$|+\rangle$ states [$P_0(N, V_{\text{eff}})$ and $P_+(N, V_{\text{eff}})$ respectively] after N pulses:

$$P_0(N, V_{\text{eff}}) = 1 - A \sin^2(N\phi/2), \tag{9.0.4a}$$

$$P_+(N, V_{\text{eff}}) = A \sin^2(N\phi/2), \tag{9.0.4b}$$

$$A = \frac{8V_{\text{eff}}^2 \sin^2\left(\pi \sqrt{1 + 8V_{\text{eff}}^2}/2\right)}{8V_{\text{eff}}^2 + \cos^2\left(\pi \sqrt{1 + 8V_{\text{eff}}^2}/2\right)}, \tag{9.0.4c}$$

$$\phi = 2 \arctan\left(\frac{\sqrt{8V_{\text{eff}}^2 + \cos^2\left(\pi \sqrt{1 + 8V_{\text{eff}}^2}/2\right)}}{\sin\left(\pi \sqrt{1 + 8V_{\text{eff}}^2}/2\right)}\right), \tag{9.0.4d}$$

which are explicitly derived in appendix A [34]. We can see from Eqs. (9.0.4a) and (9.0.4b) that in the weakly-diffracting limit, P_0 and P_+ take the form of a sinusoidal oscillation with the number of pulses, N, entirely characterized by an amplitude A and a "frequency" ϕ, both of which depend on the lattice depth V_{eff} as the only free parameter. We note the similarity to the result reported in [89] for single pulse diffraction. The variation of A and of ϕ versus V_{eff} is displayed in Fig. 9.1.[a]

ϕ initially increases approximately linearly with V_{eff}, meaning that over a sufficiently small range of lattice depths, we should expect to see an approximate universality in the population dynamics when the time axis is scaled by V_{eff}. This scaling is explored in Chapter 10. The exact form of ϕ in the limit where $V_{\text{eff}} \to 0$ is $\phi = 4\sqrt{2}V_{\text{eff}}$ (see Appendix B), which corresponds to the straight line plotted in Fig. 9.1(a). Further, if we substitute this result into Eq. (9.0.4b) and expand it as a Taylor series to leading order, we recover the familiar quadratic dependence of P_+ on N of Herold et al. [30, 32] (see Appendix B.3):

$$P_+ = 8N^2 V_{\text{eff}}^2 \propto N^2. \tag{9.0.5}$$

This result is valid subject to the condition $N\phi(V_{\text{eff}})/2 \ll 1$. As V_{eff} is increased beyond this regime, A, which decreases steadily in the range of linearity of ϕ, reaches its first node at $V_{\text{eff}} = \sqrt{3}/(2\sqrt{2}) \simeq 0.612$, and afterward at all points where $V_{\text{eff}} = \sqrt{4m^2 - 1}/(2\sqrt{2})$,

---

[a]Note that when explicitly evaluating Eq. (9.0.4d), it is desirable to use the "atan2" numerical routine e.g. in Python; this ensures that the sign of the argument is taken into account, which avoids singularities in the frequency.
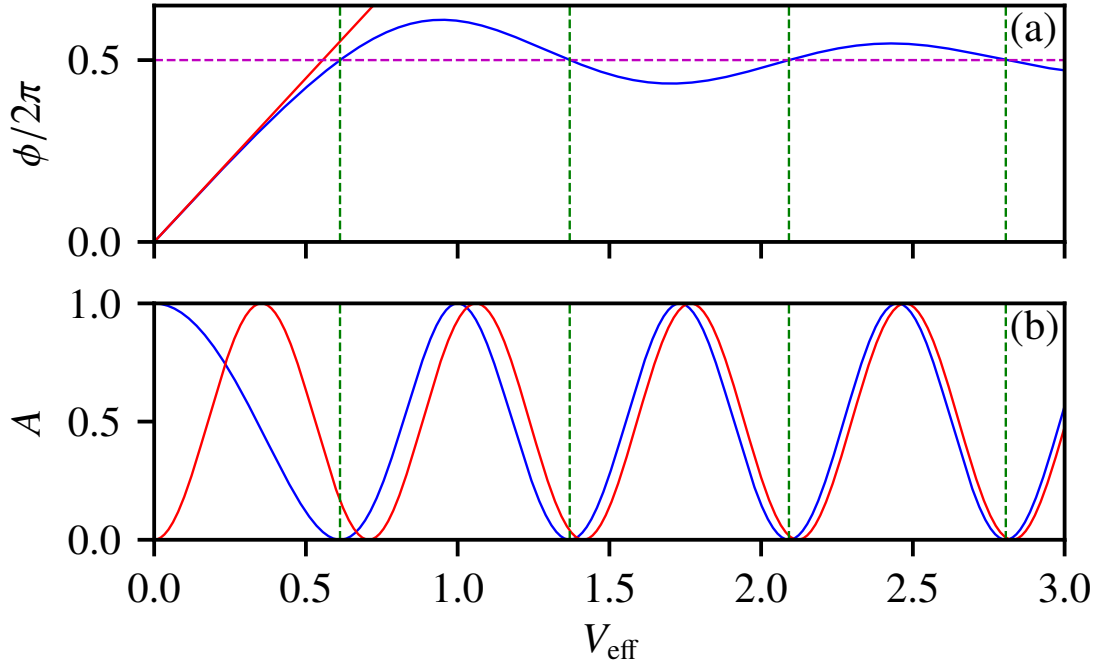
Figure 9.1: Plot of the variation of $\phi/2\pi$, (a), and the amplitude A, (b), versus V_{eff}, all quantities are dimensionless. The blue curves [beginning at $\phi/2\pi = 0$ for (a), and $A = 1$ for (b)] give the full analytic form for each expression, corresponding to Eqs. (9.0.4d) and (9.0.4c) respectively. The solid red lines show our linear approximation to ϕ for $V_{\text{eff}} \ll 1$, $\phi \approx 4\sqrt{2}V_{\text{eff}}$ [the straight line of (a)], and our limiting value of A for $V_{\text{eff}} \to \infty$, $A = \sin^2(\sqrt{2}\pi V_{\text{eff}})$ [the lowermost curve of (b)]. The horizontal dashed line in (a) appears at $\phi = \pi$, which is a physically relevant value about which ϕ oscillates beyond its first turning point. The vertical lines correspond to the points where $\phi = \pi$, and $A = 0$, both of which always occur simultaneously.

$m \in \mathbb{Z}^+$, which are denoted by the vertical dashed lines of Fig 9.1. Physically, these values of V_{eff} correspond to a situation in which there is no pulse-to-pulse population transfer out of the $|k = 0\rangle$ state, at least in the weakly-diffracting limit. It can be shown analytically (see Appendix B), that $\phi = \pi$ at those values of V_{eff} where A has a node, shown by the intersection of the vertical and horizontal dashed lines of Fig 9.1(a).

In the limit as $V_{\text{eff}} \to \infty$, $\phi = \pi$ wherever $V_{\text{eff}} = n/\sqrt{2}$, with an overall oscillatory behavior of ever-decreasing amplitude around this value, while A takes on the form of a sinusoidal oscillation $A = \sin^2(\sqrt{2}\pi V_{\text{eff}})$.

Chapter 10

Incorporating higher diffraction orders

10.1 Numerical simulations for a large momentum basis

Having obtained analytic results for the time-evolved populations in the weakly-diffracting limit, we may test their domain of validity by using standard numerical techniques to compute the full momentum distribution of the system, and sampling the population in the $|k = 0\rangle$ state, P_0. We follow the same approach as [33, 51] and work within the momentum basis. The action of the Floquet operator (8.2.2) on the total state of the system, $|\psi\rangle$, is calculated by a split-step Fourier method, on a basis of 2048 momentum states, which is exhaustive for any practical purpose.

The analytic results of Eqs. (9.0.4a,9.0.4b,9.0.4c,9.0.4d) are compared to this exact numerical calculation in Fig. 10.1 for fixed values of V_{eff} (see caption for details). From Fig. 10.1(a) we can clearly see that for higher values of the effective lattice depth, the sinusoidal character of the analytic result for P_0 is revealed, as well as a similar oscillatory behavior in the full numerics. Naively, we may say that increasing V_{eff} gives rise to a greater deviation of the full numerics from the analytics. While this is true when comparing over a fixed number of pulses, we may use our argument in Chapter 9, that there is an approximate universality in V_{eff} and the number of pulses, to clarify this statement by means of the universal curve displayed in Fig. 10.1(b).
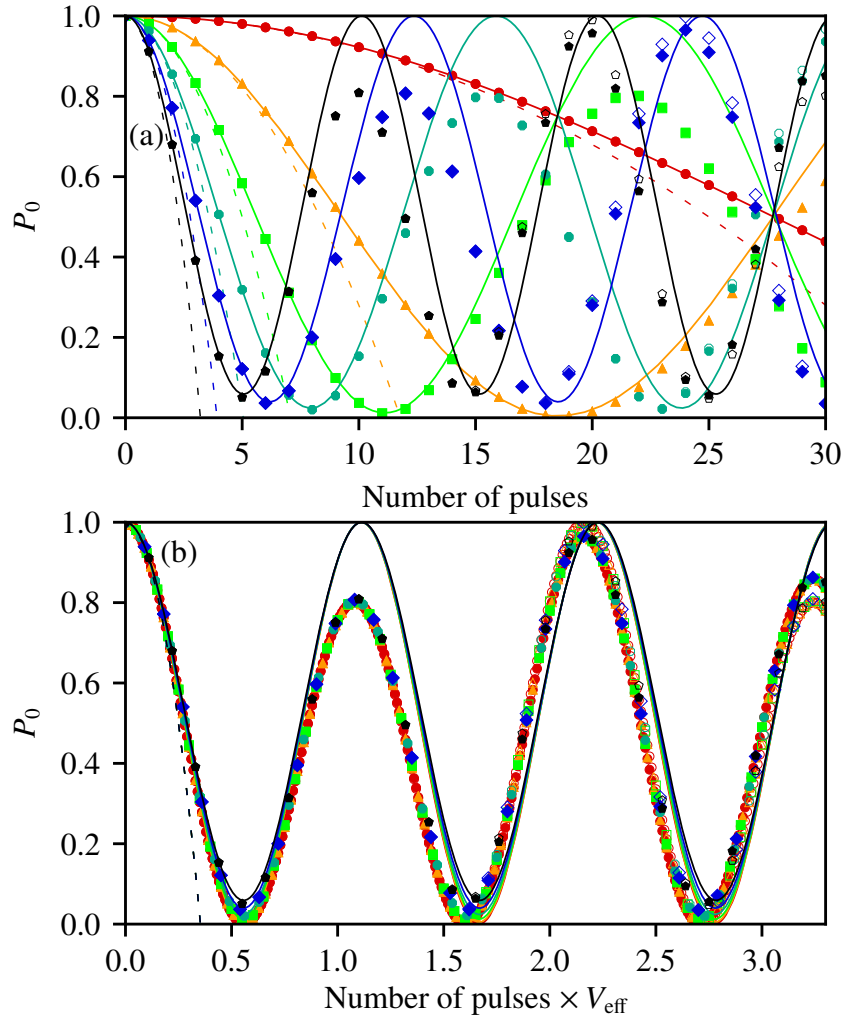
Figure 10.1: (a): Plot of population in the $|k = 0\rangle$ state, P_0, versus number of pulses, as calculated in a truncated momentum basis with $|k| \leq 3$ by numerical diagonalization (hollow markers), and full numerics (Fourier split-step calculation using 2048 basis states) (solid markers). The solid lines correspond to the analytic solution for P_0 in a two state basis, as given by Eq. (9.0.4a), while the dashed lines represent the quadratic solution of Herold et al. [Eq. (9.0.5)]. Each set of markers corresponds to a fixed value of the effective lattice depth ranging from the slowest-oscillating curve at $V_{\mathrm{eff}} = 0.01$ (red circles) to the fastest oscillating one at $V_{\mathrm{eff}} = 0.11$ (black pentagons) in steps of 0.02. (b): Reproduction of (a), with the number of pulses axis scaled by the dimensionless lattice depth V_{eff} to reveal an approximate universal curve both in the analytics and the numerical simulations. The data have been extended to span the full range of the horizontal axis. The universal curve reveals a drop in the amplitude of P_0 as calculated by the full numerics at the first revival, which is not reproduced by the analytics, but is reproduced in the truncated momentum basis. In (b), the oscillation frequency of the numerical curve increases compared to that of the analytic result as the number of pulses or the lattice depth is increased. After three half-oscillations on the universal curve, the truncated basis result begins to deviate appreciably from the full numerics.

Figure 10.1(b) clearly shows that the universality holds approximately for the full numerics also, and that the analytics cease to agree with the full numerics at approximately the same point on the universal curve, regardless of the value of V_{eff} in the chosen range. We may therefore modify our previous statement on the range of validity of the analytics, and say instead that the analytics are sufficient to understand the system provided the product of the number of pulses and effective lattice depth is sufficiently small. We note specifically that there is a frequency drift which increases along the curve, and a marked reduction in amplitude of the full numerics as compared to the analytics at the first revival of the curve. Both features appear due to leakage of population into momentum states with $|p| > \hbar K$, and inform our discussion of the range of validity of the weakly-diffracting limit taken in previous work. Indeed, the quadratic result of Herold et al. [Eq. (9.0.5)] deviates from the full numerics at a much smaller value of NV_{eff} than our exact analytic result for two diffraction orders.

In [30, 32], the regime in which the weakly-diffracting limit is satisfied is given as an inequality, $NV_{\text{eff}} \ll 1/4$, when recast in our system of variables. Though this inequality places an upper bound on the allowed value of NV_{eff}, it is reasonable to ask the question: "at what point is NV_{eff} sufficiently small to be considered much smaller than 1/4?" We may answer this question by reinterpreting the inequality using our universal curve, for which NV_{eff} is the dependent variable.

By inspection of Fig. 10.1(b), we can see that at $NV_{\text{eff}} = 1/4$, there is still excellent agreement between our analytics and full numerics. To refine this statement, we calculate the RMS difference between our analytics and full numerics [97] at this point over the range of chosen lattice depths (defined as RMS=$[\sum_{j=1}^{\mathcal{N}}\{P_0(N, V_{\text{eff}})_j - P_{0(\text{Numerical})}(N, V_{\text{eff}})_j\}/\mathcal{N}]^{1/2}$, where $\mathcal{N}$ is the number of lattice depth values) as 0.0011 (deviation at the 0.1% level), meanwhile the quadratic result deviates at the 42% level.[a] The point at which leakage into higher momentum-states first becomes appreciable is $NV_{\text{eff}} \sim 1/2$, with an RMS of 0.0043 (deviation at the 0.4% level). Though this is clearly sufficiently small to still be considered within the range of validity of the weakly-diffracting limit, beyond $NV_{\text{eff}} \sim 1/2$, where the RMS becomes larger, we must incorporate higher momentum-states in order to have a valid

---

[a]In practice, the discretization of the time axis in the number of pulses means that we cannot generally assume that any data points from the full numerics will fall at the exact value $NV_{\text{eff}} = 1/4$, and so we have chosen the data closest to this point in our calculation of the RMS.
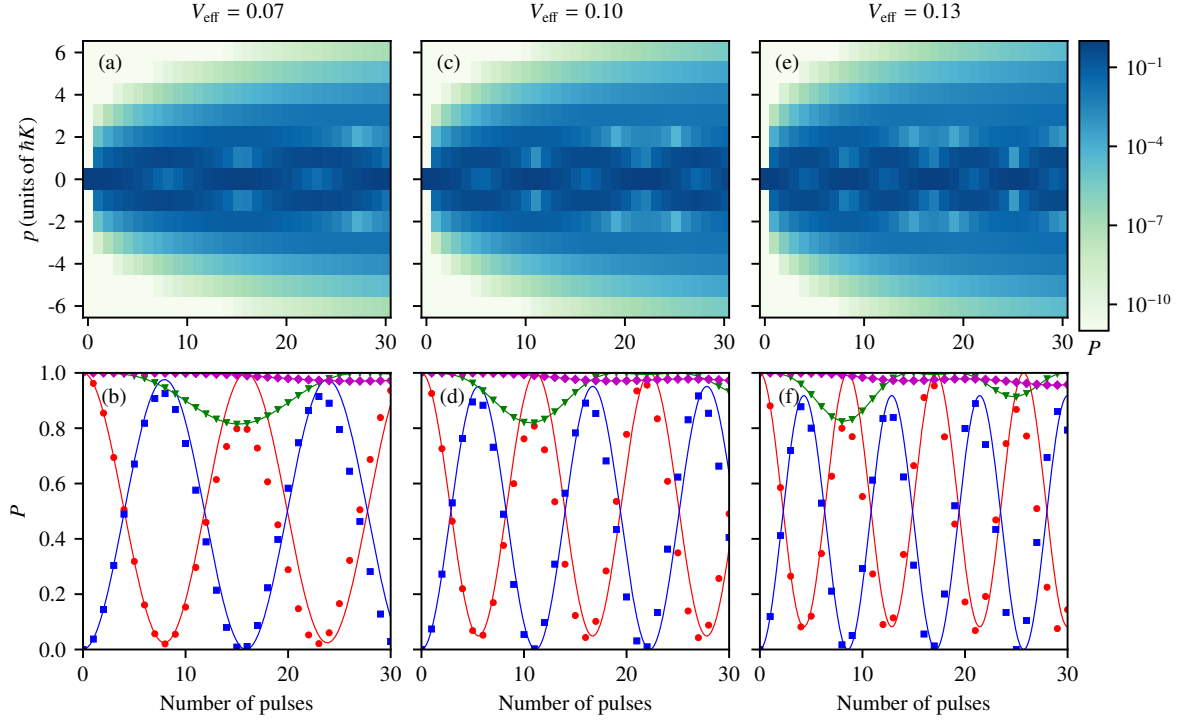
Figure 10.2: Comparison between population dynamics for differing values of the dimensionless lattice depth V_{eff}, as computed by full numerics and the two-state analytic model of Eqs. (9.0.4a) and (9.0.4b). Row 1 [(a), (c), (e)] comprises momentum distributions versus the number of lattice pulses for an initially zero-temperature gas in a basis of 2048 momentum states. Each false-color plot shows the time evolved population in the first 13 momentum states ($|k| < 6$), to be read on the colorbar to the right. A cutoff population value of $P_{\text{cutoff}} = 10^{-11}$ has been applied to each population distribution to accommodate the log scale. This illustrates that for this choice of parameters, the amount of population diffracted into momentum states with $|p| > 3\hbar K$ is negligible. Row 2 [(b), (d), (f)] shows firstly, slices through the momentum distribution corresponding to the population in the $k = 0$ state, P_0, (red circles) and the $|p| = \hbar K$ states, $P_{\pm 1}$, (blue squares), to which our two-state analytic model is compared (red and blue solid lines respectively). To clarify the drop in amplitude in the first revival of P_0, the green triangles have been added, which correspond to $1 - P_{\pm 2}$ and almost intersect the red circles corresponding to P_0, indicating that the overwhelming majority of the population which has left P_0 at this point, has in fact been diffracted into the $|k| = 2$ states. At the second revival, the two sets of points are further apart. Population leakage into the $|p| = 3\hbar K$ states, corresponding to the magenta diamonds, which represent $1 - P_{\pm 3}$, explains this effect. Solid lines have been added as a guide to the eye. Each column corresponds to a fixed value of V_{eff}, [(a),(b)] $V_{\text{eff}} = 0.07$, [(c),(d)] $V_{\text{eff}} = 0.10$, [(c),(d)] $V_{\text{eff}} = 0.13$.

model. This motivates the question of how many momentum states are necessary to include for such a model to be useful for a reasonable choice of experimental parameters.

Figures 10.2 (a,c,e) show a selection of momentum distributions for a range of values of V_{eff} as calculated by the full numerics, showing momentum states up to $|p| \leq 6\hbar K$, with Figs. 10.2 (b,d,f) showing corresponding slices through the momentum distributions. The log scale makes clear that there is very little population leakage into momentum states with $|p| > 3\hbar K$ for the chosen values. Instead we see that there are pronounced oscillations in population between the $|p| = 0$ and $|p| = \hbar K$ states, which are modulated by population leakage into the $|p| = 2\hbar K$ states, and to a lesser extent the $|p| = 3\hbar K$ states. By inspection of the lattice Hamiltonian in the momentum basis, this can be explained by the decrease in magnitude of the off-diagonal coupling terms with state number. In fact, the decrease in amplitude at the first revival in Fig. 10.1(b) is almost entirely due to population leakage into the $|p| = 2\hbar K$ states, suggesting that a model incorporating only $n = 5$ momentum states should be sufficient to capture the dynamics, up to at least $V_{\text{eff}} = 1.1$. We investigate this model in the following section.

10.2   Small momentum bases of dimension > 2

To incorporate higher momentum-states we numerically diagonalize Eqs. (8.1.1a) and (8.1.1b), in a truncated basis of n momentum states, and propagate the time-evolution using the procedure described in Appendix B.4. Our previous analysis suggests that simulations using a basis of $n = 5$ momentum states ought to be sufficient for practical purposes, the results of which are given by the hollow markers in Fig. 10.1(b). The five state model is an order of magnitude more accurate than the analytics at $NV_{\text{eff}} = 1/4$ and $NV_{\text{eff}} = 1/2$, with RMS differences with respect to the full numerics of 0.00018, and 0.00011 respectively. As expected, the decrease in amplitude at the second revival on the universal curve is reproduced by this approach, but is clearly also valid over a larger range, up to the fourth turning point ($NV_{\text{eff}} \sim 1.6$, RMS deviation 0.0022), beyond which the model begins to overestimate and then underestimate the exact numerical result.

This difference appears as a result of the basis truncation, as population leakage into states

with $|p| \geq 5\hbar K$ is explicitly not possible in this model, though it should be noted that this effect would only be relevant to experiments performed using a very large effective lattice depth. An attractive feature of the five state model is that it can in principle be solved analytically for the time-evolution of the populations, which can be fit to experimental data to extract more accurate lattice depths.

Chapter 11

Finite-temperature response

The results presented in the previous sections are valid for a gas which is assumed to be initially at zero temperature; in practice this regime is never fully achieved, even for a BEC. In this section we consider the role of finite-temperature effects. To find the response of P_0 versus the number of pulses for a finite-temperature gas, we calculate the time evolution of P_0 for an ensemble of initial momentum states $|\psi(t = 0)\rangle = |(\hbar K)^{-1}p = k + \beta\rangle$ according to Eq. (8.2.2), where the initial momentum is defined in a Bloch framework with k and β as free parameters. For a sufficiently cold gas [temperature $\mathcal{T}_w \lesssim (\hbar^2 K^2/64Mk_{\mathrm{B}})$][a] we need only consider initial states with $k = 0$ in order to capture the essential features. In this regime we choose a fixed value of the lattice depth and scan across the full range of the quasimomentum, β, as the only free parameter, to find the momentum dependence in the first Brillouin zone [54] displayed in Fig. 11.1.

Figure 11.1 clearly shows the central resonance at $\beta = 0$, where our zero-temperature analysis has been concentrated. Increasing the quasimomentum to $|\beta| = 0.0625$, we can see that the oscillation in P_0 has an amplitude of less than 50% of that at $\beta = 0$, and a substantially different frequency. Hence, the width of the central resonance is relatively narrow compared to the full width of the Brillouin zone. For an initial momentum distribution of appreciable width we must consider the surrounding structure when calculating the population dynam-

---

[a]This rule of thumb is chosen such that the initial width of the momentum distribution is at most one quarter that of the first Brillouin zone.
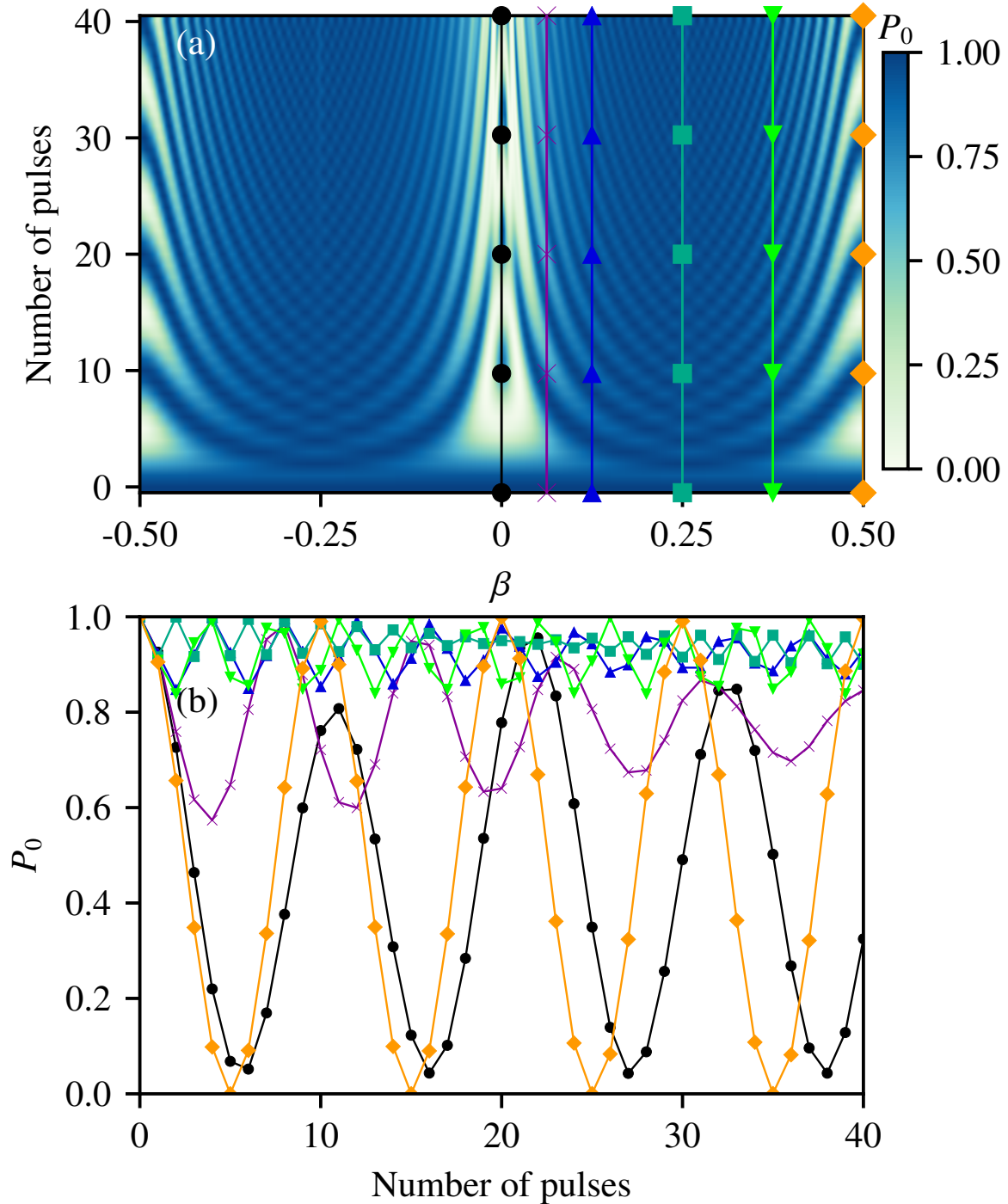
Figure 11.1: (a) False-color plot of the time evolution of P_0 as computed in a basis of 2048 momentum states for values of the dimensionless quasimomentum β [see Eq. (8.2.1)] ranging from $\beta = -0.5$ to $\beta = 0.5$ in steps of $\beta = 0.00025$ (4001 quasimomentum values). We have chosen a relatively large lattice depth of $V_{\text{eff}} = 0.1$ such that the different dynamical behaviors are made clear for the chosen number of pulses $N = 40$. (b) Slices taken through the quasimomentum distribution parallel to the time axis for $\beta = 0, 0.0625, 0.125$, then increasing in increments of $\beta = 0.125$ up to a maximum of $\beta = 0.5$, enclosing the full range of dynamics in the $k = 0$ subspace. Each vertical set of markers in (a) corresponds to the position in the quasimomentum distribution of the slices in (b), where the solid lines have been added as a guide to the eye.
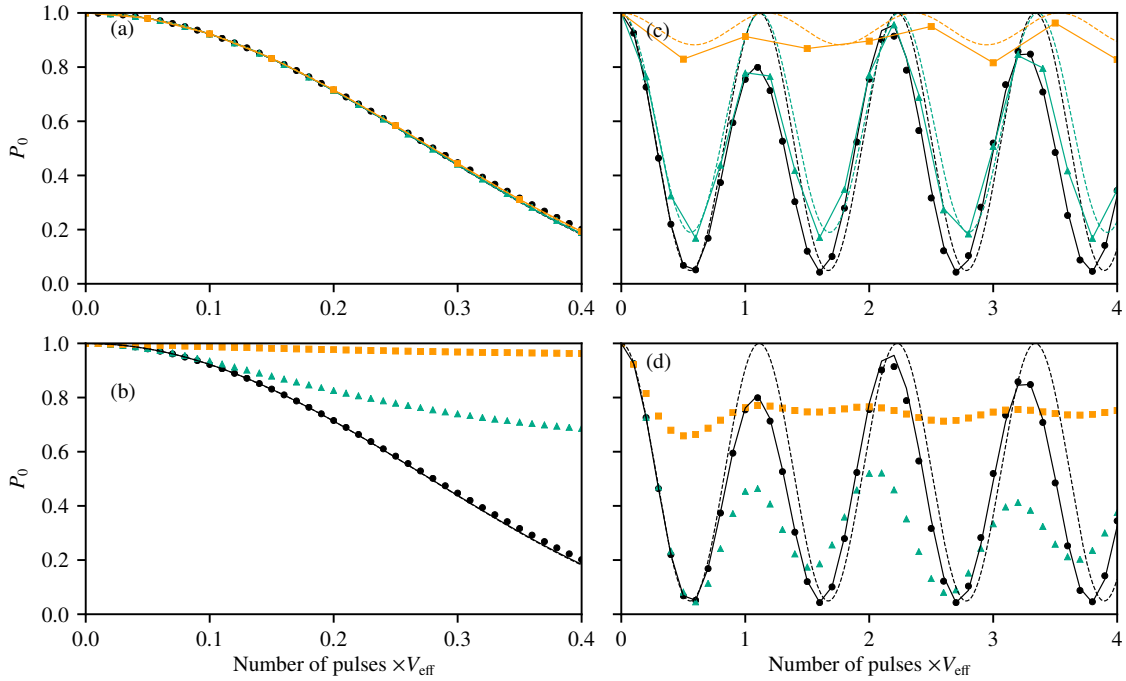
Figure 11.2: Plot of the finite temperature response of P_0 vs (number of pulses)$\times V_{\text{eff}}$, where V_{eff} is the dimensionless lattice depth [see Eq. (8.2.2)], as calculated for an ensemble of 4001 particles each evolved in a basis of 2048 momentum states. The left column [(a), (b)] corresponds to the weak-lattice regime, and the right column [(c), (d)] to the strong-lattice regime. The top row of plots [(a), (c)] shows the finite-temperature response of P_0 at a temperature of $w = 0.00125$ for a selection of different lattice depths, $V_{\text{eff}} = 0.01, 0.02, 0.05$ (all curves fall on top of each other) in the weak regime (a) and $V_{\text{eff}} = 0.1, 0.2, 0.5$ (lower, middle and uppermost curves) in the strong regime (b). For the bottom row [(b), (d)], each set of curves and markers corresponds to the response of P_0 at a different temperature ($w = 0.00125, 0.0125, 0.125$; lower, middle and uppermost curves respectively), where the effective lattice depth is kept constant at $V_{\text{eff}} = 0.1$ in the strong-lattice case and $V_{\text{eff}} = 0.01$ the weak-lattice case. In all panels, the solid lines correspond to the exact numerical result for a given lattice depth at zero temperature, while the dashed lines represent the corresponding analytic result at zero temperature in a basis of three momentum states [Eq. (9.0.4a)]. The dashed lines in panels (a) and (b) are difficult to resolve, as they match up with the full numerical zero-temperature result almost exactly.

ics, as the zero-temperature behavior will be washed out over time, or even be unresolvable altogether if the temperature is sufficiently high.

Note that for broader initial momentum distributions, the dynamics will include the secondary resonances at $|\beta| = 0.5$, which have a periodicity of the form $P_0(N) = \cos^2(\pi V_{\mathrm{eff}} N)$, such that P_0 varies between 0 and 1 for all V_{eff}.

Having characterized the first Brillouin zone, we calculate the full finite-temperature response of P_0 by performing Gaussian weighting in the momentum space according to a rescaled Maxwell-Boltzmann distribution:

$$D_{k=0}(\beta) = \frac{1}{w\sqrt{2\pi}} \exp\left(\frac{-\beta^2}{2w^2}\right), \qquad (11.0.1)$$

where the dimensionful temperature is given by $\mathcal{T}_w = \hbar^2 K^2 w^2 / M k_{\mathrm{B}}$ [51].

Figure 11.2 shows the variation of P_0 with the number of pulses, including regimes of both the strong and weak lattice regimes, and three different values of the initial momentum distribution width w. In overview: in regimes where we have a weak lattice and low temperature the analytic formula is adhered to almost perfectly; in regimes where we have a weak lattice and a higher temperature, we begin to see noticeable deviations which occur for a smaller number of pulses as the temperature is increased; where we have a strong lattice and low temperature, although the analytic formula is not strongly adhered to as the lattice depth increases, the oscillation frequency appears to be reasonably robust as V_{eff} increases and the amplitude of oscillation consequently decreases; finally for a strong lattice and higher temperature, the analytic formula is again only adhered to for relatively short times, with that time being dependent on the temperature.

Chapter Summary

- We have a zero-temperature analytic formula which yields significant insight assuming that we are working in the weakly-diffracting limit, and has a vastly larger domain of validity than the state of the art. In view of this, we argue that fitting this improved formula to experimental results ought to yield more accurate values of the lattice depths associated with weak atomic transitions, where the lattice depth is correspondingly small.

- We have shown that at zero temperature, very small basis sizes are sufficient to capture the essential features of the population dynamics outside the weakly-diffracting limit, and investigated how leakage of population into higher order momentum states affects the dynamics of the population in the zeroth order momentum state. From this analysis we have more rigorously constrained the domain of validity of the weakly diffracting limit compared to previous work.

- We have explored the effects of finite temperature initial distributions, and elucidated regimes from which the lattice depths can be determined from the observed dynamics in the lowest diffraction order. In particular we have shown that in regimes of weak lattice and low temperature, which are those most relevant to the determination of weak atomic transitions, our zero-temperature analytic formula is sufficient to capture the dynamics of the zeroth order momentum state population. For strong lattices in both low and high temperature regimes, the analytic formula still gives a reasonable estimate of the oscillation frequency over a range of lattice depths.

Part III

Lattice depth characterisation using continuous grating atom diffraction

Chapter 12

Introduction

In the previous Part we have presented improved models for the multipulse optical lattice [4] depth measurement scheme of [30, 32]. These models are useful for accurate determination of transition matrix elements of weak atomic transitions [76, 77, 78, 79, 80], where the corresponding lattice depths are small ($V \lesssim 0.01 E_R$ for any atom, where V is the lattice depth and E_R is the atomic recoil energy), and other available methods based on Kapitza–Dirac scattering [75, 86, 87, 88, 89], parametric heating [83], and sudden phase shifts [85] may suffer from signal-to-noise problems in the measurement of the resultant diffraction patterns.

Better knowledge of these matrix elements can be used to improve the black body radiation correction for ultraprecise atomic clocks [81, 82], and allows quantitative modeling of atom-light interaction [98]. In our analysis of the multipulse approach, we noted that when considering a gas with initial momentum $\hbar K/2$, the functional form of the time evolution of the atomic populations in the zeroth diffraction order is markedly simpler and therefore easier to fit to data to make an accurate measurement of the lattice depth [34].

In this Part of the thesis we explore a measurement scheme based on a regime of very simple, analytically tractable dynamics that we believe would be useful for determining optical lattice depths. Like [84], it also considers Rabi oscillations between different Bloch bands. The crucial difference is that the chosen regime accesses simple resonant behavior. We consider a lattice which is continuously present throughout the experimental sequence, which we show to be more robust to finite-temperature effects than a multipulse approach considered in [32]

for the determination of matrix elements. In Chapter 13, we describe our model system and experimental considerations. In Chapter 14, we introduce a simplified analytic approach for determining the time evolution of the atomic population in the zeroth diffraction order, and make a comparison to exact numerical calculations. Finally, in Chapter 15, we present an approximate analytic model for the finite-temperature response of the system, and discuss how these may be used to determine both the lattice depth and initial temperature of the atomic gas.

Chapter 13

Model system: Atomic gas in an optical grating

13.1 Experimental setup and Hamiltonian

We consider a two-level atom in an assumed noninteracting Bose-Einstein condensate exposed to a far off resonance optical grating, the Hamiltonian of which is given:

$$\tilde{H}_{\text{Latt}} = \frac{\hat{p}^2}{2M} - V \cos\left(K\left[\hat{x} + v_\phi t\right]\right),^{\text{a}} \qquad (13.1.1)$$

where $\hat{p}$ is the momentum operator along the lattice axis, V is the lattice depth, K is twice the laser wavenumber k_{L}, M is the atomic mass and v_ϕ is the phase velocity of the grating in the x direction (v_ϕ=0 for a static grating). For the simpler case of a static grating, we consider a BEC initially prepared in a momentum state with $p = \hbar K/2$.[b] As shown in Fig. 13.1(a), the BEC is diffracted by the static optical grating for a time t, before a time of flight measurement interrogates the population of the gas in each of the allowed momentum states. In principle there is an infinite ladder of such states, each separated by integer multiples of $\hbar K$ [3, 16], though here we show only the zeroth and first diffraction orders. We note that an initial state

---

[a]Here $\tilde{H}_{\text{Latt}}$ refers to the untransformed Hamiltonian of the system in the lab frame.

[b]The initial momentum $p = \hbar K/2$ is chosen with a view to creating population oscillations between the zeroth and first diffraction orders with a strong sinusoidal character, as suggested in [34].
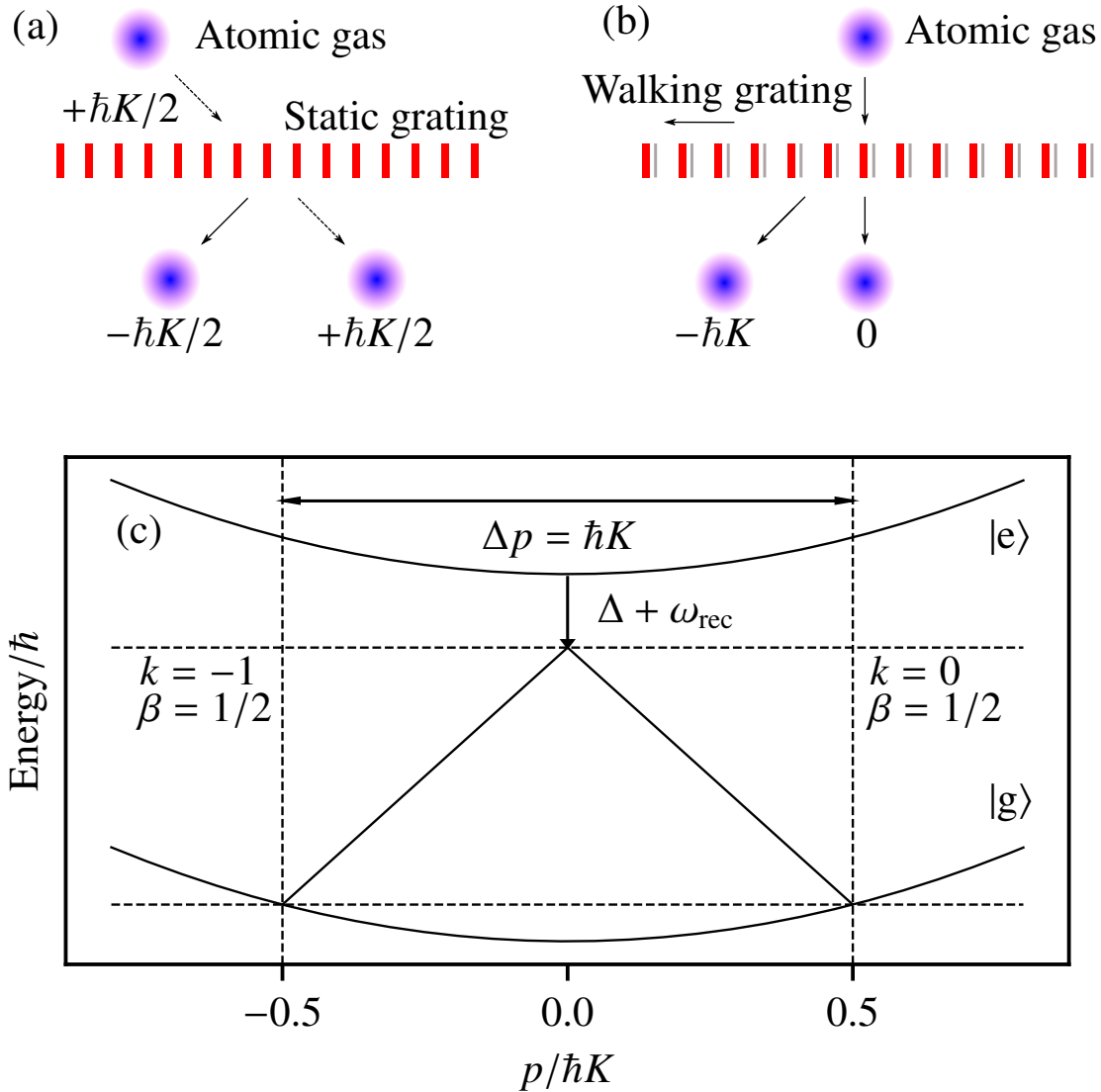
Figure 13.1: (a) A BEC initially prepared in the $p = +\hbar K/2$ state, where K is twice the laser wavenumber k_L, is exposed to a static optical grating, causing it to diffract into an, in principle, infinite number of momentum states separated by integer multiples of $\hbar K$; here we show only the first diffraction order. Equivalently, the BEC may be prepared in the $p = 0$ state, and exposed to a walking grating with an linearly time-dependent phase [see Eq. (13.1.1)] as in (b). The dynamics of the setup is identical, though the momenta in the lab frame are shifted by $-\hbar K/2$. (c), semiclassical energy-momentum diagram for a single two-level atom scattering photons from a static optical grating. The atom begins on the ground state energy parabola, with classical momentum $p = \hbar K/2$ before scattering a photon carrying momentum $p = -\hbar K/2$ and energy $\hbar^2 K^2/2M$, to reach the detuned virtual state above, before undergoing stimulated emission back to the ground state, resulting in a total momentum transfer of $\Delta p = -\hbar K$. This scattering process and its exact reversal are the only processes which semiclassically conserve both the energy and momentum of the atom grating system, indicating that population transfer between the $p = \hbar K/2$ and $p = -\hbar K/2$ states and vice versa ought to be the dominant process in the system.

$p = \hbar K/2$ can be achieved for instance by Bragg diffraction, or equivalently we may prepare the BEC in a state with $p = 0$ and impart an appropriately tuned time-dependent phase $v_\phi t$ to the standing wave as in Fig. 13.1(b). We show this equivalency in Sec. 13.2 below.

13.2 Gauge transformations and momentum kicks

The Hamiltonian of Eq. (13.1.1) can be transformed to a frame comoving with the walking grating by use of the unitary transformation

$$\hat{U} = \hat{U}_x \hat{U}_p \hat{U}_\alpha = \exp\left(imv_\phi \hat{x}/\hbar\right) \exp\left(-iv_\phi \hat{p}t/\hbar\right) \exp\left(i\alpha t/\hbar\right), \tag{13.2.1}$$

where we have chosen $\alpha = Mv_\phi^2/2$ for convenience.[c] Using $\hat{U}_p \hat{x} \hat{U}_p^\dagger = \hat{x} - v_\phi t$ and $\hat{U}_x \hat{p} \hat{U}_x^\dagger = \hat{p} - Mv_\phi$. This transformation yields:

$$\hat{H}_{\text{Latt}} = \frac{\hat{p}^2}{2M} - V\cos\left(K\hat{x}\right).^{\text{d}} \tag{13.2.2}$$

The Hamiltonian of Eq. (13.2.2) describes the system in a frame moving with velocity $-v_\phi$, therefore, a gas moving with velocity $v = 0$ in the moving frame appears to move with velocity $-v_\phi$ in the lab frame. Conversely, a gas moving with velocity $v = \hbar K/2M$ in the comoving frame, moves with velocity $v = (\hbar K/2M) - v_\phi$ in the lab frame. Choosing $v_\phi = 0$ yields the case in Fig. 13.1(a), while with $v_\phi = \hbar K/2M$, we have the situation shown in Fig. 13.1(b).

The spatial periodicity of Eq. (13.2.2) allows us to invoke Bloch theory [54], by rewriting the momentum operator in the following basis:

$$(\hbar K)^{-1}\hat{p} = \hat{k} + \hat{\beta}, \tag{13.2.3a}$$

$$\hat{k}|(\hbar K)^{-1}p = k + \beta\rangle = k|(\hbar K)^{-1}p = k + \beta\rangle, \tag{13.2.3b}$$

$$\hat{\beta}|(\hbar K)^{-1}p = k + \beta\rangle = \beta|(\hbar K)^{-1}p = k + \beta\rangle. \tag{13.2.3c}$$

---

[c]This choice of α ensures that the corresponding constant of $Mv_\phi^2/2$ appearing when Eq. (13.1.1) is transformed by the unitary operator $\hat{U}_x$ is canceled out, and so does not appear in Eq. (13.2.2).

[d]Here $\hat{H}_{\text{Latt}}$ refers to the transformed Hamiltonian in the frame comoving with the laser lattice, $\hat{x}$ and $\hat{p}$ still refer to the lab frame position and momentum.

We may speak of $k \in \mathbb{Z}$ as the discrete part of the momentum, and $\beta \in (-1/2, 1/2]$ as the continuous part or *quasimomentum* [55]. Here β is a conserved quantity, as such, only momentum states separated by integer multiples of $\hbar K$ are coupled [3, 16]. This simplification allows us to construct the time evolution operator for a lattice pulse of duration t from the lattice Hamiltonian (13.2.2) as follows:

$$\hat{U}(\beta, \tau)_{\text{Latt}} = \exp\left(-i\left[\frac{\hat{k}^2 + 2\hat{k}\beta}{2} - V_{\text{eff}}\cos(\hat{\theta})\right]\tau\right), \tag{13.2.4}$$

in which β is simply a scalar value such that overall phases which depend solely on β can be neglected. Here $V_{\text{eff}} = VM/\hbar^2 K^2$ is the dimensionless lattice depth, $\hat{\theta} = K\hat{x}$ and $\tau = t\hbar K^2/M$ is the rescaled time.

By using Eq. (13.2.4) to calculate $|\psi(\tau)\rangle = \sum_j c_j(\tau)|k = j\rangle$, the population in each discrete momentum state $|k = j\rangle$ following an evolution for a rescaled time of τ is given by the absolute square of the coefficients $P_j(\tau) = |c_j(\tau)|^2$. In this paper we employ the well-known split-step Fourier approach [3, 33] to determine $|\psi(\tau)\rangle$, as well as an analytic approach based on a simpler two-state model.

The dynamics of a single atom in the BEC standing-wave system can be understood in terms of the scattering process given by the semiclassical energy diagram of Fig. 13.1(c) (see also [99, 100, 101, 102, 103]). A two-level atom begins in a state with momentum $p = \hbar K/2$, before absorbing a photon with momentum $p = -\hbar K/2$, and subsequently emits a second photon with the momentum $p = \hbar K/2$. This is the only scattering process which classically conserves energy, whilst also conserving the quasimomentum. We therefore expect that scattering into states with momentum $p > |\hbar K/2|$ ought to be strongly suppressed even under the fully quantum time evolution. We explore this simplified picture in Chapter 14.

Chapter 14

Reduction to an effective two-state system

14.1 Simplification

We may test the conjecture that population transfer into states with $k < -1$ or $k > 0$ is strongly suppressed by computing the full time evolution of the system numerically; the results of such calculations on an exhaustive basis of momentum states are displayed in Fig 14.1. Over the 13 basis states displayed, we can clearly see that, though population transfer into higher order modes does occur, the oscillation of population between the $k = -1$ and $k = 0$ states is the dominant process in the system. We therefore expect that a representation of the system in a truncated momentum basis composed of only these two states ought to capture the essential dynamics, and explore this simplified two-state model below.
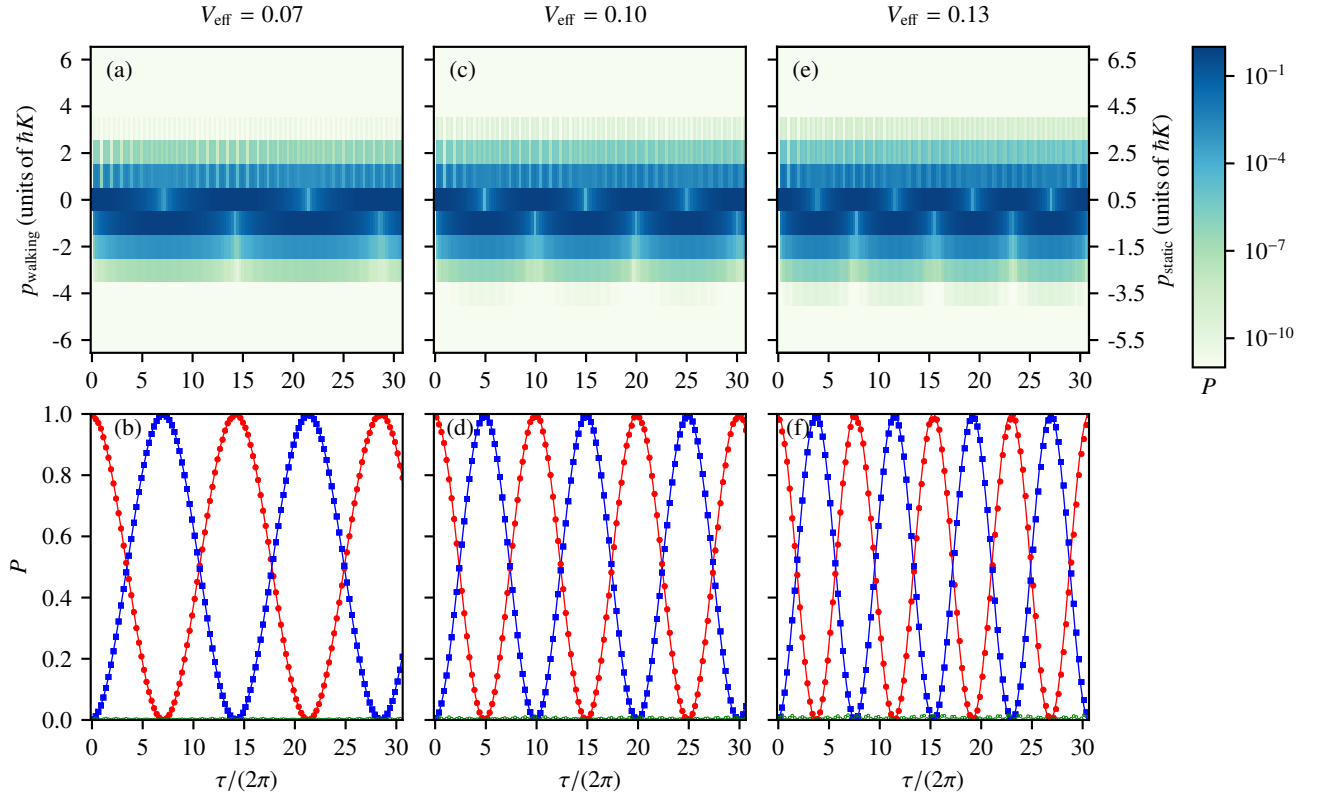
Figure 14.1: Time evolved momentum distributions for an atomic gas initially prepared in the $|k = 0, \beta = 1/2\rangle$ momentum state (corresponding to the $|k = 0, \beta = 0\rangle$ state in the lab frame for a walking grating), as calculated numerically on a basis of 2048 momentum states. The top row of false color plots [(a),(c),(e)] shows the population in the first 13 momentum states, to be read on the logarithmic colorbar to the right; a cutoff population of $P_{\text{cutoff}} = 10^{-11}$ has been applied to accommodate the log scale. The labels p_{static} and p_{walking} denote the momentum as measured in the lab frame for the case of a static and a walking grating respectively. The bottom row of plots [(b),(d),(f)] shows the time evolution of the population in the $|k = 0\rangle$ (red circles) and $|k = -1\rangle$ (blue squares) states, where the solid line through each curve is given by the analytic solution of Eqs. (14.2.3a) and (14.2.3b). Also shown is the population in the $|k = 1\rangle$ state (green points). Each column of plots corresponds to a simulation for a fixed value of the effective lattice depth V_{eff}, here, from left to right $V_{\text{eff}} = 0.07, 0.10, 0.13$ respectively.

14.2 Two-state model analytics

We may represent the Hamiltonian (13.2.2) in the $\beta = 1/2$ subspace, which corresponds to the desired initial momentum $p = \hbar K/2$, using the following two-state momentum basis:

$$|k = 0\rangle = \begin{pmatrix} 1 \\ 0 \end{pmatrix}, \tag{14.2.1a}$$

$$|k = -1\rangle = \begin{pmatrix} 0 \\ 1 \end{pmatrix}, \tag{14.2.1b}$$

yielding:

$$H_{\mathrm{Latt}}^{2\times2} = \begin{pmatrix} 1/8 & -V_{\mathrm{eff}}/2 \\ -V_{\mathrm{eff}}/2 & 1/8 \end{pmatrix}. \tag{14.2.2}$$

We recognize Eq. (14.2.2) as a Rabi matrix with zero detuning, the eigenvectors and eigenvalues of which are well known [96], and can be used to straightforwardly determine the time evolution of the population in the $|k = 0\rangle$ and $|k = -1\rangle$ states, respectively:

$$P_0 = \cos^2(V_{\mathrm{eff}}\tau/2), \tag{14.2.3a}$$

$$P_{-1} = \sin^2(V_{\mathrm{eff}}\tau/2), \tag{14.2.3b}$$

as outlined in Appendix B.5. This analytic result is compared to our exact numerics in Figs. 14.1 and 14.2, both of which show excellent agreement for a wide range of experimentally relevant values of the effective lattice depth V_{eff}. We note in particular that the form of Eqs. (14.2.3a) and (14.2.3b) is such that there is an exact universality between τ and V_{eff}, which is elucidated in Fig. 14.2(b), where all population curves fall on top of each other.
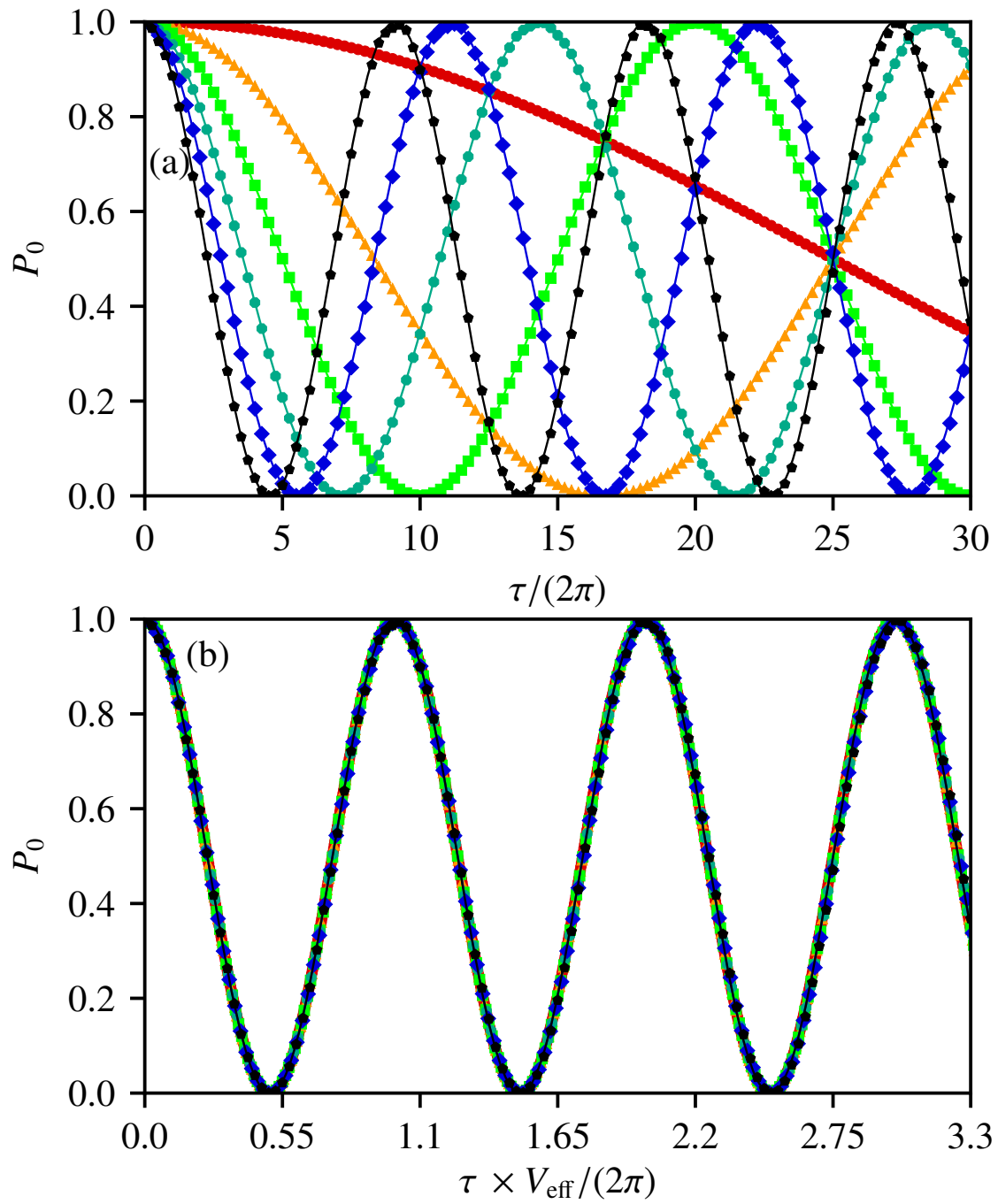
Figure 14.2: (a): Plot of P_0, the population in the $|k = 0\rangle$ state, versus τ, as calculated on a basis of 2048 momentum states using a split-step Fourier method (solid markers). The solid lines correspond to the analytic solution for P_0 in a two state basis, as given by Eq. (14.2.3a). Each set of markers corresponds to a fixed value of the effective lattice depth ranging from the slowest-oscillating curve at $V_{\mathrm{eff}} = 0.01$ to the fastest oscillating one at $V_{\mathrm{eff}} = 0.11$ in steps of 0.02. (b): Reproduction of (a), with the number of pulses axis scaled by V_{eff} to reveal a universal curve both in the analytics and the numerical simulations. The data have been extended to span the full range of the horizontal axis.

Chapter 15

Finite-temperature response

15.1 Other values of β

In the following section we consider the effect of evolving initial states with quasimomentum different to $\beta = 1/2$ in order to gain insight into the dynamics of a finite-temperature gas. Numerically, this is achieved by computing the evolution of an initial state $|k + \beta\rangle$ under the time evolution operator (13.2.4). We make the assumption from the outset that the initial momentum distribution of the gas (centred at $\beta = 1/2$) spans less than half of each of the $k = 0$ and $k = -1$ Brillouin zones for a static grating (or falls within the $k = 0$ Brillouin zone with a momentum distribution centered on $\beta = 0$ for a walking grating). Our results in this low temperature regime are displayed in Fig. 15.1, which indicates a $k = 0$ Brillouin zone with high amplitude but low-frequency oscillations in the population of the zeroth diffraction order centered around $|\beta| = 1/2$, and low amplitude but rapidly oscillating solutions as β is detuned from this value.

We may also use our simplified semiclassical model of Chapter 14 to derive an approximate analytic result for the same calculation, in which the quasimomentum β is encoded as a detuning to be included in our initial Rabi model of Eq. (14.2.2). These additions yield the

following 2×2 Hamiltonian matrix:

$$H_{\text{Latt}}^{2 \times 2}(\beta) = \begin{pmatrix} \beta^2/2 & -V_{\text{eff}}/2 \\ -V_{\text{eff}}/2 & (1 - 2\beta + \beta^2)/2 \end{pmatrix}, \tag{15.1.1}$$

in which β is now a free parameter. The time evolution of the zeroth diffraction order population governed by this matrix can be found using the approach given in Appendix B.6, thus:

$$P_0(\beta) = 1 - \frac{V_{\text{eff}}^2}{(\beta - 1/2)^2 + V_{\text{eff}}^2} \sin^2\left(\sqrt{(\beta - 1/2)^2 + V_{\text{eff}}^2} \frac{\tau}{2} \right), \tag{15.1.2}$$

which is similar to the result reported in [89] for a zero temperature gas, and agrees excellently with the exact numerics for physically relevant parameters as shown in Fig. 15.1. We therefore expect that thermal averaging of this result should produce an accurate description of the full finite-temperature response.

15.2   Finite temperature analysis

To find the finite temperature response of the system we weight the contribution of Eq. (15.1.2) for each individual quasimomentum subspace according to the Maxwell-Boltzmann distribution:

$$D_{k=0}(\beta, w) = \frac{1}{w \sqrt{2\pi}} \exp\left(\frac{-(\beta - 1/2)^2}{2w^2} \right), \tag{15.2.1}$$

where the dimensionful temperature is given by $\mathcal{T}_w = \hbar^2 K^2 w^2 / M k_{\text{B}}$ [51]. Mathematically this corresponds to the integral:

$$P_{0,\text{total}}(w) = \int_0^1 D_{k=0}(\beta, w) P_0(\beta) \, d\beta. \tag{15.2.2}$$

Inserting Eqs. (15.2.1) and (15.1.2), we have:

$$P_{0,\text{total}}(\rho) = \frac{1}{\sqrt{2\pi}\rho} \int_{\frac{-1}{2}}^{\frac{1}{2}} \exp\left(\frac{-\gamma^2}{2\rho^2} \right) \left[1 - \frac{1}{\gamma^2 + 1} \sin^2\left(\frac{\sqrt{\gamma^2 + 1}}{2} \phi \right) \right] d\gamma, \tag{15.2.3}$$
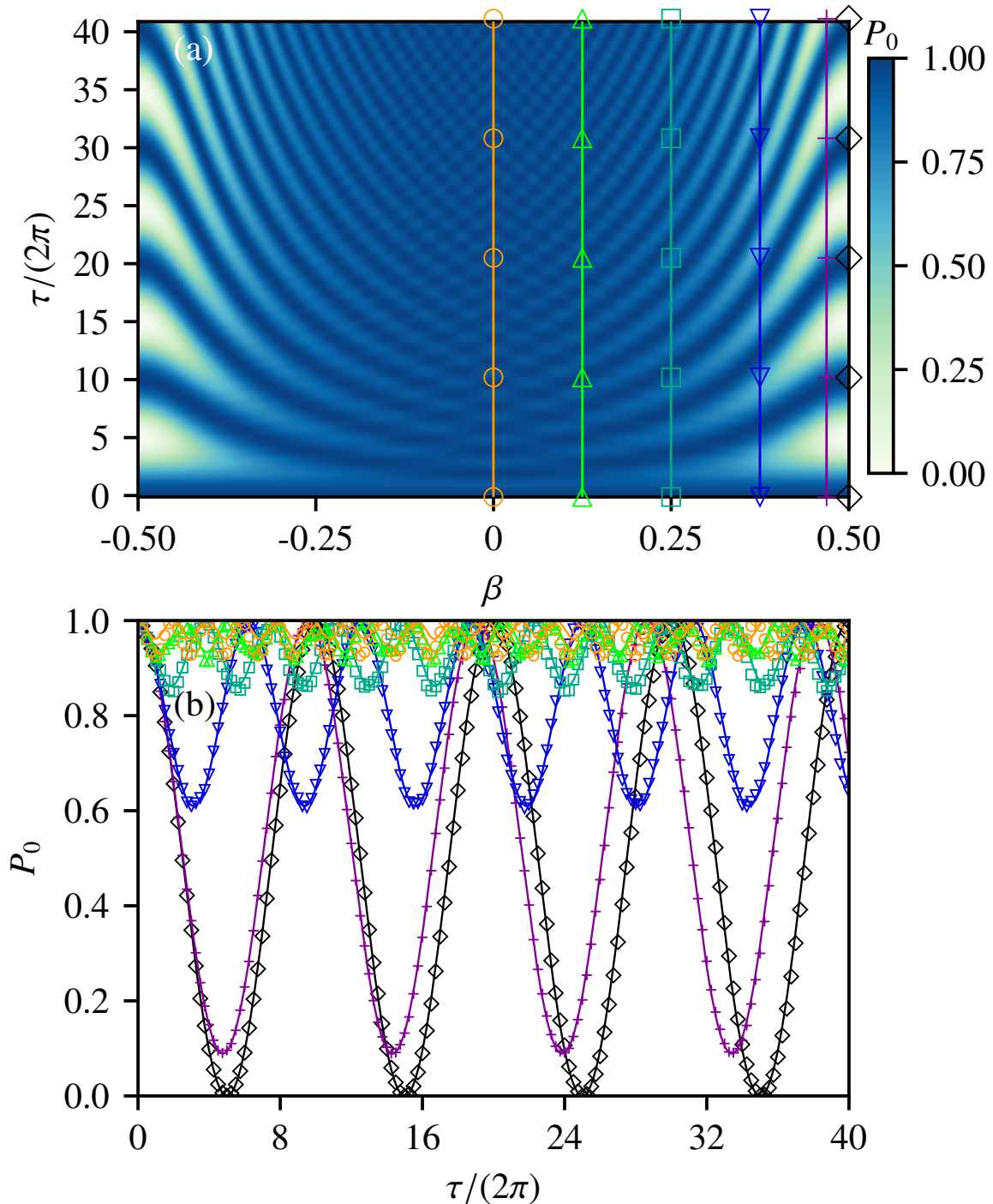
Figure 15.1: (a): False-color plot of the time evolution of P_0 as computed in a basis of 2048 momentum states for values of the dimensionless quasimomentum β [see Eqs. (13.2.3b,13.2.3c)] ranging from $\beta = -0.5$ to $\beta = 0.5$ in steps of $\beta = 0.00025$ (4001 quasimomentum values). We have chosen a relatively large lattice depth of $V_{\text{eff}} = 0.1$ such that the different dynamical behaviors are made clear for the chosen evolution time $\tau/(2\pi) = 40$. (b): Slices taken through the quasimomentum distribution parallel to the time axis for $\beta = 0, 0.0625, 0.125$, then increasing in increments of $\beta = 0.125$ up to a maximum of $\beta = 0.5$, enclosing the full range of dynamics in the $k = 0$ subspace. Each vertical set of markers in (a) corresponds to the position in the quasimomentum distribution of the slices in (b), where the solid lines represent our analytic solution for each β subspace [Eq. (15.1.2)].

where we have introduced $\gamma = (\beta - 1/2)/V_{\text{eff}}$, $\phi = V_{\text{eff}}\tau$ and $\rho = w/V_{\text{eff}}$ for simplicity. The exponential and trigonometric terms can be power expanded, and the integral (15.2.3) solved term by term, giving:

$$P_{0,\text{total}}(\rho) = 1 - \sum_{s=0}^{\infty} \sum_{q=0}^{s} u_s(\phi) M_{s,q} v_q(\rho), \qquad (15.2.4)$$

where $u_s(\phi) = (-\phi^2)^{s+1} s!/[2(s+1)]!$, $M_{s,q} = -(2q)!/[2(q!)^2(s-q)!]$ and $v_q(\rho) = (\rho^2/2)^q$ (see Appendix B.7). Equation (15.2.4) can in principle be solved numerically by recursively populating the elements of a sufficiently large pair of $u(\phi)$, $v(\rho)$ vectors and M matrix, though the elements of the vectors will grow with s and q respectively unless ϕ and ρ are sufficiently small, and this condition is only satisfied for certain experimentally relevant regimes. Nonetheless, Eq. (15.2.4) yields some insight when expressed as a sum over derivatives of sinc functions (see Appendix B.8):

$$P_{0,\text{total}}(\rho) = 1 - \sum_{q=0}^{\infty} \left(\frac{\rho}{2}\right)^{2q} \frac{(2q)!}{q!^2} \left\{ \left(\frac{\phi}{2}\right)^{2(q+1)} \left[\left(\frac{2}{\phi}\right) \frac{\mathrm{d}}{\mathrm{d}(\phi/2)}\right]^q \left[\frac{\sin^2(\phi/2)}{(\phi/2)^2}\right] \right\}. \qquad (15.2.5)$$

With $q = 0$, Eq. (15.2.5) reduces to the zero temperature result of Eq. (14.2.3a), as such we should expect the finite temperature behavior of the system to be captured in terms with $q > 0$. Though the full sum over q is always convergent, the presence of the $(\phi/2)^{2(q+1)}$ term guarantees that all individual terms with $q \geq 1$ diverge, meaning that a preferred truncation of the sum is not obvious.

However, given the well-behaved nature of the integrand, Eq. (15.2.3) can be straightforwardly integrated numerically, for instance using the trapezium rule. We compare this numerical integration to our full finite-temperature numerics in Fig. 15.2, which shows excellent agreement across a large range of initial momentum widths in the weak lattice regime [Figs. 15.2 (a),(b)], and for $V_{\text{eff}} = 0.1$ in the strong lattice regime [Fig. 15.2 (d)]. However, for $V_{\text{eff}} = 0.5$ [Fig. 15.2 (c)] the agreement is relatively poor, as in this regime the semiclassically motivated two-state model is no longer valid. We therefore expect that numerically fitting Eq. (15.2.3) to experimental data, with $\phi = V_{\text{eff}}\tau$ and $\rho = w/V_{\text{eff}}$ as free parameters, would give an accurate value of the effective lattice depth, if the time τ is known to high precision and the lattice depth is sufficiently small. Further, we note that using standard integral
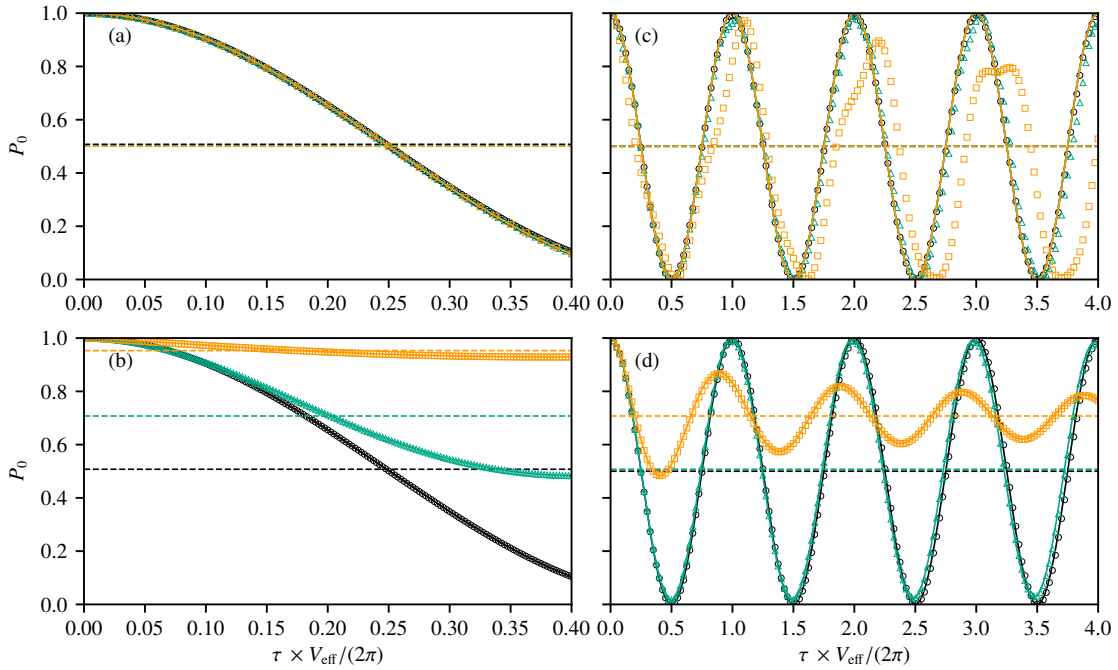
Figure 15.2: Plot of the finite temperature response of P_0 versus $\tau \times V_{\text{eff}}$, where V_{eff} is the dimensionless lattice depth [see Eq. (13.2.4)], as calculated for an ensemble of 4001 particles each evolved in a basis of 2048 momentum states (hollow markers). The left column [(a), (b)] corresponds to the weak-lattice regime, and the right column [(c), (d)] to the strong-lattice regime. The top row of plots [(a), (c)] shows the finite-temperature response of P_0 at a temperature of $w = 0.00125$ for a selection of different lattice depths, $V_{\text{eff}} = 0.01, 0.02, 0.05$ (all curves fall on top of each other) in the weak regime (a) and $V_{\text{eff}} = 0.1, 0.2, 0.5$ (lower, middle and uppermost curves) in the strong regime (c). For the bottom row [(b), (d)], each set of curves and markers corresponds to the response of P_0 at a different temperature [$w = 0.00125, 0.0125, 0.125$; lower (black circles), middle (blue triangles) and uppermost (yellow squares) curves respectively], where the effective lattice depth is kept constant at $V_{\text{eff}} = 0.1$ in the strong-lattice case and $V_{\text{eff}} = 0.01$ the weak-lattice case. In all panels, the solid lines represent the result yielded by numerically integrating Eq. (15.2.3). The horizontal dashed lines correspond to the result of the steady state solution of Eq. (15.2.6) for each set of parameters.

results, we may also extract the steady state solution to Eq. (15.2.3) as $\phi \to \infty$:

$$P_{0,\text{total},\phi\to\infty}(\rho) = \frac{1}{2\rho} \sqrt{\frac{\pi}{2}} \exp\left(\frac{1}{2\rho^2}\right) \text{Erfc}\left(\frac{1}{\sqrt{2}\rho}\right), \tag{15.2.6}$$

which depends only on $\rho = w/V_{\text{eff}}$ [35]. Here, 'Erfc' is the complementary error function [97].[a] In essence, by measuring the steady state population experimentally, and numerically fitting Eq. (15.2.6), $\rho = w/V_{\text{eff}}$ can be straightforwardly determined and substituted into Eq. (15.2.3), leaving a fit in only one parameter $\phi = V_{\text{eff}}\tau$. The steady state population can be found either by allowing the atomic gas to evolve in the lattice for a sufficiently long time, or taking the average value of P_0 in time for an appropriate number of oscillations. In fact, this improved fitting approach not only allows $\phi = V_{\text{eff}}\tau$, and therefore the effective lattice depth V_{eff} to be determined more accurately, but also allows the initial effective temperature to be determined from $w = \rho V_{\text{eff}}$.

---

[a]When evaluating Eq. (15.2.6) for physically relevant values of $\rho = w/V_{\text{eff}}$, the exponential term becomes large as the error function takes a correspondingly small value such that $P_{0,\phi\to\infty}(\rho)$ remains bounded between 0 and 1. This complication can present a problem for numerical evaluation using standard numerical routines. In practice, we numerically implement Eq. (15.2.6) exclusively in terms of rational numbers in Mathematica, before requesting a numerical evaluation to a specified precision. One could also use standard asymptotic formulas for the product of an exponential and an error function for the evaluation.

> **Chapter Summary**
>
> - We have presented a simplified model system yielding an analytic zero-temperature formula for the evolution of the zeroth diffraction order population, and demonstrated the validity of this approach across a wide range of lattice depths. We have also noted that this formula contains an exact universality in the dimensionless time and effective lattice depth, which can be represented as a universal curve.
>
> - We have extended this model to incorporate finite-temperature effects and discussed from where they arrive mathematically. We have also shown that the frequency and amplitude of the oscillations in the population of the zeroth order momentum state are extremely robust to these finite-temperature effects, especially as compared to the population dynamics of a the multipulse approach described in Part II.
>
> - We have shown that there is excellent agreement between this analytic model and exact numerical calculations if the lattice depth is sufficiently small, and shown that a steady state solution exists, which may be useful for determining the lattice depth and initial temperature of a gas from a single set of population measurements.
>
> - With regard to potential experimental implementations, we note that the phase velocity of a walking optical lattice can be calibrated extremely precisely; however, this does require optical elements to be in place which will reduce the intensity of the laser beam and therefore the lattice. The alternative is to impart a specified momentum to an initially stationary BEC; it is unlikely that this can be achieved with the same level of precision, however with such a scheme there is no need for any additional optical elements affecting the lattice depth.

Chapter 16

Conclusions

In conclusion, we have presented intuitive and simple models for the diffraction of cold dilute atomic gases by single and multiple laser standing-wave pulses which we believe will be of use to experimentalists in the field for understanding existing experiments and planning new ones. Specifically, we have shown that the ϵ-pseudoclassical model of Part I is capable of treating quantum resonances with finite duration laser standing-wave pulses. The model reduces the computational time necessary to simulate such experiments for finite temperature gases and offers insight beyond standard methods in that it gives a clear visualization of the dynamics of the diffracted ensemble, especially in terms of the momentum spread, which can be understood in terms of bounded quasiperiodic orbits about resonances in phase space. We note also that in further work, the model can be extended to include gravitational effects, which will be of further use for planning atom interferometry experiments.

In Part II, we have presented an analytic formula for population oscillations in the zeroth order momentum state which improves on those currently used in state of the art measurements of weak lattice depths. We have also characterized the domain of validity of this formula in magnitude of lattice depth and number of pulse sequences, and shown that a five state model which is solvable analytically, captures the essential features for experimentally relevant choices of parameters. The effects of finite-temperature initial momentum distributions on such experiments have been investigated.

We note in particular that the lattice depth measurement scheme described in Part III, which

we have shown to be especially robust to finite-temperature effects and mode leakage, is simple to implement experimentally compared to many atom-optical setups, and offers the advantage that population measurements can be gathered over large experimental times, with minimal heating. An advantage of this approach is that it makes it possible in principle to determine both the width of the initial momentum distribution of the atomic gas and the lattice depth from one set of population measurements.

In all three Parts, we have elucidated universalities in time and lattice depth (driving strength), which reduce the space of parameters to be considered in interpreting and planning atom diffraction experiments.

Appendix A

Time evolution for 2 diffraction orders

A.1 Floquet operator in two-state basis

We may calculate the time evolution of the $|0\rangle$ and $|+\rangle$ state populations by first diagonalizing Eq. (9.0.3) (reproduced here for convenience)

$$H_{\text{Trunc}} = \begin{pmatrix} 1/2 & -V_{\text{eff}}/\sqrt{2} \\ -V_{\text{eff}}/\sqrt{2} & 0 \end{pmatrix}, \tag{A.1.1}$$

using the well known eigenvalues and normalized eigenvectors of a Rabi matrix, $E_{\pm} = (1 \pm \sqrt{1 + 8V_{\text{eff}}^2})/4$, and

$$|E_+\rangle = \begin{pmatrix} \cos(\alpha/2) \\ -\sin(\alpha/2) \end{pmatrix}, \tag{A.1.2a}$$

$$|E_-\rangle = \begin{pmatrix} \sin(\alpha/2) \\ \cos(\alpha/2) \end{pmatrix}, \tag{A.1.2b}$$

respectively, where $\alpha = \arctan(2\sqrt{2}V_{\text{eff}})$. H_{Trunc} can then be written:

$$H_{\text{diag}} = R^{\dagger} H_{\text{Trunc}} R = \begin{pmatrix} E_+ & 0 \\ 0 & E_- \end{pmatrix}, \tag{A.1.3}$$

such that R is the matrix of normalized eigenvectors. This leads directly to the part of the Floquet operator governing the lattice evolution:

$$F_{\text{Latt}} = R^{\dagger} \begin{pmatrix} e^{-2\pi i E_{+}} & 0 \\ 0 & e^{-2\pi i E_{-}} \end{pmatrix} R. \tag{A.1.4}$$

Expressing F_{Free} in the truncated momentum basis, $|0\rangle_2 \equiv \begin{pmatrix} 0 \\ 1 \end{pmatrix}$; $|+\rangle_2 \equiv \begin{pmatrix} 1 \\ 0 \end{pmatrix}$, we can represent the total Floquet operator in matrix form thus:

$$F = F_{\text{Free}} F_{\text{Latt}} = \begin{pmatrix} -1 & 0 \\ 0 & 1 \end{pmatrix} R^{\dagger} \begin{pmatrix} e^{-2\pi i E_{+}} & 0 \\ 0 & e^{-2\pi i E_{-}} \end{pmatrix} R. \tag{A.1.5}$$

A.2 Floquet evolution for a general two-level system

Any time-evolution operator associated with a two-level system can be expressed as a 2×2 unitary matrix, and all unitary matrices are diagonalizable, hence we may represent such a time-evolution operator thus:

$$U = S\, U_{\text{diag}} S^{\dagger} = \begin{pmatrix} v_1^{+} & v_1^{-} \\ v_0^{+} & v_0^{-} \end{pmatrix} \begin{pmatrix} \lambda^{+} & 0 \\ 0 & \lambda^{-} \end{pmatrix} \begin{pmatrix} v_1^{+} & v_1^{-} \\ v_0^{+} & v_0^{-} \end{pmatrix}^{\dagger}. \tag{A.2.1}$$

Here S is a matrix composed of the normalized eigenvectors of U:

$$\vec{v}_{+} = \begin{pmatrix} v_1^{+} \\ v_0^{+} \end{pmatrix}, \qquad \vec{v}_{-} = \begin{pmatrix} v_1^{-} \\ v_0^{-} \end{pmatrix}, \tag{A.2.2}$$

and $\lambda^{\pm}$ are the corresponding eigenvalues of U, which have unit magnitude and so can be expressed as:

$$\lambda^{\pm} = \exp(-i\theta_{\pm}), \tag{A.2.3}$$

where θ_+ and θ_- are phase angles to be determined. The matrix which produces N successive evolutions can therefore be written:

$$
\begin{aligned}
U = S\,U_{\text{diag}}^N S^\dagger &= \begin{pmatrix} v_1^+ & v_1^- \\ v_0^+ & v_0^- \end{pmatrix} \begin{pmatrix} (\lambda^+)^N & 0 \\ 0 & (\lambda^-)^N \end{pmatrix} \begin{pmatrix} v_1^+ & v_1^- \\ v_0^+ & v_0^- \end{pmatrix}^\dagger \\
&= \begin{pmatrix} (\lambda^+)^N |v_1^+|^2 + (\lambda^-)^N |v_1^-|^2 & (\lambda^+)^N v_1^+ (v_0^+)^* + (\lambda^-)^N v_1^- (v_0^-)^* \\ (\lambda^+)^N v_0^+ (v_1^+)^* + (\lambda^-)^N v_0^- (v_1^-)^* & (\lambda^+)^N |v_0^+|^2 + (\lambda^-)^N |v_0^-|^2 \end{pmatrix}.
\end{aligned}
\tag{A.2.4}
$$

Suppose that the initial state of the system can be represented by $|0\rangle_2 \equiv \begin{pmatrix} 0 \\ 1 \end{pmatrix}$, and the excited state by $|+\rangle_2 \equiv \begin{pmatrix} 1 \\ 0 \end{pmatrix}$, the probability of the system occupying the $|0\rangle$ state after N evolutions can be written:

$$
P_0(N) = \left| \begin{pmatrix} 0 & 1 \end{pmatrix} U^N \begin{pmatrix} 0 \\ 1 \end{pmatrix} \right|^2 = \left\| \left[(\lambda^+)^N |v_0^+|^2 + (\lambda^-)^N |v_0^-|^2 \right] \right\|^2,
\tag{A.2.5}
$$

which is the absolute square of the bottom-right matrix element of Eq. (A.2.4). The corresponding probability of the system being in the $|+\rangle$ state is simply $P_+(N) = 1 - P_0(N)$. Since S is a unitary matrix, v_0^+ and v_0^- must satisfy $|v_0^+|^2 + |v_0^-|^2 = 1$, using this identity and inserting Eq. (A.2.3), $P_0(N)$ and $P_+(N)$ can be written:

$$
P_0(N) = 1 - 4|v_0^+|^2 |v_0^-|^2 \sin^2(N[\theta_+ - \theta_-]/2)
\tag{A.2.6a}
$$

$$
P_+(N) = 4|v_0^+|^2 |v_0^-|^2 \sin^2(N[\theta_+ - \theta_-]/2).
\tag{A.2.6b}
$$

By finding $v_0^\pm$ and $\theta_\pm$ for our specific Floquet operator (A.1.5), we explicitly determine Eq. (A.2.6a) and (A.2.6b), in terms of the number of pulses N and the effective potential depth V_{eff}, this is the origin of Eq. (9.0.4a) and (9.0.4b).

A.3   Back to the system Floquet operator

Both the amplitude $A = 4|v_0^+|^2 |v_0^-|^2$, and the oscillation frequency $\phi = \theta_+ - \theta_-$ can be determined by calculating the eigenvalues and eigenvectors of the Floquet operator (A.1.5),

reproduced here for convenience:

$$F = F_{\text{Free}} F_{\text{Latt}} = \begin{pmatrix} -1 & 0 \\ 0 & 1 \end{pmatrix} R^{-1} \begin{pmatrix} e^{-2\pi i E_+} & 0 \\ 0 & e^{-2\pi i E_-} \end{pmatrix} R, \tag{A.3.1}$$

where

$$R = \begin{pmatrix} \cos(\alpha/2) & -\sin(\alpha/2) \\ \sin(\alpha/2) & \cos(\alpha/2) \end{pmatrix}. \tag{A.3.2}$$

Introducing $\mu_\pm = e^{-2\pi i E_\pm}$, $\cos(\alpha/2) = c$ and $\sin(\alpha/2) = s$, we can express (A.1.5) in the the more compact form:

$$F = \begin{pmatrix} -\mu_+ c^2 - \mu_- s^2 & \mu_+ cs - \mu_- cs \\ -\mu_+ cs + \mu_- cs & \mu_+ c^2 + \mu_- s^2 \end{pmatrix}. \tag{A.3.3}$$

Using $s^2 = 1 - c^2$ we can write (A.3.3) as:

$$F = \begin{pmatrix} -c^2(\mu_+ - \mu_-) - \mu_- & cs(\mu_+ - \mu_-) \\ -cs(\mu_+ - \mu_-) & s^2(\mu_+ - \mu_-) + \mu_- \end{pmatrix}. \tag{A.3.4}$$

Further, introducing the shorthand $\bar{c}^2 \equiv c^2(\mu_+ - \mu_-)$, $\bar{s}^2 \equiv s^2(\mu_+ - \mu_-)$, $\overline{sc} \equiv sc(\mu_+ - \mu_-)$, we have:

$$F = \begin{pmatrix} -\bar{c}^2 - \mu_- & \overline{sc} \\ -\overline{sc} & \bar{s}^2 + \mu_- \end{pmatrix}, \tag{A.3.5}$$

the eigenvalues of which can be written:

$$\lambda_\pm = \frac{1}{2}\left(-\left(\bar{c}^2 - \bar{s}^2\right) \pm \sqrt{\left(\bar{c}^2 - \bar{s}^2\right)^2 + 4\mu_-\left\{\bar{c}^2 - \bar{s}^2 + \mu_-\right\}} \right). \tag{A.3.6}$$

Noting that $(\bar{c}^2 - \bar{s}^2)^2 = (c^2 - s^2)(\mu_+ - \mu_-)^2$, and $(c^2 - s^2)^2 = 1 - 4s^2 c^2$, we can simplify the argument of the radical $(\bar{c}^2 - \bar{s}^2)^2 + 4\mu_-\{\bar{c}^2 - \bar{s}^2 + \mu_-\} = (\mu_+ + \mu_-)^2 - 4s^2 c^2(\mu_+ - \mu_-)^2$, leading to:

$$\lambda_\pm = \frac{(\mu_+ - \mu_-)}{2}\left[-\left(c^2 - s^2\right) \pm \sqrt{-4s^2 c^2 + \left(\frac{\mu_+ + \mu_-}{\mu_+ - \mu_-}\right)^2} \right]. \tag{A.3.7}$$

Recalling that $\mu_\pm = e^{-2\pi i E_\pm}$, and $E_\pm = (1 \pm \sqrt{1 + 8V_{\text{eff}}^2})/4$, it can be shown that

$$
\begin{aligned}
(\mu_+ - \mu_-) &= -\left(e^{i\pi[E_+ - E_-]} - e^{-i\pi[E_+ - E_-]}\right)e^{-i\pi[E_+ + E_-]} \\
&= -2\sin(\pi[E_+ - E_-]),
\end{aligned}
\tag{A.3.8a}
$$

$$
\begin{aligned}
(\mu_+ + \mu_-) &= -\left(e^{i\pi[E_+ - E_-]} + e^{-i\pi[E_+ - E_-]}\right)e^{-i\pi[E_+ + E_-]} \\
&= -2i\cos(\pi[E_+ - E_-]),
\end{aligned}
\tag{A.3.8b}
$$

where we have made use of the fact that $E_+ + E_- = 1/2$, leading to:

$$
\left(\frac{\mu_+ + \mu_-}{\mu_+ - \mu_-}\right)^2 = -\frac{\cos^2(\pi[E_+ - E_-])}{\sin^2(\pi[E_+ - E_-])} = -\cot^2(\pi[E_+ - E_-]).
\tag{A.3.9}
$$

Since (A.3.9) and (A.3.8a) are always real and negative, it is straightforward to separate the eigenvalues (A.3.7) into their real and imaginary parts:

$$
\begin{aligned}
\lambda_\pm &= \text{Re}(\lambda_\pm) + i\,\text{Im}(\lambda_\pm) \\
&= \frac{(\mu_+ - \mu_-)}{2}\left[-\left(c^2 - s^2\right) \pm i\sqrt{4s^2c^2 + \delta^2}\right],
\end{aligned}
\tag{A.3.10}
$$

where we have introduced $\delta \equiv i(\mu_+ + \mu_-)/(\mu_+ - \mu_-)$ and $\delta^2 \equiv -(\mu_+ + \mu_-)^2/(\mu_+ - \mu_-)^2$. We can now solve the eigenvalue equation:

$$
F\begin{pmatrix} v_1^\pm \\ v_0^\pm \end{pmatrix} = \frac{(\mu_+ - \mu_-)}{2}\left[-\left\{c^2 - s^2\right\} \pm i\sqrt{4s^2c^2 + \delta^2}\right]\begin{pmatrix} v_1^\pm \\ v_0^\pm \end{pmatrix},
\tag{A.3.11}
$$

for $v_0^\pm, v_1^\pm$. Equation (B.5.2) leads directly to:

$$
v_1^\pm = i\left[\epsilon \pm \sqrt{\epsilon^2 + 1}\right]v_0^\pm,
\tag{A.3.12}
$$

where we have introduced the shorthand $\epsilon \equiv -\delta/2sc$. We can now state that:

$$
\vec{v}_+ \propto \begin{pmatrix} i\left[\epsilon + \sqrt{\epsilon^2 + 1}\right] \\ 1 \end{pmatrix}, \qquad \vec{v}_- \propto \begin{pmatrix} i\left[\epsilon - \sqrt{\epsilon^2 + 1}\right] \\ 1 \end{pmatrix},
\tag{A.3.13}
$$

and noting that $\sqrt{\epsilon^2 + 1} - \epsilon = \left[\sqrt{\epsilon^2 + 1} + \epsilon\right]^{-1}$, we can express the normalized eigenvectors thus:

$$\vec{v}_+ = \frac{1}{\sqrt{2\sqrt{\epsilon^2 + 1}}} \begin{pmatrix} i\sqrt{\sqrt{\epsilon^2 + 1} + \epsilon} \\ \sqrt{\sqrt{\epsilon^2 + 1} - \epsilon} \end{pmatrix}, \tag{A.3.14a}$$

$$\vec{v}_- = \frac{1}{\sqrt{2\sqrt{\epsilon^2 + 1}}} \begin{pmatrix} \sqrt{\sqrt{\epsilon^2 + 1} - \epsilon} \\ i\sqrt{\sqrt{\epsilon^2 + 1} + \epsilon} \end{pmatrix}. \tag{A.3.14b}$$

The amplitude $A = 4|v_0^+|^2|v_0^-|^2$ can now be determined from the product of the absolute squares of the bottom entries of $\vec{v}_+$ and $\vec{v}_-$:

$$A = \frac{4}{\left[\sqrt{2\sqrt{\epsilon^2 + 1}}\right]^4} \left(\left[\sqrt{\epsilon^2 + 1} - \epsilon\right]\left[\sqrt{\epsilon^2 + 1} + \epsilon\right]\right)$$

$$= \frac{1}{\epsilon^2 + 1}. \tag{A.3.15}$$

Inserting $\epsilon^2 = \delta^2/4s^2c^2$ and $4s^2c^2 = \sin^2(\alpha) = \sin^2(\arcsin(2\sqrt{2}V_{\text{eff}}/\sqrt{1 + 8V_{\text{eff}}^2})) = 8V_{\text{eff}}^2/(1 + 8V_{\text{eff}}^2)$ we can express the amplitude in terms of the effective lattice-depth V_{eff}:

$$A = \frac{8V_{\text{eff}}^2 \sin^2\left(\pi\sqrt{1 + 8V_{\text{eff}}^2}/2\right)}{8V_{\text{eff}}^2 + \cos^2\left(\pi\sqrt{1 + 8V_{\text{eff}}^2}/2\right)}, \tag{A.3.16}$$

which corresponds to Eq. (9.0.4c). Using Eq. (A.3.10), we can also determine the oscillation frequency $\phi = \theta_+ - \theta_- = \arg(\lambda_-) - \arg(\lambda_+)$. We can express ϕ as:

$$\phi = \arctan\left(\frac{\text{Im}(\lambda_-)}{\text{Re}(\lambda_-)}\right) - \arctan\left(\frac{\text{Im}(\lambda_+)}{\text{Re}(\lambda_+)}\right) = 2\arctan\left(\frac{\text{Im}(\lambda_-)}{\text{Re}(\lambda_-)}\right),$$

where we have used the relations $\text{Re}(\lambda_-) = \text{Re}(\lambda_+)$, and $\text{Im}(\lambda_+) = -\text{Im}(\lambda_-)$. Substituting in $\text{Re}(\lambda_-) = -(\mu_+ - \mu_-)(c^2 - s^2)/2$ and $\text{Im}(\lambda_-) = -(\mu_+ - \mu_-)\sqrt{4s^2c^2 + \delta^2}/2$ we have:

$$\phi = 2\arctan\left(\frac{\sqrt{4s^2c^2 + \delta^2}}{c^2 - s^2}\right), \tag{A.3.17}$$

which, noting that $4s^2c^2 = 8V_{\text{eff}}^2/(1 + 8V_{\text{eff}}^2)$ and recalling that $\delta^2 = \cot^2(\pi\sqrt{1 + 8V_{\text{eff}}^2}/2)$, can be written:

$$\phi = 2\arctan\left(\frac{\sqrt{8V_{\text{eff}}^2 + \cos^2(\pi\sqrt{1 + 8V_{\text{eff}}^2}/2)}}{\sin(\pi\sqrt{1 + 8V_{\text{eff}}^2}/2)}\right),$$

which corresponds to Eq. (9.0.4d).

Appendix B

Limiting behaviours of Equations (9.0.4c) and (9.0.4d)

B.1 Weak coupling regime

Equation (9.0.4d) can be linearized in the weak coupling regime as $V_{\text{eff}} \to 0$. To clarify the procedure, we introduce the following notation:

$$\phi = 2 \arctan\left(\frac{Y}{X}\right), \tag{B.1.1a}$$

$$Y = \sqrt{8V_{\text{eff}}^2 + \cos^2\left(\frac{\pi}{2}\sqrt{1 + 8V_{\text{eff}}^2}\right)}, \tag{B.1.1b}$$

$$X = \sin\left(\frac{\pi}{2}\sqrt{1 + 8V_{\text{eff}}^2}\right). \tag{B.1.1c}$$

Clearly as $V_{\text{eff}} \to 0$, it follows that $Y \to \cos(\pi/2) = 0$, $X \to \sin(\pi/2) = 1$, and therefore $\phi \to 2\arctan(0/1) = 0$. However, we can still find an approximation to ϕ that is linear in V_{eff} by means of a Taylor expansion:

$$\phi = 2\arctan(Z) \approx Z - \frac{Z^3}{3} + \frac{Z^5}{5} \dots, \tag{B.1.2}$$

101

where $Z = Y/X$. Hence, near $V_{\text{eff}} = 0$, ϕ is given approximately by $\phi \approx 2Y/X$. Note that $\sin(\theta) = \cos(\theta - \frac{\pi}{2})$, $\cos(\theta) = -\sin(\theta - \frac{\pi}{2})$, and hence

$$\sin\left(\frac{\pi}{2}\sqrt{1 + 8V_{\text{eff}}}\right) = \cos\left(\frac{\pi}{2}\left[\sqrt{1 + 8V_{\text{eff}}} - 1\right]\right), \tag{B.1.3a}$$

$$\cos\left(\frac{\pi}{2}\sqrt{1 + 8V_{\text{eff}}}\right) = -\sin\left(\frac{\pi}{2}\left[\sqrt{1 + 8V_{\text{eff}}} - 1\right]\right). \tag{B.1.3b}$$

The arguments of the trigonometric functions on the right hand side tend to zero as $V_{\text{eff}} \to 0$, which simplifies the expansions of (B.1.3a) and (B.1.3b), since we can use standard small-angle approximations. We can simplify the arguments further by use of the binomial approximation $\sqrt{1 + \epsilon} \approx 1 + \epsilon/2$, yielding:

$$\cos\left(\frac{\pi}{2}\left[\sqrt{1 + 8V_{\text{eff}}} - 1\right]\right) \approx \cos(2\pi V_{\text{eff}}^2) \approx 1 - \frac{4\pi^2 V_{\text{eff}}^4}{2}, \tag{B.1.4a}$$

$$\sin\left(\frac{\pi}{2}\left[\sqrt{1 + 8V_{\text{eff}}} - 1\right]\right) \approx \sin(2\pi V_{\text{eff}}^2) \approx 2\pi V_{\text{eff}}^2. \tag{B.1.4b}$$

Hence:

$$
\begin{aligned}
Y &= \sqrt{8V_{\text{eff}}^2 + \cos^2\left(\frac{\pi}{2}\sqrt{1 + 8V_{\text{eff}}^2}\right)} \\
&= \sqrt{8V_{\text{eff}}^2 + \sin^2\left(\frac{\pi}{2}\left[\sqrt{1 + 8V_{\text{eff}}^2} - 1\right]\right)} \\
&\approx \sqrt{8V_{\text{eff}}^2 + 4\pi^2 V_{\text{eff}}^4} \\
&\approx 2\sqrt{2}V_{\text{eff}}, \tag{B.1.5} \\
X &= \sin\left(\frac{\pi}{2}\sqrt{1 + 8V_{\text{eff}}^2}\right) = \cos\left(\frac{\pi}{2}\left[\sqrt{1 + 8V_{\text{eff}}^2} - 1\right]\right) \\
&\approx \cos\left(2\pi V_{\text{eff}}^2\right) \approx 1 - 2\pi^2 V_{\text{eff}}^4 \\
&\approx 1. \tag{B.1.6}
\end{aligned}
$$

Therefore, to leading order in V_{eff}, around $V_{\text{eff}} = 0$

$$\phi \approx \frac{2 \times 2\sqrt{2}V_{\text{eff}}}{1} = 4\sqrt{2}V_{\text{eff}}. \tag{B.1.7}$$

We may follow a similar procedure for Eq. (9.0.4c), reproduced here for convenience:

$$A = \frac{8V_{\text{eff}}^2 \sin^2\left(\pi \sqrt{1 + 8V_{\text{eff}}^2}/2\right)}{8V_{\text{eff}}^2 + \cos^2\left(\pi \sqrt{1 + 8V_{\text{eff}}^2}/2\right)}. \tag{B.1.8}$$

Using Eqs. (B.1.3a) and (B.1.3b), it follows that around $V_{\text{eff}} = 0$, $\sin^2\left(\pi \sqrt{1 + 8V_{\text{eff}}^2}/2\right) \approx 1$ and $\cos^2(\pi \sqrt{1 + 8V_{\text{eff}}^2}/2) \approx 0$ leading to:

$$A \approx \frac{8V_{\text{eff}}^2 \times 1}{8V_{\text{eff}}^2 + 0} \approx 1. \tag{B.1.9}$$

B.2 Strong coupling regime

To determine the behavior of ϕ as $V_{\text{eff}} \to \infty$ we first rearrange Eq. (B.1.1b):

$$\begin{aligned}
Y &= \sqrt{8V_{\text{eff}}^2 + \cos^2\left(\frac{\pi}{2}\sqrt{1 + 8V_{\text{eff}}^2}\right)} \\
&= 2\sqrt{2}V_{\text{eff}}\left[1 + \frac{\cos^2\left(\frac{\pi}{2}\sqrt{1 + 8V_{\text{eff}}^2}\right)}{16V_{\text{eff}}^2}\right].
\end{aligned} \tag{B.2.1}$$

Clearly, as $V_{\text{eff}} \to \infty$, $Y \approx 2\sqrt{2}V_{\text{eff}}$, whereas $X = \sin(\pi \sqrt{1 + 8V_{\text{eff}}^2}/2)$ simply oscillates. Therefore, recalling Eq. (B.1.1a), if $X = 0$ and $Y > 0$, then $\phi = \pi$. Also, for nonzero X, then as $V_{\text{eff}} \to \infty$, $Y \to \infty$, and therefore $\phi \to \pi$, either from below ($X > 0$) or above ($X < 0$). The curve of ϕ as a function of V_{eff} crosses through the line where $\phi = \pi$ whenever $\pi \sqrt{1 + 8V_{\text{eff}}^2} = m\pi$ for $m \in \mathbb{Z}^+$, in other words where:

$$V_{\text{eff}} = \sqrt{\frac{4m^2 - 1}{8}}, \tag{B.2.2}$$

or, as $V_{\text{eff}} \to \infty$,

$$V_{\text{eff}} = \frac{m}{\sqrt{2}}. \tag{B.2.3}$$

B.3   Quadratic approximant to Equation (9.0.4b)

Equation (9.0.4b) can be rewritten by means of a Taylor expansion thus:

$$P_+(N, V_{\text{eff}}) = A \sin^2(x) \approx A x^2 - \frac{A}{3} x^4 \ldots, \tag{B.3.1}$$

with $x \equiv N\phi/2$, in a regime where $x \ll 1$. Further, assuming that V_{eff} is near zero, we may replace ϕ and A with our leading order approximations of Eqs. (B.1.7, B.1.9), with $x \approx 2\sqrt{2}N V_{\text{eff}}$. Hence, to leading (quadratic) order in x:

$$P_+(N, V_{\text{eff}}) \approx 8N^2 V_{\text{eff}}^2 \propto N^2, \tag{B.3.2}$$

which corresponds to the result used in [30, 32] where $P_+ \equiv P_1$ and $V_{\text{eff}} = V_0/(16E_{\text{R}}) = U_0/(16E_{\text{R}})$.

B.4   Numerical diagonalization

To diagonalize the lattice Hamiltonian in the zero-quasimomentum subspace, we first express Eq. (8.1.1a) in the following form:

$$\frac{M}{\hbar^2 K^2} \hat{H}_{\text{latt}} = \tilde{H}_{\text{latt}} = \frac{\hat{k}^2}{2} - \frac{V_{\text{eff}}}{2} \left(e^{i2k_l\hat{x}} + e^{-i2k_l\hat{x}} \right). \tag{B.4.1}$$

Here $e^{i2k_l\hat{x}}$ and $e^{-i2k_l\hat{x}}$ are momentum displacement operators, which act on the momentum eigenkets in the following way:

$$e^{i2k_l\hat{x}}|k = \alpha\rangle = |k = \alpha + 1\rangle, \qquad e^{-i2k_l\hat{x}}|k = \alpha\rangle = |k = \alpha - 1\rangle. \tag{B.4.2}$$

The matrix elements of the Hamiltonian can, therefore, be expressed in the momentum basis thus:

$$
\begin{aligned}
\tilde{H}_{\text{latt }\gamma,\alpha} &= \langle k = \alpha|\tilde{H}_{\text{latt}}|k = \gamma\rangle \\
&= \frac{\gamma^2}{2}\delta_{\gamma,\alpha} - \frac{V_{\text{eff}}}{2}(\delta_{\gamma,\alpha-1} + \delta_{\gamma,\alpha+1}) \\
&= \frac{\gamma^2}{4}\delta_{\gamma,\alpha} - \frac{V_{\text{eff}}}{2}\delta_{\gamma,\alpha-1} + \text{H.c,}
\end{aligned}
\tag{B.4.3}
$$

where $\alpha, \gamma \in \mathbb{Z}$. Equation (B.4.3) can then be expressed in matrix form, and numerically diagonalized in order to find the time evolution of an initial momentum eigenstate.

By expressing Eq. B.4.3 in matrix form thus:

$$
H_{\text{latt}} = \begin{pmatrix}
\ddots & \vdots & \vdots & \vdots & \iddots \\
\dots & 1/2 & -V_{\text{eff}}/2 & 0 & \dots \\
\dots & -V_{\text{eff}}/2 & 0 & -V_{\text{eff}}/2 & \dots \\
\dots & 0 & -V_{\text{eff}}/2 & 1/2 & \dots \\
\iddots & \vdots & \vdots & \vdots & \ddots
\end{pmatrix},
\tag{B.4.4}
$$

We may now construct the matrix $P^{n\times n}$ which diagonalizes $H_{\text{latt}}^{n\times n}$, such that $H_{\text{latt,diag}}^{n\times n} = (P^\dagger)^{n\times n}H_{\text{latt}}^{n\times n}P^{n\times n}$. We are led to the expression:

$$
|\psi(t = N)\rangle^{n\times 1} = [H_{\text{free}}^{n\times n}P^{n\times n}H_{\text{latt,diag}}^{n\times n}(P^{n\times n})^\dagger]^N|K = \alpha\rangle^{n\times 1},
\tag{B.4.5}
$$

for $|\psi(t = N)\rangle^{n\times 1}$, the time evolution due to N pulse sequences of an initial eigenstate $|K = \alpha\rangle^{n\times 1}$, where $\alpha \in [-(n-1)/2, (n-1)/2]$. The $n \times 1$ superscript denotes that the ket should be understood as an n-dimensional column vector.

B.5 Derivation of the two-state model

To calculate the time-evolution of the population in the zeroth diffraction order, we construct the time evolution operator in the momentum basis from the Hamiltonian of Eq. (14.2.2),

reproduced here for convenience:

$$H_{\text{Latt}}^{2\times2} = \begin{pmatrix} 1/8 & -V_{\text{eff}}/2 \\ -V_{\text{eff}}/2 & 1/8 \end{pmatrix}. \tag{B.5.1}$$

The diagonal terms simply represent an energy shift that can be transformed away, thus the eigenvalues of Eq. (14.2.2) can simply be read from the off-diagonal: $E_\pm = \pm V_{\text{eff}}/2$. We may now solve the eigenvalue equation:

$$\begin{pmatrix} 0 & -V_{\text{eff}}/2 \\ -V_{\text{eff}}/2 & 0 \end{pmatrix} \begin{pmatrix} v_1^\pm \\ v_0^\pm \end{pmatrix} = \pm V_{\text{eff}}/2 \begin{pmatrix} v_1^\pm \\ v_0^\pm \end{pmatrix}. \tag{B.5.2}$$

Equation (B.5.2) leads directly to $-v_1^\pm = \pm v_0^\pm$, yielding eigenvectors:

$$|E_+\rangle = \frac{1}{\sqrt{2}} \begin{pmatrix} 1 \\ -1 \end{pmatrix}, \qquad |E_-\rangle = \frac{1}{\sqrt{2}} \begin{pmatrix} 1 \\ 1 \end{pmatrix}. \tag{B.5.3}$$

We may now construct our initial condition in the energy basis, in which the matrix representation of the time evolution operator

$$\hat{U}(\tau) = \exp\left(-i\hat{H}_{\text{Latt}}\tau\right) \tag{B.5.4}$$

is diagonal:

$$|\psi(\tau = 0)\rangle = |k = 0\rangle = \frac{1}{\sqrt{2}} \left(|E_+\rangle + |E_-\rangle\right). \tag{B.5.5}$$

The time evolution of the population in the zeroth diffraction order is given by:

$$\begin{aligned} P_0 &= \left| \frac{1}{2} \left(\langle E_+| + \langle E_-|\right) \hat{U}(\tau) \left(|E_+\rangle + |E_-\rangle\right) \right|^2, \\ &= \frac{1}{4} \left| e^{-iE_+\tau} + e^{-iE_-\tau} \right|^2, \\ &= \frac{1}{4} \left| e^{-iV_{\text{eff}}\tau/2} + e^{iV_{\text{eff}}\tau/2} \right|^2, \\ &= \cos^2(V_{\text{eff}}\tau/2), \end{aligned} \tag{B.5.6}$$

which corresponds to Eq. (14.2.3a).

B.6 Derivation of β dependent two-state model

To calculate the time-evolved population for a given quasimomentum subspace, we follow the same procedure as in Appendix B.5. Equation (15.1.1), reproduced here for convenience

$$H_{\text{Latt}}^{2\times2}(\beta) = \begin{pmatrix} \beta^2/2 & -V_{\text{eff}}/2 \\ -V_{\text{eff}}/2 & (1 - 2\beta + \beta^2)/2 \end{pmatrix},$$

is nothing other than a Rabi matrix, the eigenvalues of which are $E_\pm = \left[(1/2 - \beta + \beta^2) \pm \sqrt{(\beta - 1/2)^2 + V_{\text{eff}}^2}\right]/2$, and the corresponding eigenvectors:

$$|E_+\rangle = \begin{pmatrix} \cos(\alpha/2) \\ \sin(\alpha/2) \end{pmatrix} = \frac{1}{\sqrt{2}}\left[\sqrt{1 + \cos(\alpha)}|k = 0\rangle \right.$$
$$\left. + \sqrt{1 - \cos(\alpha)}|k = -1\rangle\right], \quad \text{(B.6.1a)}$$

$$|E_+\rangle = \begin{pmatrix} -\sin(\alpha/2) \\ \cos(\alpha/2) \end{pmatrix} = -\frac{1}{\sqrt{2}}\left[\sqrt{1 - \cos(\alpha)}|k = 0\rangle \right.$$
$$\left. - \sqrt{1 + \cos(\alpha)}|k = -1\rangle\right], \quad \text{(B.6.1b)}$$

where $\cos(\alpha) = (\beta - 1/2)/\sqrt{(\beta - 1/2)^2 + V_{\text{eff}}^2}$. This leads directly to:

$$|\psi(\tau = 0)\rangle = |k = 0\rangle = \cos(\alpha/2)|E_+\rangle - \sin(\alpha/2)|E_-\rangle$$
$$= \frac{1}{\sqrt{2}}\left[\sqrt{1 + \cos(\alpha)}|E_+\rangle - \sqrt{1 - \cos(\alpha)}|E_-\rangle\right].$$

We may now simply calculate the time-evolved state from the action of the time evolution operator

$$\hat{U}(\tau, \beta) = \exp\left(-i\hat{H}(\beta)_{\text{Latt}}\tau\right),$$

on this initial state thus:

$$|\psi(\tau, \beta)\rangle = \exp\left(-i\hat{H}(\beta)_{\text{Latt}}\tau\right)|k = 0\rangle$$
$$= \frac{1}{\sqrt{2}}\left[\sqrt{1 + c}\, e^{-iE_+\tau}|E_+\rangle + \sqrt{1 - c}\, e^{-iE_-\tau}|E_-\rangle\right].$$

Here we have introduced $c \equiv \cos(\alpha)$. The time-evolved population in the zeroth diffraction order for a given β subspace is then given by:

$$
\begin{aligned}
p_0(\tau, \beta) &= |\langle k = 0 | \psi(\tau, \beta) \rangle|^2 \\
&= \frac{1}{4} \left| (1 + c) e^{-iE_+\tau} + (1 - c) e^{-iE_-\tau} \right|^2 \\
&= \frac{1}{4} \left| e^{E_+\tau/2} e^{E_-\tau/2} \left[(1 + c) e^{-i[E_+ - E_-]\tau/2} + (1 - c) e^{i[E_+ - E_-]\tau/2} \right] \right|^2 \\
&= \cos^2([E_+ - E_-]\tau/2) + c^2 \sin^2([E_+ - E_-]\tau/2) \\
&= 1 + (c^2 - 1) \sin^2([E_+ - E_-]\tau/2) \\
&= 1 - \frac{V_{\text{eff}}^2}{(\beta - 1/2)^2 + V_{\text{eff}}^2} \sin^2 \left(\sqrt{(\beta - 1)^2 + V_{\text{eff}}^2} \tau/2 \right),
\end{aligned}
\tag{B.6.2}
$$

which corresponds to Eq. (15.1.2).

B.7   Derivation of finite-temperature matrix equation

To derive the matrix equation for the finite-temperature response of the zeroth diffraction order population, we begin from Eq. (15.2.2), into which we insert Eqs. (15.2.1) and (15.1.2), yielding:

$$
\begin{aligned}
P_0(w) = 1 &- \\
&\frac{1}{\sqrt{2\pi}w} \int_{-\infty}^{\infty} d\alpha \frac{V_{\text{eff}}^2}{\alpha^2 + V_{\text{eff}}^2} \exp\left(\frac{-\alpha^2}{2w^2}\right) \sin^2 \left(\sqrt{\alpha^2 + V_{\text{eff}}^2} \frac{\tau}{2} \right), \\
&= 1 - P_{-1}(w)
\end{aligned}
\tag{B.7.1}
$$

where we have introduced $\alpha \equiv (\beta - 1/2)$. For simplicity, we now refer to $P_{-1}(w)$, the population in the $|k = -1\rangle$ state. The sinusoidal term can be rewritten using $\sin^2(\theta) = [1 - \cos(2\theta)]/2$, thus:

$$
P_{-1}(w) = \frac{V_{\text{eff}}^2}{\sqrt{2\pi}w} \int_0^{\infty} d\alpha \frac{1}{\alpha^2 + V_{\text{eff}}^2} \exp\left(\frac{-\alpha^2}{2w^2}\right) \times \left[1 - \cos\left(\sqrt{\alpha^2 + V_{\text{eff}}^2} \tau \right) \right],
\tag{B.7.2}
$$

where we have used the fact that the integrand is an even function. The term in $\cos\left(\sqrt{\alpha^2 + V_{\text{eff}}^2}\,\tau\right)$ can then be power expanded, leading to:

$$
\begin{aligned}
P_{-1}(w) &= \frac{V_{\text{eff}}^2}{\sqrt{2\pi}w} \int_0^\infty d\alpha \frac{-1}{\alpha^2 + V_{\text{eff}}^2} \exp\left(\frac{-\alpha^2}{2w^2}\right) \sum_{s=1}^\infty \frac{(-1)^s(\alpha^2 + V_{\text{eff}}^2)^s \tau^{2s}}{(2s)!}, \\
&= \frac{V_{\text{eff}}^2}{\sqrt{2\pi}w} \sum_{s=0}^\infty \frac{(-1)^s \tau^{2(s+1)}}{(2[s+1])!} \int_0^\infty d\alpha \exp\left(\frac{-\alpha^2}{2w^2}\right)(\alpha^2 + V_{\text{eff}}^2)^s, \quad \text{(B.7.3)}
\end{aligned}
$$

such that the square root in the argument no longer appears, and the $(\alpha^2 + V_{\text{eff}}^2)^s$ term can be binomially expanded thus:

$$
P_{-1}(w) = \frac{V_{\text{eff}}^2}{\sqrt{2\pi}w} \sum_{s=0}^\infty \frac{(-1)^s \tau^{2(s+1)} s!}{(2[s+1])!} \sum_{q=0}^s \frac{V^{2(s-q)}}{q!(s-q)!} \int_0^\infty d\alpha\, \alpha^{2q} \exp\left(\frac{-\alpha^2}{2w^2}\right). \quad \text{(B.7.4)}
$$

Further, introducing $\xi \equiv \alpha^2/(2w^2)$, the remaining integral can be rewritten as:

$$
\begin{aligned}
\int_0^\infty d\alpha\, \alpha^{2q} \exp\left(\frac{-\alpha^2}{2w^2}\right) &= w^{2q+1} 2^{q-1/2} \int_0^\infty d\xi \exp(-\xi)\xi^{q-1/2}, \\
&= w^{2q+1} 2^{q-1/2} \Gamma(q+1/2),
\end{aligned}
$$

which, when substituted into Eq. (B.7.4) leads to:

$$
P_{-1}(w) = \frac{1}{2\sqrt{\pi}} \sum_{s=0}^\infty \frac{(-1)^s (V_{\text{eff}}\tau)^{2(s+1)} s!}{(2[s+1])!} \sum_{q=0}^s \frac{1}{q!(s-q)!} \left(\frac{2w^2}{V_{\text{eff}}^2}\right)^q \Gamma(q+1/2). \quad \text{(B.7.5)}
$$

Finally, noting that $\Gamma(s+1/2) = (2s)!\,\sqrt{\pi}/(2^{2s} s!)$, Eq. (B.7.5) can be rewritten, thus:

$$
\begin{aligned}
P_{-1}(w) &= \sum_{s=0}^\infty \sum_{q=0}^s \frac{(-V_{\text{eff}}^2 \tau^2)^{s+1} s!}{(2[s+1])!} \frac{\left(-\frac{1}{2}\right)(2q)!}{(q!)^2(s-q)!} \left(\frac{w^2}{2V_{\text{eff}}^2}\right)^q, \quad \text{(B.7.6)} \\
&= u_s(V_{\text{eff}}\tau) M_{s,q} v_q(w/V_{\text{eff}}),
\end{aligned}
$$

or, equivalently, with $\phi = V_{\text{eff}}\tau$ and $\rho = w/V_{\text{eff}}$:

$$
P_0(\rho) = 1 - P_{-1}(\rho) = 1 - \sum_{s=0}^\infty \sum_{q=0}^s u_s(\phi) M_{s,q} v_q(\rho),
$$

which corresponds to Eq. (15.2.4).

B.8   Expression of Eq. (15.2.4) in terms of Sinc functions

Equation (B.7.6) can be rewritten as:

$$
P_{-1}(\rho) = \sum_{q=0}^{\infty} \left(\frac{\rho^2}{2}\right)^q \frac{(2q)!}{q!^2} \left\{ \left(\frac{-1}{2}\right) \sum_{s=q}^{\infty} \frac{s!}{(2[s+1])!(s-q)!} (-\phi^2)^{s+1} \right\},
$$

where we have used $\phi = V_{\text{eff}}t$ and $\rho = w/V_{\text{eff}}$. We now introduce $\tau = \phi^2$ and re-index the sum in s, yielding:

$$
P_{-1}(\rho) = \sum_{q=0}^{\infty} \left(\frac{\rho^2}{2}\right)^q \frac{(2q)!}{q!^2} \left\{ \left(\frac{-1}{2}\right) \sum_{s=q+1}^{\infty} \frac{(s-1)!}{(2s)!(s-1-q)!} (-1)^s \tau^s \right\}.
$$

Expanding the factorial terms in s and rearranging in τ in the following way:

$$
P_{-1}(\rho) = \sum_{q=0}^{\infty} \left(\frac{\rho^2}{2}\right)^q \frac{(2q)!}{q!^2} \left\{ \tau^{q+1} \left(\frac{-1}{2}\right) \sum_{s=1}^{\infty} \frac{(s-1)(s-2)...(s-q)}{(2s)!} (-1)^s \tau^{s-q-1} \right\},
$$

which we recognize can be expressed as a derivative in q, thus:

$$
P_{-1}(\rho) = \sum_{q=0}^{\infty} \left(\frac{\rho^2}{2}\right)^q \frac{(2q)!}{q!^2} \left\{ \tau^{q+1} \left(\frac{-1}{2}\right) \frac{d^q}{d\tau^q} \sum_{s=1}^{\infty} \frac{(-1)^s \tau^{s-1}}{(2s)!} \right\}. \tag{B.8.1}
$$

Equation (B.8.1) can be rewritten:

$$
P_{-1}(\rho) = \sum_{q=0}^{\infty} \left(\frac{\rho^2}{2}\right)^q \frac{(2q)!}{q!^2} \left\{ \tau^{q+1} \frac{d^q}{d\tau^q} \left(\frac{1}{\tau} \left[-\frac{1}{2} \sum_{s=1}^{\infty} \frac{(-1)^s \tau^{s-1}}{(2s)!} \right] \right) \right\},
$$

such that the sum in s can now be recognized as a sinusoidal term, yielding:

$$
P_{-1}(\rho) = \sum_{q=0}^{\infty} \left(\frac{\rho^2}{2}\right)^q \frac{(2q)!}{q!^2} \left\{ \tau^{q+1} \frac{d^q}{d\tau^q} \left(\frac{1}{\tau} \left[\frac{\sin^2(\sqrt{\tau}/2)}{\tau} \right] \right) \right\}.
$$

Reintroducing ϕ leads to:

$$
\begin{aligned}
P_{-1}(\rho) &= \sum_{q=0}^{\infty} \left(\frac{\rho^2}{2}\right)^q \frac{(2q)!}{q!^2} \left\{ \phi^{2(q+1)} \left(\frac{1}{2\phi}\frac{\mathrm{d}}{\mathrm{d}\phi}\right)^q \left[\frac{\sin^2(\phi/2)}{\phi^2}\right] \right\}, \\
&= \frac{1}{2} \sum_{q=0}^{\infty} \left(\frac{\rho^2}{2}\right)^q \frac{(2q)!}{q!^2} \left\{ \left(\frac{\phi^2}{2}\right)^{q+1} \left(\frac{1}{\phi}\frac{\mathrm{d}}{\mathrm{d}\phi}\right)^q \left[\frac{\sin^2(\phi/2)}{\phi^2}\right] \right\}, \\
&= \frac{1}{2} \sum_{q=0}^{\infty} \left(\frac{\rho^2}{2}\right)^q \frac{(2q)!}{q!^2} \\
&\quad \times \left\{ \left(\frac{\phi^2}{2}\right)^{q+1} \frac{1}{2^{2q}} \left[\left(\frac{2}{\phi}\right)\frac{\mathrm{d}}{\mathrm{d}(\phi/2)}\right]^q \left[\frac{\sin^2(\phi/2)}{\phi^2}\right] \right\}.
\end{aligned}
$$

Equivalently,

$$
\begin{aligned}
P_0(\rho) &= 1 - P_1(\rho) \\
&= 1 - \sum_{q=0}^{\infty} \left(\frac{\rho}{2}\right)^{2q} \frac{(2q)!}{q!^2} \left\{ \left(\frac{\phi}{2}\right)^{2(q+1)} \left[\left(\frac{2}{\phi}\right)\frac{\mathrm{d}}{\mathrm{d}(\phi/2)}\right]^q \left[\frac{\sin^2(\phi/2)}{(\phi/2)^2}\right] \right\},
\end{aligned}
$$

which corresponds to Eq. (15.2.5).

Bibliography

[1] R. M. Godun, M. B. d'Arcy, M. K. Oberthaler, G. S. Summy, and K. Burnett. *Quantum accelerator modes: A tool for atom optics*. Phys. Rev. A **62**, 013411 (2000).

[2] M. Saunders, P. L. Halkyard, S. A. Gardiner, and K. J. Challis. *Fractional resonances in the atom-optical δ-kicked accelerator*. Phys. Rev. A **79**, 023423 (2009).

[3] B. T. Beswick, I. G. Hughes, S. A. Gardiner, H. P. A. G. Astier, M. F. Andersen, and B. Daszuta. *ϵ-pseudoclassical model for quantum resonances in a cold dilute atomic gas periodically driven by finite-duration standing-wave laser pulses*. Phys. Rev. A **94**, 063604 (2016).

[4] O. Morsch and M. Oberthaler. *Dynamics of Bose-Einstein condensates in optical lattices*. Rev. Mod. Phys. **78**, 179 (2006).

[5] L. E. Reichl. *The Transition to Chaos*, (Springer-Verlag New York, Inc., New York 2004).

[6] A. J. Lichtenberg and M. A. Lieberman. *Regular and Chaotic Dynamics*, (Springer-Verlag New York, Inc., New York 1992).

[7] C. F. Bharucha, J. C. Robinson, F. L. Moore, B. Sundaram, Q. Niu, and M. G. Raizen. *Dynamical localization of ultracold sodium atoms*. Phys. Rev. E **60**, 3881 (1999).

[8] F. L. Moore, J. C. Robinson, C. Bharucha, P. E. Williams, and M. G. Raizen. *Observation of Dynamical Localization in Atomic Momentum Transfer: A New Testing Ground for Quantum Chaos*. Phys. Rev. Lett. **73**, 2974 (1994).

[9] B. Klappauf, W. Oskay, D. Steck, and M. Raizen. *Quantum chaos with cesium atoms: pushing the boundaries*. Physica D: Nonlinear Phenomena **131**, 78 (1999). Classical Chaos and its Quantum Manifestations.

[10] D. A. Steck, V. Milner, W. H. Oskay, and M. G. Raizen. *Quantitative study of amplitude noise effects on dynamical localization*. Phys. Rev. E **62**, 3461 (2000).

[11] V. Milner, D. A. Steck, W. H. Oskay, and M. G. Raizen. *Recovery of classically chaotic behavior in a noise-driven quantum system*. Phys. Rev. E **61**, 7223 (2000).

[12] W. H. Oskay, D. A. Steck, and M. G. Raizen. *Timing noise effects on dynamical localization*. Chaos, Solitons & Fractals **16**, 409 (2003).

[13] K. Vant, G. Ball, and N. Christensen. *Momentum distributions for the quantum δ-kicked rotor with decoherence*. Phys. Rev. E **61**, 5994 (2000).

[14] H. Ammann and N. Christensen. *Mixing internal and external atomic dynamics in the kicked rotor*. Phys. Rev. E **57**, 354 (1998).

[15] F. L. Moore, J. C. Robinson, C. F. Bharucha, B. Sundaram, and M. G. Raizen. *Atom Optics Realization of the Quantum δ-Kicked Rotor*. Phys. Rev. Lett. **75**, 4598 (1995).

[16] M. Bienert, F. Haug, W. P. Schleich, and M. G. Raizen. *Kicked rotor in Wigner phase space*. Fortschr. Phys. **51**, No. 45, 474 486 (2003).

[17] D. H. White, S. K. Ruddell, and M. D. Hoogerland. *Phase noise in the delta kicked rotor: from quantum to classical*. New J. Phys. **16**, 113039 (2014).

[18] M. B. d'Arcy, R. M. Godun, M. K. Oberthaler, G. S. Summy, K. Burnett, and S. A. Gardiner. *Approaching classicality in quantum accelerator modes through decoherence*. Phys. Rev. E **64**, 056233 (2001).

[19] M. B. d'Arcy, R. M. Godun, M. K. Oberthaler, D. Cassettari, and G. S. Summy. *Quantum Enhancement of Momentum Diffusion in the Delta-Kicked Rotor*. Phys. Rev. Lett. **87**, 074102 (2001).

[20] M. Sadgrove, A. Hilliard, T. Mullins, S. Parkins, and R. Leonhardt. *Observation of robust quantum resonance peaks in an atom optics kicked rotor with amplitude noise*. Phys. Rev. E **70**, 036217 (2004).

[21] J. F. Kanem, S. Maneshi, M. Partlow, M. Spanner, and A. M. Steinberg. *Observation of High-Order Quantum Resonances in the Kicked Rotor*. Phys. Rev. Lett. **98**, 083004 (2007).

[22] G. J. Duffy, A. S. Mellish, K. J. Challis, and A. C. Wilson. *Nonlinear atom-optical δ-kicked harmonic oscillator using a Bose-Einstein condensate*. Phys. Rev. A **70**, 041602 (2004).

[23] G. Behinaein, V. Ramareddy, P. Ahmadi, and G. S. Summy. *Exploring the Phase Space of the Quantum δ-Kicked Accelerator*. Phys. Rev. Lett. **97**, 244101 (2006).

[24] C. Ryu, M. F. Andersen, A. Vaziri, M. B. d'Arcy, J. M. Grossman, K. Helmerson, and W. D. Phillips. *High-Order Quantum Resonances Observed in a Periodically Kicked Bose-Einstein Condensate*. Phys. Rev. Lett. **96**, 160403 (2006).

[25] P. Szriftgiser, J. Ringot, D. Delande, and J. C. Garreau. *Observation of Sub-Fourier Resonances in a Quantum-Chaotic System*. Phys. Rev. Lett. **89**, 224101 (2002).

[26] K. Vant, G. Ball, H. Ammann, and N. Christensen. *Experimental evidence for the role of cantori as barriers in a quantum system*. Phys. Rev. E **59**, 2846 (1999).

[27] M. E. K. Williams, M. P. Sadgrove, A. J. Daley, R. N. C. Gray, S. M. Tan, A. S. Parkins, N. Christensen, and R. Leonhardt. *Measurements of diffusion resonances for the atom optics quantum kicked rotor*. J. Opt. B: Quant. Semiclass. Optics **6**, 28 (2004).

[28] G. J. Duffy, S. Parkins, T. Müller, M. Sadgrove, R. Leonhardt, and A. C. Wilson. *Experimental investigation of early-time diffusion in the quantum kicked rotor using a Bose-Einstein condensate*. Phys. Rev. E **70**, 056206 (2004).

[29] M. F. Andersen and T. Sleator. *Lattice Interferometer for Laser-Cooled Atoms*. Phys. Rev. Lett. **103**, 070402 (2009).

[30] W. Kao, Y. Tang, N. Q. Burdick, and B. L. Lev. *Anisotropic dependence of tune-out wavelength near Dy 741-nm transition*. Opt. Express **25**, 3411 (2017).

[31] M. Saunders. *Manifestation of quantum resonant effects in the atom-optical delta-kicked accelerator*. Ph.D. thesis, University of Durham, UK (2009).

[32] C. D. Herold, V. D. Vaidya, X. Li, S. L. Rolston, J. V. Porto, and M. S. Safronova. *Precision Measurement of Transition Matrix Elements via Light Shift Cancellation.* Phys. Rev. Lett. **109**, 243003 (2012).

[33] B. Daszuta and M. F. Andersen. *Atom interferometry using δ-kicked and finite-duration pulse sequences.* Phys. Rev. A **86**, 043604 (2012).

[34] B. T. Beswick, I. G. Hughes, and S. A. Gardiner. *Lattice-depth measurement using multipulse atom diffraction in and beyond the weakly diffracting limit.* Phys. Rev. A **99**, 013614 (2019).

[35] B. T. Beswick, I. G. Hughes, and S. A. Gardiner. *Lattice-depth measurement using continuous grating atom diffraction.* arXiv **quant-ph**, 1903.04011 (2019).

[36] A. Miffre and M. Jacquey and M. Büchner and G. Trénec and J. Vigué. *Atom interferometry.* Physica Scripta **74**, C15 (2006).

[37] P. Cladé, S. Guellati-Khélifa, F. Nez, and F. Biraben. *Large Momentum Beam Splitter Using Bloch Oscillations.* Phys. Rev. Lett. **102**, 240402 (2009).

[38] H. Müller, S.-w. Chiow, S. Herrmann, and S. Chu. *Atom Interferometers with Scalable Enclosed Area.* Phys. Rev. Lett. **102**, 240403 (2009).

[39] S.-w. Chiow, T. Kovachy, H.-C. Chien, and M. A. Kasevich. *102ℏk Large Area Atom Interferometers.* Phys. Rev. Lett. **107**, 130403 (2011).

[40] F. M. Izrailev and D. L. Shepelyanskii. *Quantum Resonance for a Rotator in a Nonlinear Field.* Theor. Math. Phys. **43**, 553 (1980).

[41] A. C. Doherty, K. M. D. Vant, G. H. Ball, N. Christensen, and R. Leonhardt. *Momentum distributions for the quantum δ-kicked rotor with decoherence.* Journal of Optics B: Quantum and Semiclassical Optics **2**, 605 (2000).

[42] W. H. Oskay, D. A. Steck, V. Milner, B. G. Klappauf, and M. G. Raizen. *Ballistic peaks at quantum resonance.* Opt. Comm. **179**, 137 (2000).

[43] S. Fishman, I. Guarneri, and L. Rebuzzini. *A Theory for Quantum Accelerator Modes in Atom Optics.* Journal of Statistical Physics **110**, 911 (2003).

[44] S. Fishman, I. Guarneri, and L. Rebuzzini. *Stable Quantum Resonances in Atom Optics*. Phys. Rev. Lett. **89**, 084101 (2002).

[45] M. Kasevich and S. Chu. *Laser cooling below a photon recoil with three-level atoms*. Phys. Rev. Lett. **69**, 1741 (1992).

[46] S. Inouye, M. R. Andrews, J. Stenger, H.-J. Miesner, D. M. Stamper-Kurn, and W. Ketterle. *Observation of Feshbach resonances in a Bose-Einstein condensate*. Nature **392**, 151 (1998).

[47] J. L. Roberts, N. R. Claussen, J. P. Burke, C. H. Greene, E. A. Cornell, and C. E. Wieman. *Resonant Magnetic Field Control of Elastic Scattering in Cold ^{85}Rb*. Phys. Rev. Lett. **81**, 5109 (1998).

[48] T. Köhler, K. Góral, and P. S. Julienne. *Production of cold molecules via magnetically tunable Feshbach resonances*. Rev. Mod. Phys. **78**, 1311 (2006).

[49] M. Gustavsson, E. Haller, M. J. Mark, J. G. Danzl, G. Rojas-Kopeinig, and H.-C. Nägerl. *Control of Interaction-Induced Dephasing of Bloch Oscillations*. Phys. Rev. Lett. **100**, 080404 (2008).

[50] P. K. Molony, P. D. Gregory, Z. Ji, B. Lu, M. P. Köppinger, C. R. Le Sueur, C. L. Blackley, J. M. Hutson, and S. L. Cornish. *Creation of Ultracold $^{87}Rb^{133}Cs$ Molecules in the Rovibrational Ground State*. Phys. Rev. Lett. **113**, 255301 (2014).

[51] M. Saunders, P. L. Halkyard, K. J. Challis, and S. A. Gardiner. *Manifestation of quantum resonances and antiresonances in a finite-temperature dilute atomic gas*. Phys. Rev. A **76**, 043415 (2007).

[52] Y. Zheng. *Chaos and momentum diffusion of the classical and quantum kicked rotor*. Ph.D. thesis, University of North Texas, USA (2005).

[53] C. J. Foot. *Atomic Physics (Oxford Master Series in Atomic, Optical and Laser Physics)*. 1st ed., (Oxford University Press, USA2005).

[54] N. Ashcroft and N. Mermin. *Solid State Physics*, (Saunders College, Philadelphia1976).

[55] R. Bach, K. Burnett, M. B. d'Arcy, and S. A. Gardiner. *Quantum-mechanical cumulant dynamics near stable periodic orbits in phase space: Application to the classical-like dynamics of quantum accelerator modes*. Phys. Rev. A **71**, 033417 (2005).

[56] R. Lima and D. Shepelyansky. *Fast delocalization in a model of quantum kicked rotator*. Phys. Rev. Lett. **67**, 1377 (1991).

[57] P. L. Halkyard, M. Saunders, S. A. Gardiner, and K. J. Challis. *Power-law behavior in the quantum-resonant evolution of the δ-kicked accelerator*. Phys. Rev. A **78**, 063401 (2008).

[58] M. K. Oberthaler, R. M. Godun, M. B. d'Arcy, G. S. Summy, and K. Burnett. *Observation of Quantum Accelerator Modes*. Phys. Rev. Lett. **83**, 4447 (1999).

[59] E. Hecht. *Optics*, (Addison Wesley, San Francisco2002).

[60] A. Ullah. *Delta-kicked rotor experiments with an all-optical BEC*. Ph.D. thesis, University of Auckland, New Zealand (2012).

[61] A. D. Cronin, J. Schmiedmayer, and D. E. Pritchard. *Optics and interferometry with atoms and molecules*. Rev. Mod. Phys. **81**, 1051 (2009).

[62] C. F. Bharucha. *Experiments in dynamical localization of ultra-cold sodium atoms using time-dependent optical potentials*. Ph.D. thesis, the University of Texas at Austin, US (1997).

[63] S. Wimberger, I. Guarneri, and S. Fishman. *Quantum resonances and decoherence for δ-kicked atoms*. Nonlinearity **16**, 1381 (2003).

[64] S. Wimberger, I. Guarneri, and S. Fishman. *Classical Scaling Theory of Quantum Resonances*. Phys. Rev. Lett. **92**, 084102 (2004).

[65] L. Rebuzzini, S. Wimberger, and R. Artuso. *Delocalized and resonant quantum transport in nonlinear generalizations of the kicked rotor model*. Phys. Rev. E **71**, 036220 (2005).

[66] S. Schlunk, M. B. d'Arcy, S. A. Gardiner, D. Cassettari, R. M. Godun, and G. S. Summy. *Signatures of Quantum Stability in a Classically Chaotic System*. Phys. Rev. Lett. **90**, 054101 (2003).

[67] S. Schlunk, M. B. d'Arcy, S. A. Gardiner, and G. S. Summy. *Experimental Observation of High-Order Quantum Accelerator Modes*. Phys. Rev. Lett. **90**, 124102 (2003).

[68] Z. Ma, M. B. d'Arcy, and S. A. Gardiner. *Gravity-Sensitive Quantum Dynamics in Cold Atoms*. Phys. Rev. Lett. **93**, 164101 (2004).

[69] A. Buchleitner, M. B. d'Arcy, S. Fishman, S. A. Gardiner, I. Guarneri, Z.-Y. Ma, L. Rebuzzini, and G. S. Summy. *Quantum Accelerator Modes from the Farey Tree*. Phys. Rev. Lett. **96**, 164101 (2006).

[70] M. B. d'Arcy, R. M. Godun, D. Cassettari, and G. S. Summy. *Accelerator-mode-based technique for studying quantum chaos*. Phys. Rev. A **67**, 023605 (2003).

[71] M. Abb, I. Guarneri, and S. Wimberger. *Pseudoclassical theory for fidelity of nearly resonant quantum rotors*. Phys. Rev. E **80**, 035206 (2009).

[72] Johann G Danzl and Manfred J Mark and Elmar Haller and Mattias Gustavsson and Russell Hart and Andreas Liem and Holger Zellmer and Hanns-Christoph Nägerl. *Deeply bound ultracold molecules in an optical lattice*. New J. Phys. **11**, 055036 (2009).

[73] S. Kotochigova and E. Tiesinga. *Controlling polar molecules in optical lattices*. Phys. Rev. A **73**, 041405 (2006).

[74] I. Bloch, J. Dalibard, and W. Zwerger. *Many-body physics with ultracold gases*. Rev. Mod. Phys. **80**, 885 (2008).

[75] G.-B. Jo, J. Guzman, C. K. Thomas, P. Hosur, A. Vishwanath, and D. M. Stamper-Kurn. *Ultracold Atoms in a Tunable Optical Kagome Lattice*. Phys. Rev. Lett. **108**, 045305 (2012).

[76] J. Mitroy, M. S. Safronova, and C. W. Clark. *Theory and applications of atomic and ionic polarizabilities*. J. Phys. B: At. Mol. Opt. Phys. **43**, 202001 (2010).

[77] B. Arora, M. S. Safronova, and C. W. Clark. *Tune-out wavelengths of alkali-metal atoms and their applications*. Phys. Rev. A **84**, 043401 (2011).

[78] B. M. Henson, R. I. Khakimov, R. G. Dall, K. G. H. Baldwin, L.-Y. Tang, and A. G. Truscott. *Precision Measurement for Metastable Helium Atoms of the 413 nm Tune-Out Wavelength at Which the Atomic Polarizability Vanishes*. Phys. Rev. Lett. **115**, 043004 (2015).

[79] R. H. Leonard, A. J. Fallon, C. A. Sackett, and M. S. Safronova. *High-precision measurements of the* ^{87}Rb *D-line tune-out wavelength*. Phys. Rev. A **92**, 052501 (2015).

[80] L. W. Clark, L.-C. Ha, C.-Y. Xu, and C. Chin. *Quantum Dynamics with Spatiotemporal Control of Interactions in a Stable Bose-Einstein Condensate*. Phys. Rev. Lett. **115**, 155301 (2015).

[81] M. S. Safronova, M. G. Kozlov, and C. W. Clark. *Precision Calculation of Blackbody Radiation Shifts for Optical Frequency Metrology*. Phys. Rev. Lett. **107**, 143006 (2011).

[82] J. A. Sherman, N. D. Lemke, N. Hinkley, M. Pizzocaro, R. W. Fox, A. D. Ludlow, and C. W. Oates. *High-Accuracy Measurement of Atomic Polarizability in an Optical Lattice Clock*. Phys. Rev. Lett. **108**, 153002 (2012).

[83] S. Friebel, C. D'Andrea, J. Walz, M. Weitz, and T. W. Hänsch. CO_2-*laser optical lattice with cold rubidium atoms*. Phys. Rev. A **57**, R20 (1998).

[84] Y. B. Ovchinnikov, J. H. Müller, M. R. Doery, E. J. D. Vredenbregt, K. Helmerson, S. L. Rolston, and W. D. Phillips. *Diffraction of a Released Bose-Einstein Condensate by a Pulsed Standing Light Wave*. Phys. Rev. Lett. **83**, 284 (1999).

[85] C. Cabrera-Gutiérrez, E. Michon, V. Brunaud, T. Kawalec, A. Fortun, M. Arnal, J. Billy, and D. Guéry-Odelin. *Robust calibration of an optical-lattice depth based on a phase shift*. Phys. Rev. A **97**, 043617 (2018).

[86] S. B. Cahn, A. Kumarakrishnan, U. Shim, T. Sleator, P. R. Berman, and B. Dubetsky. *Time-Domain de Broglie Wave Interferometry*. Phys. Rev. Lett. **79**, 784 (1997).

[87] G. Birkl, M. Gatzke, I. H. Deutsch, S. L. Rolston, and W. D. Phillips. *Bragg Scattering from Atoms in Optical Lattices*. Phys. Rev. Lett. **75**, 2823 (1995).

[88] P. Cheiney, C. M. Fabre, F. Vermersch, G. L. Gattobigio, R. Mathevet, T. Lahaye, and D. Guéry-Odelin. *Matter-wave scattering on an amplitude-modulated optical lattice*. Phys. Rev. A **87**, 013623 (2013).

[89] B. Gadway, D. Pertot, R. Reimann, M. G. Cohen, and D. Schneble. *Analysis of Kapitza-Dirac diffraction patterns beyond the Raman-Nath regime*. Opt. Express **17**, 19173 (2009).

[90] F. Schmidt, D. Mayer, M. Hohmann, T. Lausch, F. Kindermann, and A. Widera. *Precision measurement of the ^{87}Rb tune-out wavelength in the hyperfine ground state $F = 1$ at 790 nm*. Phys. Rev. A **93**, 022507 (2016).

[91] L. Deng, E. W. Hagley, J. Denschlag, J. E. Simsarian, M. Edwards, C. W. Clark, K. Helmerson, S. L. Rolston, and W. D. Phillips. *Temporal, Matter-Wave-Dispersion Talbot Effect*. Phys. Rev. Lett. **83**, 5407 (1999).

[92] A. O. Jamison, J. N. Kutz, and S. Gupta. *Atomic interactions in precision interferometry using Bose-Einstein condensates*. Phys. Rev. A **84**, 043643 (2011).

[93] P. Meystre. *Atom Optics*, (Springer, New York2001).

[94] Y. Zhai, C. H. Carson, V. A. Henderson, P. F. Griffin, E. Riis, and A. S. Arnold. *Talbot-enhanced, maximum-visibility imaging of condensate interference*. Optica **5**, 80 (2018).

[95] S. Wu, Y.-J. Wang, Q. Diot, and M. Prentiss. *Splitting matter waves using an optimized standing-wave light-pulse sequence*. Phys. Rev. A **71**, 043602 (2005).

[96] S. M. Barnett and P. M. Radmore. *Methods in Theoretical Quantum Optics*, (Clarendon Press, Oxford1997).

[97] I. G. Hughes and T. P. A. Hase. *Measurements and their Uncertainties*, (Oxford University Press, New York2010).

[98] D. J. Whiting, J. Keaveney, C. S. Adams, and I. G. Hughes. *Direct measurement of excited-state dipole matrix elements using electromagnetically induced transparency in the hyperfine Paschen-Back regime*. Phys. Rev. A **93**, 043854 (2016).

[99] P. J. Martin, B. G. Oldaker, A. H. Miklich, and D. E. Pritchard. *Bragg scattering of atoms from a standing light wave*. Phys. Rev. Lett. **60**, 515 (1988).

[100] D. M. Giltner, R. W. McGowan, and S. A. Lee. *Atom Interferometer Based on Bragg Scattering from Standing Light Waves*. Phys. Rev. Lett. **75**, 2638 (1995).

[101] *Bordé, C. J., 1997, Matter-wave interferometers: a synthetic approach*. P. R. Berman (editor), *Atom Interferometry*, pp. 257–292, (Academic Press, San Diego1997).

[102] M. Kozuma, L. Deng, E. W. Hagley, J. Wen, R. Lutwak, K. Helmerson, S. L. Rolston, and W. D. Phillips. *Coherent Splitting of Bose-Einstein Condensed Atoms with Optically Induced Bragg Diffraction*. Phys. Rev. Lett. **82**, 871 (1999).

[103] S. Gupta, A. Leanhardt, A. Cronin, and D. Pritchard. *Coherent manipulation of atoms with standing light waves*. Comptes Rendus de l'Academie des Sciences - Series IV: Physics, Astrophysics **2**, 479 (2001).